Mo/La_2O_3 NANO MULTILAYERS AND THEIR THERMAL STABILITY AND ELECTRICAL PROPERTIES

A DISSERTATION

Submitted in partial fulfilment of the

requirements for the award of the degree

of

MASTER OF TECHNOLOGY

in

METALLURGICAL AND MATERIALS ENGINEERING
(with specialization in Materials Engineering)

Submitted by

ABHINAV PRIYADARSHI

Department of Metallurgical and Materials Engineering

INDIAN INSTITUTE OF TECHNOLOGY, ROORKEE

ROORKEE – 247667 (INDIA)

MAY 2018

IFW Dresden • Helmholtzstraße 20 • 01069 Dresden

Institute for Complex Materials (IKM)

Dr. Thomas Gemming
Acting Director

Tel +49 351 4659-298/-217
Fax +49 351 4659-452
t.gemming@ifw-dresden.de

5. May 2018

TO WHOM IT MAY CONCERN

This is to certify that the DAAD-IIT Master Sandwich student **Mr. Abhinav Priyadarshi** from Department of Metallurgical and Materials Engineering, Indian Institute of Technology, Roorkee worked at the IFW Dresden, Institute of Complex Materials, Germany from October 1st, 2017 to March 31st, 2018 towards his master dissertation.

The title of his thesis is: "**Mo/La_2O_3 nano multilayers and their thermal stability and electrical properties**".

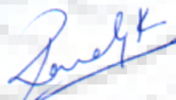

Dr. T. Gemming	Dr. G. Rane	Dr. S. R. Meka
Act. Director, IKM	Research Scientist	Assistant Professor
IFW Dresden	IFW Dresden	IIT Roorkee

CANDIDATE'S DECLARATION

I hereby declare that the proposed work presented in this dissertation entitled "**Mo/La_2O_3 nano multilayers and their thermal stability and electrical properties**" is in partial fulfilment of the requirements for the award of the degree of **Master of Technology in Materials Engineering**, submitted in the **Department of Metallurgical and Materials Engineering, Indian Institute of Technology Roorkee** is an authentic record of my own work carried out during the period of July 2017 to May 2018 under the joint supervision of **Dr. S. R. Meka**, Assistant Professor, Department of Metallurgical and Materials Engineering, Indian Institute of Technology Roorkee, **Dr. G. Rane**, Research Scientist, IFW Dresden and **Dr. T. Gemming**, Acting Director, Institute for Complex Material, IFW Dresden.

The matter presented in this dissertation has not been submitted by me for the award of any other degree.

Dated:

Place: Roorkee (Abhinav Priyadarshi)

CERTIFICATE

This is to certify that the above statement made by the candidate is correct to the best of my knowledge and belief.

Dr. Sai Ramudu Meka
Assistant Professor
Metallurgical and Materials Engineering
Indian Institute of Technology Roorkee
Roorkee – 247667 (India)

ACKNOWLEDGEMENT

In the first place, I am very much grateful to GOD ALMIGHTY for his graces and blessings, without which this study would not have been possible.

It is all but impossible to express how grateful I am to my daily supervisor Dr. Gayatri Rane, who shared her knowledge with me in numerous helpful and inspiring scientific discussions. Her inexhaustible enthusiasm and encouragement have always strengthened my eagerness for science. I convey my sincere thanks to her for the help, guidance, advices, valuable comments, suggestions and support throughout the research work and writing of this dissertation. I would like to thank her for giving the opportunity to carry out the exciting research work and the trust placed in me. I am very grateful for the opportunities and freedom in research she has given me, especially during the last 6 months at the IFW Dresden.

I extend the immeasurable appreciation and deepest gratitude to my guide Dr. Sai Ramudu Meka for his encouragement, suggestions and continuous support which helped me to widen my research from various perspective. I could not have imagined having a better advisor and mentor for my master thesis.

I can't find the right words either to express how thankful I am to Dr. Thomas Gemming, my german co-supervisor during my last 6 months at the IFW Dresden. Many thanks to him for taking time to do TEM investigation. The wonderful result really inspired us a lot.

Besides, I would like to express my sincere gratitude to Dr. Siegfried Menzel for giving me the opportunity to carry out of my thesis work at the SAW Lab Saxony group. It meant a lot to me and I have no words to describe how thankful I am to him for that. Without his precious support it would not have been possible to conduct this research.

It's my fortune to gratefully acknowledge the support of Ms. Eunmi Park for guiding and helping me with my experiments. Her extraordinary commitment and the numerous, intensive discussions were of great importance for the success of this work.

Finally, I convey my thanks to all the group members of SAW Lab Saxony, who supported me daily and provided a pleasant working atmosphere. Especially I would like to thank Dr. Marietta Seifert for doing the TEM studies for my samples, Dr. Steffen Oswald for the XPS measurements along with the analysis and Mr. Thomas Wiek for the FIB measurements. Help received from Mr. Erik Brachmann for film fabrication is greatly acknowledged.

I take this opportunity to sincerely acknowledge the German Academic Exchange Service (DAAD), Delhi for providing the financial assistance in the form of DAAD-IIT Master Sandwich Scholarship which buttressed me to perform my work comfortably.

Last but not least, I would like to pay high regards to my parents and family members who have always supported and cheered me so often. Thank you so much.

Table of Contents

	List of Tables	i
	List of Figures	ii
	Symbols	iv
	Abbreviations	vi
	Abstract	viii
1	**Introduction**	1
1.1	Motivation	1
1.2	Objectives	5
1.3	Thesis Outline	6
2	**Surface Acoustic Wave Device - An Introduction**	7
2.1	Working of a SAW device	7
2.2	Materials for SAW devices	8
2.2.1	*Choice of substrate*	8
2.2.2	*Choice of transducer*	9
3	**Mo-La_2O_3: Potential Metallization System**	12
3.1	Introduction	12
3.2	Mo-La_2O_3 material system	14
3.3	Thin film synthesis methods	15
3.4	Thin film evolution	17
3.5	Stresses in thin films	19
3.6	Size effect in thin films	21
4	**Research Methodologies and Experimental Procedure**	23
4.1	Film preparation	23

4.2	Characterization of thin films	26
4.2.1	*Van der Pauw measurement*	26
4.2.2	*Residual stress measurement*	27
4.2.3	*In-plane microstructure: Scanning electron microscope (SEM)*	29
4.2.4	*Atomic force microscope (AFM)*	30
4.2.5	*Out-plane microstructure: Focused ion beam (FIB)*	31
4.2.6	*X-ray diffraction (XRD)*	32
4.2.7	*X-ray reflectivity (XRR)*	33
4.2.8	*Transmission electron microscopy (TEM)*	35
5	**Results and Discussion**	37
5.1	Electrical resistivity	37
5.2	In-plane microstructure: SEM	39
5.3	Surface roughness	41
5.4	Out-of-plane microstructure: FIB	44
5.5	Film structure: XRR	46
5.6	XRD phase and structure analysis	53
5.7	Interfacial structure analysis	61
5.8	Curvature based residual stress measurement	60
6	**Conclusion**	65
7	**Future scope**	68
	References	69

List of Tables

Table		Page No.
Table 1.1:	Principle applications of SAW devices	3
Table 2.1:	Substrates used for acoustic wave generation	9
Table 2.2:	Characteristics of metals for the SAW IDT's	10
Table 4.1:	Deposited thin film multilayer configuration details	25
Table 4.2:	Sputtering parameters for deposition of thin film multilayers	25
Table 5.1:	Measured resistivity values of thin films using van der Pauw technique	37
Table 5.2:	Measured RMS Surface Roughness (Rq)	42
Table 5.3:	Residual stresses in thin films obtained using curvature method	62

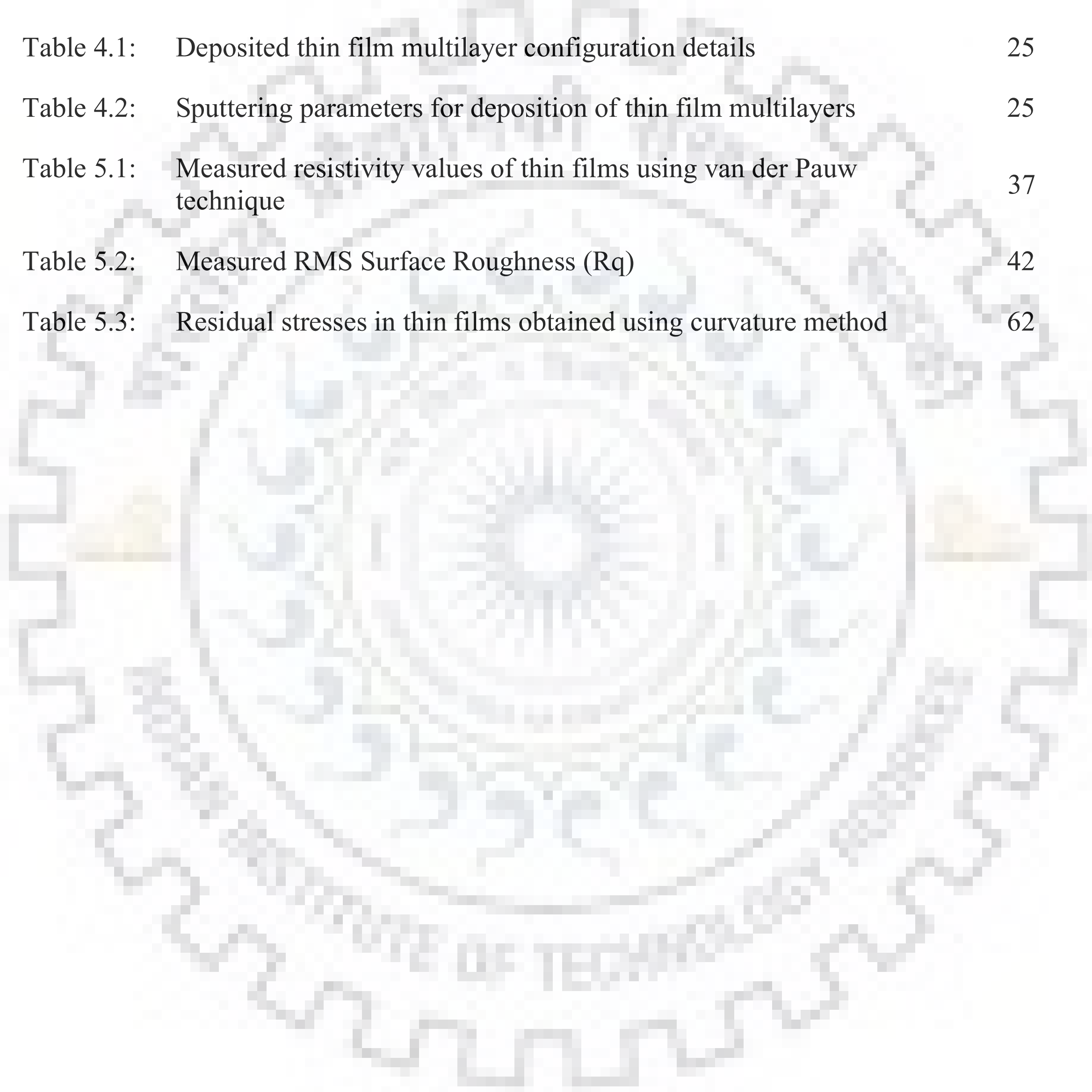

List of Figures

Figure		Page No.
Figure 2.1:	Basic Structure of SAW device	8
Figure 3.1:	Schematic of a DC magnetron sputtering process	16
Figure 3.2:	Schematic illustration of the growth process	17
Figure 3.3:	Structure zone model for metal films	18
Figure 3.4:	Schematic diagram of microstructure evolution	18
Figure 3.5:	Illustrations of film/substrate bending due to (a) compressive, (b) tensile residual stresses in the film and (c) due to mismatch of the coefficients of thermal expansion	20
Figure 4.1:	Designed multilayer film configuration	23
Figure 4.2:	DC magnetron sputtering system for Mo/La2O3¬ multilayer thin films	24
Figure 4.3:	Measurement of specific resistivity of flat sample using van der Pauw technique	27
Figure 4.4:	Wafer probe device for van der Pauw measurements	27
Figure 4.5:	A schematic of a laser-scanning wafer curvature measurement system	28
Figure 4.6:	Curvature stress measurement device	29
Figure 4.7:	Schematic diagram of (a) scanning electron microscope (SEM), (b) Schematic showing interaction volume of the electrons/interaction depth	29
Figure 4.8:	SEM Zeiss Ultra Plus used for viewing the top surface microstructure of the samples	30
Figure 4.9:	Schematic of a Bruker Dimension Icon AFM	31
Figure 4.10:	FIB Crossbeam 1540 XB, Zeiss	32
Figure 4.11:	Panalytical X'Pert XRD device	33
Figure 4.12:	Information provided by X-ray reflectivity curve	35
Figure 4.13:	TEM Tecnai F30 FEI device	36
Figure 5.1:	Resistivity variation as a function of bilayer period	38

Figure 5.2: SEM micrographs of as-deposited and annealed, (a) Mo-Si, (b) Mo-(La_2O_3-Mo)-Si, (c) Mo-(La_2O_3-Mo)$_2$-Si, (d) Mo-(La_2O_3-Mo)$_4$-Si, (e) Mo-(La_2O_3-Mo)$_8$-Si, multilayer thin films. 40

Figure 5.3: AFM topographical images of as-deposited and annealed, (a) Mo-Si, (b) Mo-(La_2O_3-Mo) Si, (c) Mo-(La_2O_3-Mo)$_2$-Si, (d) Mo-(La_2O_3-Mo)$_4$-Si, (e) Mo-(La_2O_3-Mo)$_8$-Si, multilayer thin films and (f) RMS roughness variation as a function of bilayer period and annealing duration 43

Figure 5.4: FIB cross-section view of as-deposited and annealed, (a) Mo-Si, (b) Mo-(La_2O_3-Mo)-Si, (c) Mo-(La_2O_3-Mo)$_2$-Si, (d) Mo-(La_2O_3-Mo)$_4$-Si, (e) Mo-(La_2O_3-Mo)$_8$-Si, multilayer thin films 45

Figure 5.5: XRR curves for as-deposited and annealed, (a) Mo-Si, (b) Mo-(La_2O_3-Mo)-Si, (c) Mo-(La_2O_3-Mo)$_2$-Si, (d) Mo-(La_2O_3-Mo)$_4$-Si, (e) Mo-(La_2O_3-Mo)$_8$-Si, thin films 48

Figure 5.6: Schematic model of the interlayer configuration for Mo-(La_2O_3-Mo)$_8$-Si 50

Figure 5.7: XRR fitted curve and simulated data for Mo-(La_2O_3-Mo)$_8$-Si multilayer thin film in, (a) as deposited, (b) annealed at 800 °C for 24 h, (c) annealed at 800 °C for 48 h, (d) annealed at 800 °C for 120 h, condition 52

Figure 5.8: XRD pattern of multilayer thin film, (a) as deposited, (b) annealed at 800 °C for 24 h, (c) annealed at 800 °C for 48 h, (d) annealed at 800 °C for 120 h, condition 55

Figure 5.9: Enlarged XRD peak of Mo (110) in pure Mo and multilayer thin film in, (a) as deposited, (b) annealed at 800 °C for 24 h, (c) annealed at 800 °C for 48 h, (d) annealed at 800 °C for 120 h, condition 58

Figure 5.10: Volume weighted grain size as a function of bilayer period and annealing duration 59

Figure 5.11: Microstrain as a function of bilayer period and annealing duration 60

Figure 5.12: Cross-sectional bright-field C-TEM of sample Mo-(La_2O_3-Mo)$_8$-Si 61

Figure 5.13: EDX spectra of interlayer area 1 & 2 present in sample Mo-(La_2O_3-Mo)$_8$-Si 62

Figure 5.14: Residual stress variation in the multilayer films in as-deposited and annealed condition 63

Symbols

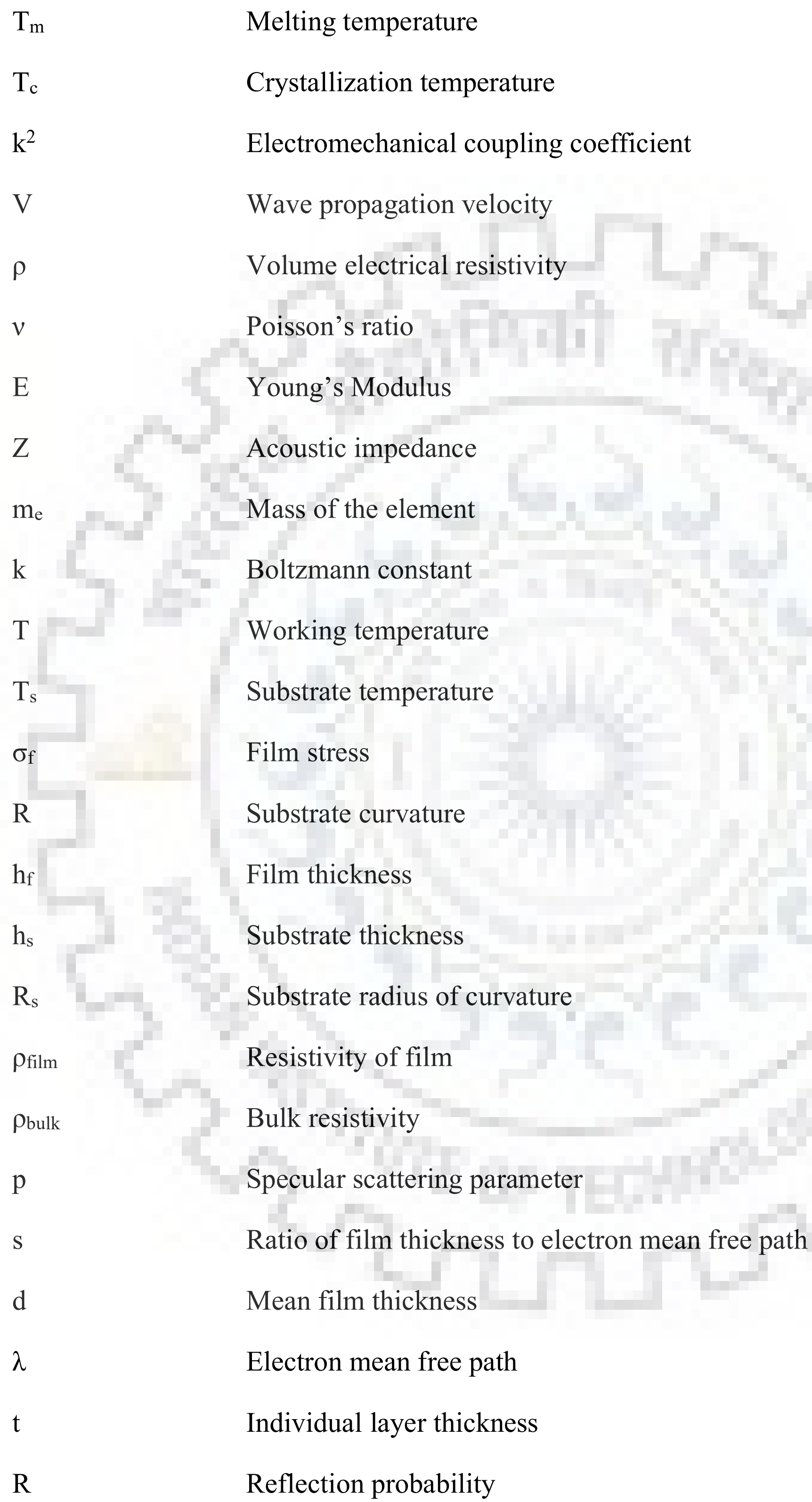

T_m — Melting temperature

T_c — Crystallization temperature

k^2 — Electromechanical coupling coefficient

V — Wave propagation velocity

ρ — Volume electrical resistivity

ν — Poisson's ratio

E — Young's Modulus

Z — Acoustic impedance

m_e — Mass of the element

k — Boltzmann constant

T — Working temperature

T_s — Substrate temperature

σ_f — Film stress

R — Substrate curvature

h_f — Film thickness

h_s — Substrate thickness

R_s — Substrate radius of curvature

ρ_{film} — Resistivity of film

ρ_{bulk} — Bulk resistivity

p — Specular scattering parameter

s — Ratio of film thickness to electron mean free path

d — Mean film thickness

λ — Electron mean free path

t — Individual layer thickness

R — Reflection probability

D	Average in-plane grain size
n	Bilayer period
R_a	Sheet resistance
R_b	Sheet resistance
R_o	Radius of substrate material before deposition
R_f	Radius of substrate after deposition
x	Number of films deposited over substrate
h(x)	Measured diffraction profile
f(x)	Structurally broadened profile
g(x)	Instrumental profile
c	Cauchy component
g	Gaussian component
β	Integral breadth
2θ	Diffraction angle
ε	Microstrain
D_v	Volume weighted crystallite size
n_r	Refractive index
α_c	Critical angle
α_i	Incident angle
ρ_e	Electron density
r_e	Electron radius
m	Order of reflection
R_q	RMS Surface Roughness
ε_s	Lattice strain
a_{Mo}	Lattice parameter of Mo
a_{La2O3}	Lattice parameter of lanthanum oxide

Abbreviations

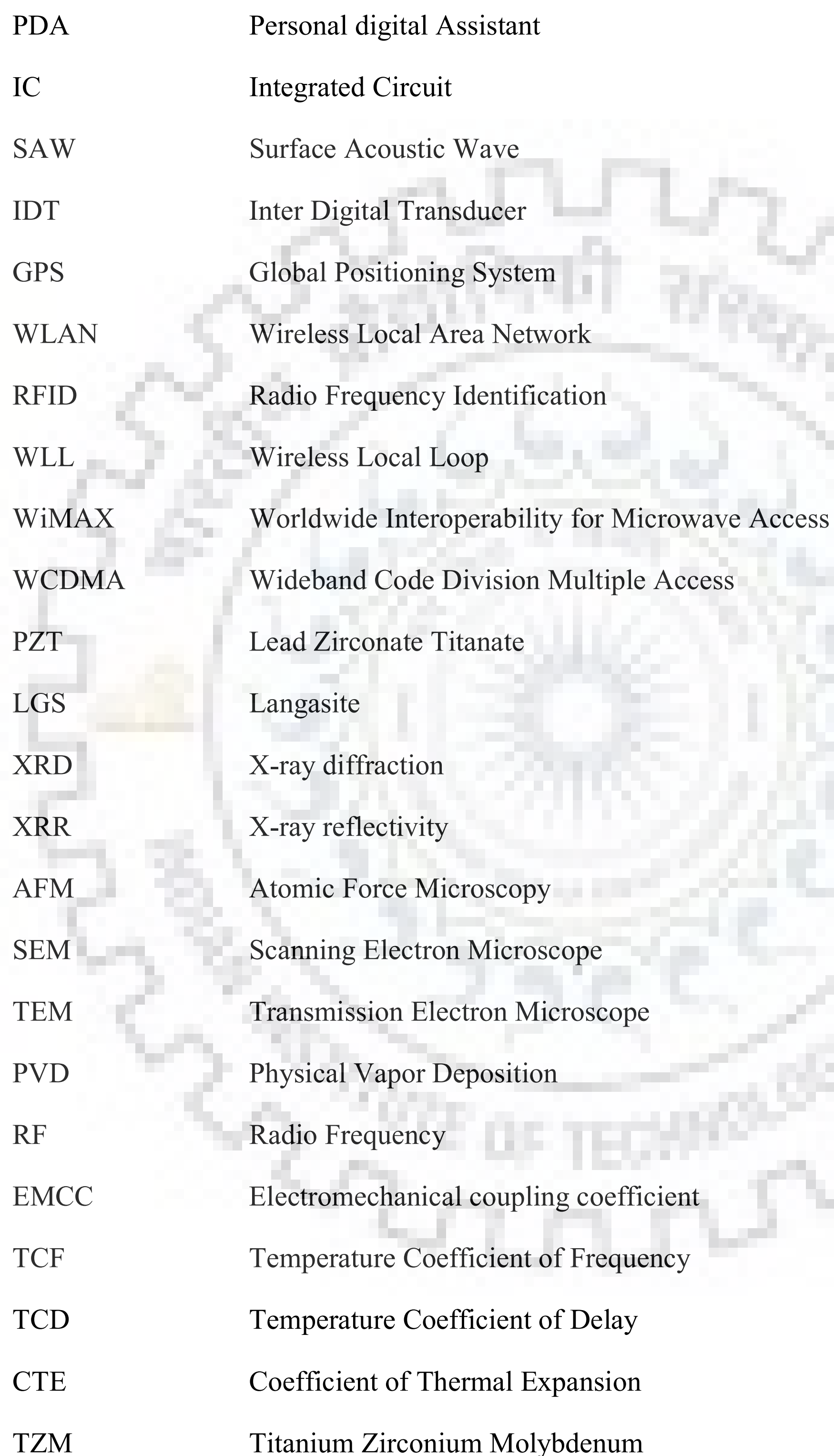

PDA	Personal digital Assistant
IC	Integrated Circuit
SAW	Surface Acoustic Wave
IDT	Inter Digital Transducer
GPS	Global Positioning System
WLAN	Wireless Local Area Network
RFID	Radio Frequency Identification
WLL	Wireless Local Loop
WiMAX	Worldwide Interoperability for Microwave Access
WCDMA	Wideband Code Division Multiple Access
PZT	Lead Zirconate Titanate
LGS	Langasite
XRD	X-ray diffraction
XRR	X-ray reflectivity
AFM	Atomic Force Microscopy
SEM	Scanning Electron Microscope
TEM	Transmission Electron Microscope
PVD	Physical Vapor Deposition
RF	Radio Frequency
EMCC	Electromechanical coupling coefficient
TCF	Temperature Coefficient of Frequency
TCD	Temperature Coefficient of Delay
CTE	Coefficient of Thermal Expansion
TZM	Titanium Zirconium Molybdenum

TZC	Titanium Zirconium Carbon
ODS	Oxide Dispersion Strengthening
UTS	Ultimate Tensile Strength
CVD	Chemical Vapor Deposition
ALD	Atomic Layer Deposition
PLD	Pulsed Layer Deposition
SOD	Stand-off Distance
DC	Direct Current
EMFP	Electron Mean Free Path
FS	Fuchs Sondheimer
MS	Mayadas Shatzkes
AD	As Deposited
HT	Heat Treated
vdP	van der Pauw
PSD	Position Sensitive Photodiode
FIB	Focused Ion Beam
LIMS	Liquid Metal Ion Source
FWHM	Full Width Half Maximum
CTEM	Conventional Transmission Electron Microscopy
STEM	Scanning Transmission Electron Microscope
RMS	Root Mean Square
EDX	Energy Dispersive X-ray spectroscopy

Abstract

Surface acoustic wave based high-temperature sensors are promising devices owing to advantages such as robustness, passive operation and wireless interrogation making them usable in harsh environments as well as mountable on moving equipments. The device's potential to respond to any kind of surface changes/alterations as an electrical signal is the basic underlying principal behind its functioning and sensing. The susceptibility to surface perturbations vary with the configuration of the electrode, choice of substrate and metallization system and the surrounding environment. One of the key challenges in this field is the choice of the electrode material that is stable with long lifetime and high reliability up to operating temperatures of about 800 °C. The main limitations for the use of such nanocrystalline metal films are related to stress-induced damaging processes such as agglomeration, cracking, and delamination along with stress-driven mechanisms such as high temperature creep which become significantly operative at ~ 0.4 T_m. Thus, structural failure would consequently lead to the electrical failure of the device.

In the present dissertation work, the high temperature stability of a new electrode material, Mo-La_2O_3 composite, has been studied up to 800 °C. Different multilayer thin film metallization was deposited on a Si (100) wafer using DC magnetron sputtering at same operating conditions to study microstructural and electrical properties in as-deposited and heat-treated conditions.

Studies revealed that a combination of Mo and La_2O_3 together has improved the performance of the thin films than pure Mo. Among all the films designed here, Mo-(La_2O_3-Mo)$_8$-Si is the most interesting. This film shows the uniform and stable microstructure even after 120 h of vacuum annealing with only a slight decrease in the conductivity. In as-deposited condition, all the films showed a typical rice-like grain morphology. Upon annealing for 120 h, the Mo-(La_2O_3-Mo)$_8$-Si thin film showed the formation of equiaxed grains with smallest in-plane and out-of-plane grain size. The increase in the RMS roughness value was also found to be small for the annealed Mo-(La_2O_3-Mo)$_8$-Si thin film. XRD analysis showed the presence of diffraction peaks of (110), (220) and low intensity (211) associated with BCC Mo. It was observed that both in as-deposited and annealed condition, the multilayer film with 8 bilayer period showed the lowest microstrain when compared to pure Mo and other multilayer films. XRR examination revealed that the density of the all the individual Mo layers were lower than that of the values in bulk indicating that the formed Mo-(La_2O_3-Mo)$_8$-Si film is not dense and consists of pores and voids in both as-deposited and heat-treated condition. The curve fitting showed that the thickness of the individual layers matches well with the intended values. TEM

investigations evidenced the presence of clear and distinct interlayers containing the agglomerates of La_2O_3 in 120 h annealed Mo-(La_2O_3-Mo)$_8$-Si multilayer thin film.

1. Introduction

1.1 Motivation

The state-of-the-art technology for development has narrowed down to make things faster and smaller. An individual was perhaps fortunate enough to have the access to digital platform to perform his task few decades ago. But the surrounding has now completely changed with people having easy accessibility to personal digital assistants (PDAs) such as computers and mobile phones. All these advancements have become conceivable with the progress made by the semiconductor industry in recent years in the field of storage, compactness, high power and speed and configurational aspects. There has been an exponential growth in the density of various semiconductor devices such as diodes, transistors and rectifiers fitted with the so called Integrated circuits (IC's) due to the decrease in manufacturable feature size such as semiconductor chips. To make things simpler these semiconductor devices in the form of sensors are being widely used in various physical, mechanical and chemical systems for their increased performance while measurement & detection.

Monitoring and control of environment conditions in chemical or physical processes is of huge importance, e.g. in smart home / city systems or for the production of standardized products in automated industry setups. Unfortunately, some of these processes are carried out at high temperatures, under corrosive atmosphere or at locations difficult to access, so that monitoring tasks can be hardly achieved with conventional sensors. In vague sense 'Sensor' is a device that generates a suitable output following a specific measured input data [1]. Sensors are used in applications ranging from medical diagnostic and health care, defense and security to automotive and industrial manufacturing as well as environmental monitoring.

With the augment in complexity of the state-of-art control and mechanical devices, there is a surge increase in the number of related challenges linked to its instrumentation and measurement characteristics. There have been significant issues concerning the use of conventional wired sensors, and the associated difficulty in its operation when it comes to spinning or speeding structural systems. This calls for the need of sensors with improved precision, consistency and speed. Recently wireless sensors have gained huge demand for applications wherever wiring is unfeasible. Efforts have been directed towards the study of vital features of different sensors such

as its selectivity, sensitivity, stability and repeatability [2]. To attain these attributes, research has been conducted in search of new sensors based on different principles and materials.

The large amount of information in data communication systems has resulted in an increased demand of devices operating in the GHz frequency band range. Since majority of these systems function with SAW (Surface Acoustic Wave) devices, there is a need for supplementing the resonance frequency. Besides, most of the sensor usage is based on these kinds of devices where the sensitivity is dependent on its frequency.

Piezoelectric effect has been the most commonly utilized technique to create acoustic waves in solids. SAW devices began to be explored after the revelation of the interdigital transducer (IDT) by White and Voltmer in the year 1965 [3]. Later on, the fundamentals of SAW device technology were established in the period 1970-85, pertaining to design methods and evaluation of SAW propagation on lithium niobate and quartz [4]. Subsequently, SAW devices started being used in applications related to wireless communication systems such as mobile phones, RFID tags and remote switches [5]. Nowadays, SAW devices are extensively employed as resonators and band-pass filters in communication systems to filter a transmission frequency. With the advancement in the communication, sensing and radiography technology has led to the increased need for fast and improved SAW devices with minimum losses.

Nearly four billion SAW based band-pass filters for mobile and other communication devices are employed every year in the telecom business [6]. Bluetooth, GPS, WLAN are other such wireless data transfer systems with regular applications of RF filters. Table 1.1 lists the outline of some of the major application of SAW devices [7], [8]. The working frequency for the aforementioned applications exists mostly in the range of 300 MHz to 10 GHz, where the conventional band-pass filters experience huge losses. Using a ceramic material based electromagnetic filter which possesses a superior power control ability can be a solution to such issues. In contrast, they are large in dimensions and hence not feasible for use where there is a need for effective miniaturization. Another advantage of SAW device is the adjustment between the miniaturization and large frequencies.

Table 1.1: Principle applications of SAW devices.

Systems and Infrastructures	Mobile Communication	Multimedia Applications	Sensors and Actuators	Remote Control	Automotive Sector
WLL and WiMAX	WCDMA systems	Digital audio and video	Chemical and biochemical sensors	Tag RFID	Remote key
WLAN/Blutooth	Mobile telephones	Digital television	Microfluidic actuators	Remote switches	Tire pressures sensors
GPS					Wireless audio
Radar					

Instead, in the past few years, SAW devices have also been used in sensor systems in addition to the prevalent communication devices [7]. In fact, almost every acoustic wave device can be called sensors where the wave propagation features are extremely receptive to minor alteration along the propagation path. Therefore, these devices can be improved to possess very high sensitivity in response to small changes in the surrounding medium. Variation in the features of the acoustic wave propagation medium lead to adjustments in the wave velocity and amplitude or both, resulting in a modification of output signal in terms of phase shift or wave dampening. Accordingly, SAW devices have found widespread use in various other applications relating to chemical, biochemical and physical sensor applications for example, gas [9], pressure and temperature sensors [10]. Moreover, SAW sensors can also be employed in harsh environments where the sensors have to endure extreme conditions of electromagnetic fields, heat or radiations.

Sensors based on Rayleigh waves or surface acoustic wave devices, named after Lord Rayleigh, who first confirmed its presence in 1885 [11], have shown immense potential for applications related to production and transportation engineering, environmental monitoring and safety because of their direct response to physical and chemical parameters. The device comprises of electrodes (interdigital transducers) structured on a piezoelectric substrate. Because of the piezoelectric effect, application of a RF voltage between the two-opposing electrode 'combs' generates a surface acoustic wave and vice-versa. Any physical/chemical quantity that influences the surface acoustic wave can thus be sensed based on the modification of the electric signal. In the past years, SAW-based temperature sensor devices have received much attention, mainly because of it being a wireless and passive device and at the same time inexpensive and robust. The efficiency of a SAW

sensor can depend on multiple factors such as higher operating frequencies, wider bandwidths and lower insertion losses which in turn depend upon the transport of input and output signals which further depends on the medium (material) through which the wave propagates. So, on the root level, it is the material compatibility which plays a significant role in defining the performance of a SAW sensor device.

Every SAW-based sensor device uses a piezoelectric material as a substrate, such as quartz crystal (SiO_2), lithium tantalite ($LiTaO_3$), lithium niobate ($LiNbO_3$), lead zirconate titanate ($Pb(Zr,Ti)O_3$, PZT), (Al, Ga)N, ZnO, and SiC to produce the acoustic waves [6]. Langasite ($La_3Ga_5SiO_{14}$), langatate ($La_3Ga_{5.5}Ta_{0.5}O_{14}$) and langanite ($La_3Ga_{5.5}Nb_{0.5}O_{14}$) have quite high electromechanical coupling coefficient, and can operate at temperatures up to 850 °C making them promising candidates for high-temperature SAW devices [12]. In addition to the substrate, another part which plays a major role in sensing applications is the Inter-digital transducers. These electrodes are used for the excitation and detection of SAW's. Since the IDT's of a SAW device are attached directly on the oscillating section of the SAW, the electrodes are continuously exposed to high temperature environment inducing thermal stresses and vibration and consequently may get physically damaged (owing to stress migration) when subjected to large input power and temperature. Thus, most of the research work in this field is focused on the development of new functional piezoelectric materials with improved electroacoustic characteristics and high temperature stable thin film materials for the IDT for the fabrication of high frequency devices with enhanced performance and also with low fabrication cost [13]. Conventional metallization materials like Al, Cu, Ag and Pt undergo thermal damage [14][15]. The most promising of these is Pt, however, studies show that Pt fails due to diffusion and agglomeration due to its weak chemical affinity to the substrate above 600 °C [15]. Thus, achieving such sensors with long-term stability and reliability is still of major concern and opens up a wide area in search of suitable IDT material for high temperature applications. The main limitations for the use of such nanocrystalline metal films are related to stress-induced damaging processes, manifested as voids, hillocks, and mechanical hysteresis that lead to the structural failure and thus consequently lead to the electrical failure of the device. An understanding of the thermo-mechanical behavior of the films is hence indispensable since most technical solutions fail in this field.

1.2 Objective

The appeal for achieving effective and inexpensive SAW-based temperature sensors that can monitor the conditions in chemical and physical processes with the intention for its application in automobiles, medical devices and other automated industry setups has been the major motivation behind this work [16].

The main issue in this field of high temperature SAW sensor devices is the attainability of metallisation electrodes that are stable at high temperatures (about 800 °C) for long working durations. Since the thin-film electrode dimensions in such sensors are only a few nanometers (<100 nm typically), material migration related damage of the electrodes at high temperatures is the predominant cause for device failure. It is thus paramount to first understand and address these failures in thin films. Since the traditionally used metallisation materials such as Pt, Pd, Rh etc. have failed with respect to high temperature stability, search for better materials have gained impetus in the past few years.

In search of novel high-temperature stable materials, this work focuses on the nanostructured molybdenum-lanthanum oxide multilayer thin film systems. The aim of this project is to study the thermal stability provided by the possible oxide-dispersion strengthening mechanism in these thin films for the above mentioned high temperature application. Focus will be placed on understanding the recrystallization and grain-growth at elevated temperatures in the multilayer thin film system. The studies will involve thin film deposition using magnetron sputtering and its characterization using X-ray diffraction, X-ray reflectivity, atomic force microscopy, scanning and transmission electron microscopy to understand the film microstructure in the as-deposited state and then upon heat treatment. Since the electrical properties of the electrodes are also important for their applicability, the electrical conductivity has been studied after subjecting the electrodes to heat treatments.

The major goals of this dissertation work are:

1. Deposition and characterisation of damage free 100 nm thick Mo-La_2O_3 multilayer thin film deposited on Si using PVD (Physical Vapor Deposition) technique.
2. Understanding their recrystallization and grain growth at elevated temperature of 800 °C with different heating duration for different film configurations in order to understand the influence of La_2O_3 on Mo.

3. Studying the electrical behaviour and residual stresses in these films in as-deposited and annealed condition.

1.3 Thesis Outline

The thesis is organized as follows. The Introduction chapter briefly describes the evolution of the SAW applications and the importance of thin film technology for high frequency SAW devices fabrication for sensor applications. Chapter 2 & 3 presents the literature review on SAW, Mo-La_2O_3 material system, thin film deposition process, film growth and microstructural evolution, properties and the well-known size effect in thin films. Chapter 4 discusses the methodology followed to fabricate the nanostructured multilayer metallization system, process parameters details regarding the deposition Mo-La_2O_3 film stack and the characterization techniques to evaluate the films. The results obtained after the characterization of the Mo-La_2O_3 multi-layered films and discussion of those results are presented in Chapter 5. Finally, in Chapter 6, the principal conclusions of this thesis work have been included along with the scope of the future work presented in Chapter 7.

2. Surface Acoustic Wave Device - An Introduction

Surface Acoustic Wave (SAW) based devices have gained significant importance in the electronic industry since the 1970s. It has been widely used in RF filters, microfluidic systems, sensors and actuators for detecting various environmental variables such as temperature, chemicals, gasses and mechanical stresses. SAW devices are also used as bandpass filter elements in radar systems and televisions. SAW sensors can operate wirelessly and passively, which demonstrate an advantage over wired sensing solutions. It is one of the most promising detection systems due to their smaller size, low weight, minimal power requirements and high sensitivity.

2.1 Working of a SAW device

Like throwing a rock into a lake can generate waves, tapping a desk surface can induce vibrations in the nearby region. Similarly, an elastic body can also stimulate a wave on its free surface whose movement is contained in the neighbouring area.

SAW devices consist of metallic interdigital transducers (IDT) thin film electrodes that are structured as opposing combs on a single crystal piezoelectric substrate. An electric RF voltage applied between two opposing IDT combs is converted into a surface acoustic wave and vice-versa because of the piezoelectric effect of the substrate material. When an electric field is applied to the input electrode or IDT, the substrate material experiences deformation (mechanical stresses) which in turn causes the surface acoustic wave to traverse over the surface with same frequency as that of the applied field [3].

The IDT electrodes are in the shape of a comb, the teeth of which is arranged such that spacing between them is equivalent to one pitch. When wavelength of the wave generated equals the pitch of the electrode, the distortion developed on the piezoelectric crystal is the strongest. Figure 2.1 shows the schematic and working principle of a SAW device.

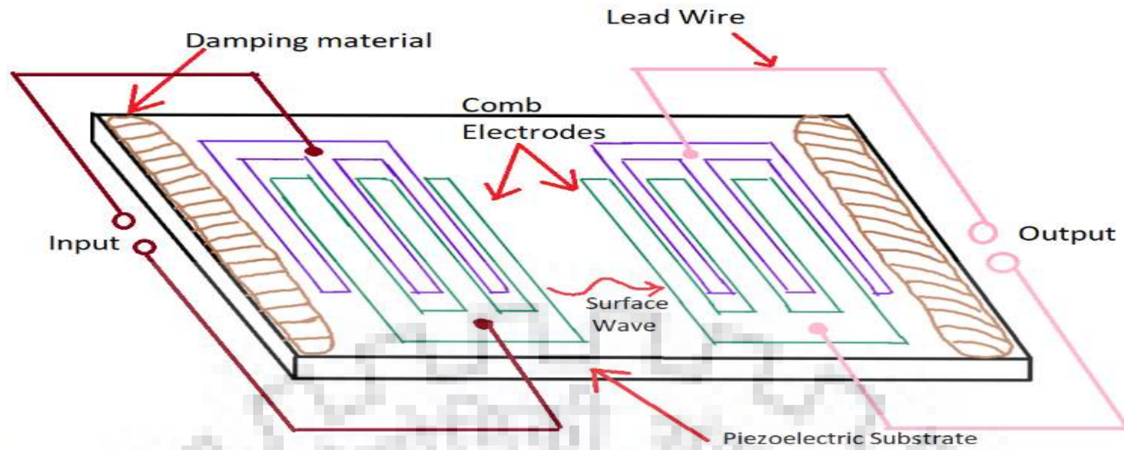

Figure 2.1: Basic Structure of SAW device.

2.2 Materials for SAW devices

2.2.1 Choice of substrate

For SAW device design, a structurally uniform (defect free) piezoelectric single crystal substrate or a non-homogeneous structure consisting of multiple layers (preferably epitaxial) of different materials can be used.

An appropriate substrate material for the SAW device is the one which has high wave propagation velocity, highest electromechanical coupling coefficient or bonding, least temperature coefficient of delay/maximum temperature coefficient of frequency, and minimum wave attenuation rate. Presently, there is no such material present which satisfies all the requirements together and ultimately the material selection becomes the subject of compromise.

Table 2.1 displays the list of vital characteristics of some piezoelectric materials used as a substrate for SAW devices. From all the materials listed, PZT shows the highest EMCC (Electromechanical coupling coefficient, k^2) and AlN has the highest wave velocity. Quartz has been extensively used as a substrate material since it shows very low temperature coefficient of frequency (TCF) which eventually provides an improved thermal stability for accurate sensing requirements. Substrate such as X-112° Y-cut $LiTaO_3$ and 128° Y-X-cut $LiNbO_3$ can easily generate Rayleigh waves. In addition, shear horizontal-SAW can be generated on 64° Y-X-cut $LiNbO_3$ and 36° Y-X-cut $LiTaO_3$ substrates.

Table 2.1: Substrates used for acoustic wave generation [17].

Crystal	T_c/T_m (°C)	k^2 (%)	V (m/s)	TCD (ppm/°C)	ρ (μΩ.cm) at 300 °C	CTE (x 10^{-6} /°C)	Comments
Quartz (ST)	~573	0.11	3158	~0	~2.0 x 10^{16}	1.5	Crystal twinning at ~300° & Phase transformation
LGS (48.5° rot Y)	~1470	0.44	2400	4.34	~8.0 x 10^{14}	5.8	Disordered structure; low resistivity
$GaPO_4$ (Y)	~933	0.29	2400	~0	~2.0 x 10^{18}		Phase Transformation
CTGS	~1350	15.0	2771	37.1	~1.0 x 10^{17}	-	Ordered structure
$LiNbO_3$ (Y)	~300	4.5	3488	94	-	15	Decomposition
$LiTaO_3$ (X)	~300	0.9	3295	18	-	16.5	Decomposition
(Al,Ga)N	≥1000 (AlN)	0.6	≈6000 (AlN)	28.3	~1 x 10^{19}	4.6 (AlN)	Phase Transformation

For high temperature applications (> 600 °C), choosing an appropriate substrate becomes important as conventional materials cannot be utilized. For example, Quartz, a most widely used piezoelectric material has a crystal phase transition from α to β at 573 °C [18] while substrates like $LiTaO_3$ and $LiNbO_3$ lose their piezoelectric effect or decompose at high temperatures. In search of high-temperature stable piezoelectric materials, recent studies have shown that LGS ($La_3Ga_5SiO_{14}$) and CTGS ($Ca_3TaGa_3Si_2O_{14}$) have favourable high temperature properties and are promising candidates for high temperature applications based on SAW devices [19]. The increasing interests and widespread use of these piezoelectric materials has been attributed to its high temperature stability with the nonappearance of phase transformation till its melting point at 1460 °C [20].

2.2.2 Choice of transducer

The selection of a potential electrode material for SAW IDT's involves several important factors such as ease of deposition, good adhesion to the substrate, non-reactivity with the substrate material and in case of high temperature application, the ability to resist degradation after short-term high-temperature cycles and long-term stability at the operating temperatures.

The most commonly used electrode material for IDT's is aluminium and is the typical choice for operations below 200 °C owing to its low density and high electrical conductivity. Nevertheless, aluminium fails and becomes soft at temperatures even below 200 °C because of electro- and acousto-migration [21].

Other natural candidates of SAW transducer material for high temperature application up to 800°C include platinum and palladium [22]. Owing to high melting point and its inertness, platinum has been

preferred as a possible electrode material over others for temperatures above 300°C [22]–[24]. However, it was observed that Pt electrode having thickness less than 100 nm, agglomerates (de-wetting) at temperatures above 700 °C due to surface tension, disrupting the film uniformity, and finally resulting in a complete loss of electrical continuity [25]. Nevertheless, by proper alloying, the agglomeration can be avoided [23]. In addition, iridium and platinum with titanium adhesion layer electrodes can sustain even higher temperatures.

Thiele et al. [22] studied the effect of Zr & Ti as an adhesion layer for IDT's with Pt and Pd electrodes over LGS. It was found that on long exposure to high temperatures, the adhesion layer of Ti migrates into Pt resulting in poor linkage and weakening of the SAW transducer performance. However, Zr having similar adhesion characteristics does not migrate into the Pt layer [26]. Moreover, typical metallic adhesive films, such as Ti:W alloy or Cr can form a network and migrate into Pt at large annealing temperatures resulting in adhesion failure by lowering the temperature coefficient of resistance (TCR). Extensive blistering/delamination or agglomeration can occur at elevated annealing temperatures in the absence of adhesion promoter [27].

Various other metal doped oxides based thin film IDT electrodes have been investigated such as $PtAl_2O_3$, Pt-Rh/NiO, Pt-Rh/CoO and Pt-Rf/HfO_2 using co-deposition method [15]. A comparison of few metal electrodes for SAW IDT's has been listed in Table 2.2.

Table 2.2: Characteristics of metals for the SAW IDT's [28].

	ρ (μΩ.cm)	**Phase Velocity (m/s)**	**Poisson ratio**	**Density (10^3 kg/m^3)**	**Young's Modulus (GPa)**	**Acoustic impedance, Z (10^6 kg/m^2 s)**
Al	2.82	6350-6500	033	2.695	76	17.65
Ti	42	6100	0.32	4.48	110	27.33
Ru	7.1	1200	0.3	12.2	220	27.57
Ag	1.59	3600	0.37	10.6	100	38.16
Hf	33	3010	0.37	13.3	110	40.03
Ni	6.99	5600	0.31	8.84	200	44.20
Cu	1.7	5010-5200	0.355	8.96	128	44.89
Cr	12.5	6650	0.21	7.19	140	46.74
Au	2.44	2650-3210	0.42	19.32	78	51.20
Pt	10.5	3260	0.38	21.14	170	63.42
Mo	5.3	6290-6700	0.307	10.28	230	63.74
Ta	13.2	4100	0.34	16.6	200	68.06
W	5.6	5200-5500	0.28	19.25	410	92.40
Ir	4.7	5350-5560	0.21	22.3	525	118.19

Potential electrode materials can be classified into 3 groups: metal (e.g. W, Mo, Cu, Ti, Pt), alloys (e.g. RuAl, TiAl, CuAl, NiCr) and metal non-metal compounds (e.g. Pt-Rh/CoO, Pt-Al/Pt/ZrO_2, Pt-Al_2O_3, Pt-Rh/HfO_2). For high temperature applications, the most suited metals are the one which have high melting point with noble character, e.g. Platinum (Pt), Rhodium (Rh) & Iridium (Ir). There have been numerous studies on the some of these high temperature materials for electrode fabrication [29]–[31]. Gayatri et al. [29] studied Mo/W metallization system as an alternative IDT material for SAW based high temperature sensors because of its capability to withstand high temperature (~1000°) along with better adhesion to the substrate and least degradation driven by responses such as acousto, thermal and electromigration, possibility of agglomeration, void formation thereby maintaining a constant electrical resistivity. The bulk properties of Mo such as high melting (2623 °C) than that of Pt (1768 °C) and higher thermomechanical stability make it attractive for use in SAW application. Another property of Mo that reduces the agglomeration and slows down grain boundary grooving is the activation energy for self-diffusion of Mo (5.8 eV) compared to Pt (3 eV). The higher thermal conductivity of Mo (139 $Wm^{-1} K^{-1}$) as compared to Pt (72 $Wm^{-1} K^{-1}$) lowers the temperature gradient in SAW based temperature sensors. Additionally, other properties such as electrical resistivity and thermal expansion coefficients of Mo is much lower than that of Platinum which makes it a promising candidate for such applications. Comparing with the other low melting and low resistivity metals such as Cu and Al, Mo in the pure bulk form has a high resistivity of 5.78 μΩ cm, therefore a trade-off between high temperature stability and the lower film resistivity needs to be appreciated in addition to other parameters that could influence the microstructure of the films.

3. Mo-La_2O_3: Potential Metallization System

3.1 Introduction

Thin film technology has played an exceptionally significant role in the advancement of electronic gadgets due to the realization of real-world applications in the engineering systems which depends mostly on the polycrystalline thin films with thickness ranging from nm to µm. Thin film properties can be tailored by varying the deposition conditions. Functionality in the film structure can be obtained by depositing multiple layers of different materials. By combining different metals, insulating and semiconducting layers collectively, the practicality of the electronic devices can be clearly recognized. One of the usual method for achieving the desired properties from these layers is by performing the so called 'micro and nanostructuring' [32].

The structuring is pretty much valid for most of the microelectronic gadgets having surface coatings with electrical, thermal and mechanical functions. Metal based thin films have been extensively used for performing high end performance in field of electronics in comparison to other films. Applications of these thin films in the field of SAW technology is related to the IDT metallization, cover and barrier layers for preventing degradation by agglomeration and migration phenomenon that arises at harsh environment conditions.

Speaking of harsh environment, it is known that high temperatures adversely affect device performance. This calls for a material system that can be stable, conducting and at the same time functional at high temperatures without any material degradation. Metals such as molybdenum (Mo) & Tungsten (W) have recently received much attention and have been used in areas such as memory device, solar cells, etc. due to their good thermal stability and low contact resistance [33], [34]. Mo films are frequently the main choice in various electronics applications because of their attractive functional properties. These films serve as the electrode materials in piezoelectric micro and nano electromechanical devices due to their low resistivity and high acoustic impedance values [35], [36]. Mo films also finds applications as the metallization system in thin film transistors i.e. in gate electrodes and as a diffusion barrier layer [37]. Lately thin films of molybdenum have attained industrial significance as a linking material for ICs, environmentally protective coatings, contact film for solar cells owing to high strength at elevated temperature, low thermal coefficient of expansion, high conductivity and resistance to creep [32], [33]. However, commercially pure molybdenum has

low strength at elevated temperatures. Depending on the amount of work hardening Mo usually recrystallizes between 900 and 1250 °C. The use of pure Mo in structural and electronic based applications has been limited due to the decrease in strength with recrystallization [34]. Although Mo has a high melting point of 2896 K, it loses its strength and fails already at 800 °C.

Another major impediment in the use of Mo thin films in flexible electronics is its mechanical failure through brittle fracture. To overcome this issue, various approaches have been adopted for improving the behaviour of Mo films. Mo, a refractory metal from group VI of the periodic table, can be strengthened by (a) solid-solution strengthening additions, (b) precipitation or dispersion strengthening by second-phase particles, (c) strain hardening and grain size refinement, and (d) retaining a worked structure at high temperatures. For service at elevated temperatures ($>0.5T_m$), only a combination of (b), (c), and (d) has the potential for success. Strengthening by second-phase particles can be both direct and indirect. Direct strengthening is caused by particles acting as barriers as to dislocations motion during deformation. Indirect strengthening is caused when a dispersoid-containing metal is thermomechanically processed, so that the particles help to develop and stabilize a worked structure. An additional strength increment resulting from the fine grain size and substructure can be achieved at high temperature if the structure is stable.

Carbides have been the favoured second-phase particle for strengthening molydenum, as is evident in the Mo-TZM (Titanium-Zirconium-Molybdenum) and Mo-TZC (Titanium-Zirconium-Carbon) alloys [38]. However, the carbide particles are not stable at high temperature and will coarsen and/or dissolve into solution, thereby negating their effective need as a strengthener. Inert oxide particles are preferable as the dispersoid. It has been observed that alloying Mo with Re improves the room temperature ductility thereby increasing the workability and toughness of the alloy [39]. Recently alloys strengthened by addition of oxide particles have received considerable attention owing to their excellent creep properties. Lanthanum oxide doped molybdenum is one such ODS alloy which has been the interest of study for applications as furnace components, sintering boats, feed wires in the lighting industry, high temperature springs, welding electrode material etc. [40]. In order to use Mo for applications concerning operating temperatures more than the recrystallization temperature, various alloys have been developed by dispersion strengthening using rare earth oxides such as La_2O_3 and Y_2O_3 thereby providing superior ductility and creep resistance properties [41]. Zhang et al. [42] reported that in bulk molybdenum toughness can be improved by the dispersion of second phase La_2O_3 in the parent matrix. It was found that the for Mo-La_2O_3 alloys, particles dispersion strengthening is much more effective than compared to grain size refinement [36]. However, studies on thin films of Mo with oxide dispersion is still lacking. It would be interesting to study if such parallels can be drawn

for thin film systems as observed in bulk form. Thus, the aim of this work is to develop a high temperature stable IDT metallization system by incorporating a second phase particle (La_2O_3) into thin film of parent metal (Mo) matrix using thin film deposition of magnetron sputtering. Additionally, these films have to be tested for electrical and thermal behaviour at elevated temperature of 800 °C.

3.2 Mo-La_2O_3 material system

In order to improve the mechanical properties of Mo metal in terms of high temperature strength, creep resistance, and ductility, use of oxide dispersion strengthened (ODS) Mo alloy is particularly of interest. Though significant amount of studies has been conducted on this material system in bulk form, investigations based on nanostructured thin films is still lacking. It would be interesting to note the behaviour of the material system in the nanoscale dimension.

Stable oxides of rare earth-metals have melting temperatures close to Mo and thus are logical choice for dispersion strengthening. It has been observed that ODS Mo prepared by doping appropriate quantity of rare earth oxides such as La_2O_3, Y_2O_3, when deformed exhibits a much higher recrystallization temperature than the commercially available pure molybdenum [43]–[45]. This makes ODS Mo demonstrate not only higher non-sag property and creep strength at elevated temperatures but also increased strength and ductility at low temperatures as compared with the pure Mo [46]. Deng shiqiang et al. [47] believed that rare earth might reduce the density of N, O, C, on the grain boundaries, whereas Zhang at al. [46] observed that the presence of second phase particles of La_2O_3 as the major input to Mo toughness enhancement. It has been found that creep-rupture life of pure molybdenum at $0.65T_m$ (where T_m is the melting temperature) i.e. 1600 °C increases only by an order of magnitude on adding 50 wt.% of Rhenium. Nevertheless, an ODS Mo alloy at 1800 °C shows the creep strength several orders of magnitude more than unalloyed Mo [48]. Actually, the oxide dispersion strengthened molybdenum has a high creep-rupture at 1800 °C compared to unalloyed W or Re at 1600 °C. Endo and others [45] investigated the microstructural and mechanical behaviour of molybdenum thin wires doped with lanthanum oxide particles and found that recrystallization temperature increased to 1500-1600 °C from 1100-1200 °C for undoped wire. Besides, the increase in the recrystallization temperature, the shape of the recrystallized grains changed after the dispersion of the oxide phase. Bianco et al. [48] compared the effect of adding different oxides such as La_2O_3, Y_2O_3, and Zr_2O_3 in the molybdenum matrix and observed that doping with La_2O_3 exhibited highest ultimate tensile strength (UTS) along with increase creep rupture strength when compared with other oxide

additions. The commercial production of lanthanum doped ODS alloys are presently carried out using the powder processing techniques. The amount of La_2O_3 added into the Mo matrix affect the properties of the alloy in a substantial way. It has been observed 0.6 - 1.5 wt.% of lanthanum oxide when added to the Mo metal in the bulk form, gives the best combination of thermos-mechanical properties [49]. In this thesis work, about 1 wt.% of lanthanum oxide in Mo thin films has been studied.

3.3 Thin film synthesis methods

For the fabrication of thin functional layers, various vacuum or non-vacuum-based methods can be opted such as physical vapor deposition (PVD), chemical vapor deposition (CVD), atomic layer deposition (ALD), pulsed layer deposition (PLD), wet and dry chemical deposition. PVD is one of the commonly used method for the deposition of thin films. PVD can be classified further into three main processes, namely ion-beam etching, sputtering and evaporation. Sputtering being the most frequently used method for the fabrication of thin metallic and non-metallic films. This deposition technique can be extended to various other materials for instance, insulators, alloys, organic blends and semi-conductors etc.

Though there are different methods for film fabrication, each method can be visualized in a three sequential step process: (1) A thin film material source is provided, (2) the material is transported onto the substrate surface and (3) film growth occurs. The uniformity of the film will depend on the deposition parameters and material transport. The medium of transport (vacuum medium) also plays an important role in defining the film uniformity by affecting the deposition rate, energy and material flow direction. In the PVD process, a target source is bombarded by ions leading to sputtering out of the target atoms and its deposition onto a substrate to form a thin film on its surface. Sputtering technique will be used as the deposition method for film fabrication in the present work [32].

Sputtering is basically ejection of material from a solid surface because of impingement of the same by highly energetic projectile. The Ar ions strike the target surface acting as cathode in the sputtering chamber. The flux of the sputtered material is intercepted by the receptor surface of the substrate. The cathode current, discharge voltage, process pressure and stand-off-distance (SOD) are the main process variables. A mono phase or multiphase coating can be deposited by sputtering. It can also be extended to deposit multilayer or graded layer coating. Substrate bias and substrate temperature have strong influence on coating properties. The thickness of the sputtered films can vary from 1 nm up to several

μm. Physical sputtering is a process which occur under high vacuum conditions. Most plasmas are formed by electron impact ionization of the gas in a controlled electrical gas discharge, when Ar is the gas, the ionization can be described as:

$$e^- + Ar \rightarrow Ar^+ + 2e^- \quad 3.1$$

Moreover, the flux of particles onto a surface at a given pressure p is given by:°°°

$$\Gamma = \frac{p}{\sqrt{2\pi mkT}} [m^{-2}s^{-1}] \quad 3.2$$

where m is the mass of the element, k is the Boltzmann constant, and T is the temperature in Kelvin. Generally, in a DC sputtering system, the target is kept as cathode and the grounded chamber walls acts as the anode. When a negative potential is applied to the cathode, the electric field created between the electrode accelerates all the charged particles. The energy and momentum transfer from the particles enables the escape of the surface atoms of the source. These atoms will then condense and nucleate onto the substrate located opposite to the target [50]. Figure 3.1 shows the schematic of the reactive sputtering process.

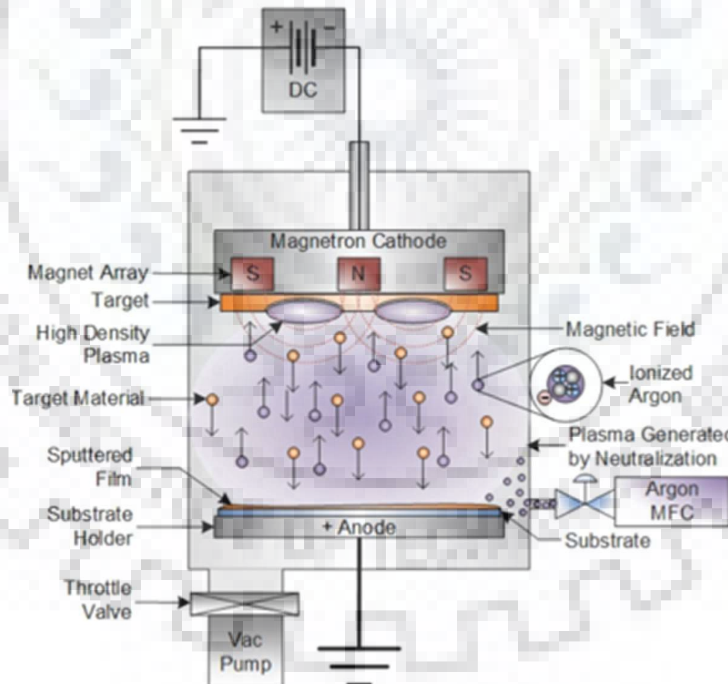

Figure 3.1: Schematic of a DC magnetron sputtering process [51].

A lot of different thin film deposition techniques have been reported in literature for metal doped oxides by sputtering, sintering powder blends PLD, CVD and ALD [52], [53]. Sputtering process is

usually characterized by discharge voltage, argon pressure, discharge current and deposition rate. The magnetron sputtering source further reduces the requirement of high discharge voltage and argon pressure & significantly improves the quality of the film/coating. The presence of a magnetic field near the target surface intensifies the plasma by trapping the electrons leading to increase in ion impingement and sputtering rate.

3.4 Thin film growth

The growth of the thin film can be distributed into four main growth stages as shown in Figure 3.2. The stages include nucleation of island structure, coalescence of islands, channel formation, and formation of the continuous film. Thin film formation initiates with the deposited atoms colliding with the substrate surface and developing as isolated atomic clusters. These clusters start to combine to form larger islands and then these islands coalesce to form a film. Once a continuous film is formed, it starts to thicken and grow [54]. The microstructure of the film will depend on the efficiency of the atom to stick together.

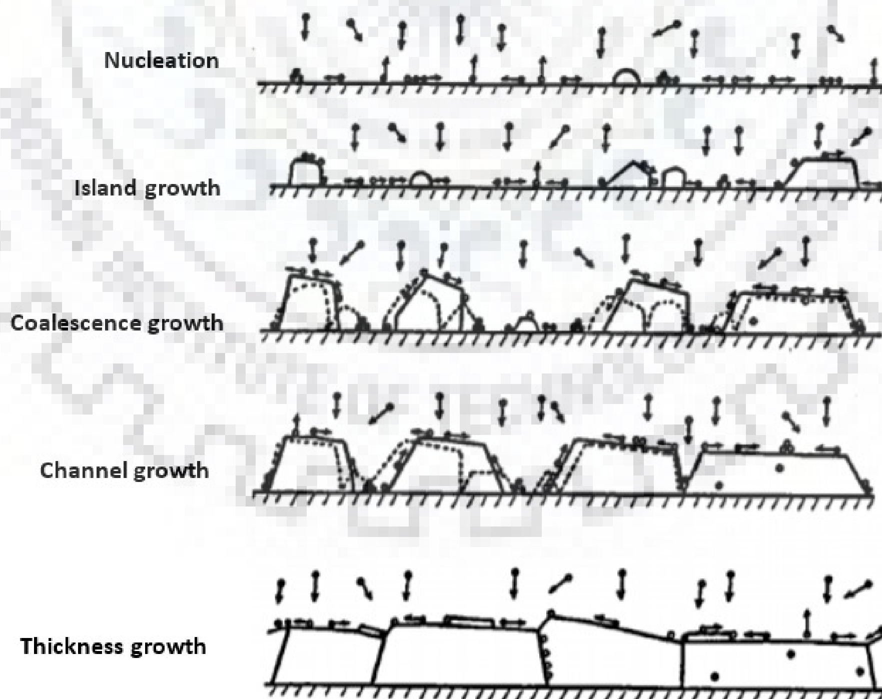

Figure 3.2: Schematic illustration of the growth process [54].

In sputter deposition, films are often deposited at a substrate temperature T_s which is lower than the film melting point T_m. Because of this difference, the sputtering process deviates far from the thermodynamic equilibrium. Figure 3.3 shows the different microstructures obtained from a PVD process. One axis of the graph represents the ratio of substrate temperature T_s to the film melting temperature T_m and the other axis represents the working gas pressure. Typically, at low deposition temperatures the mobility of the incoming atoms is limited. Hence, the obtained film is likely to be less dense, with columnar growth structures separated by voids. This kind of microstructure can be interpreted for zone 1 in Figure 3.4, comprising of tapered columns with curved tops demarcated by voided boundaries. Zone T is a transition state between zone 1 and zone 2, its grains are fibrous and dense. As temperature rises, width of the column increases defined by grain boundaries which is accounted for zone 2 ($0.3 < T_s/T_m < 0.5$). Zone 3 ($T_s/T_m > 0.5$) corresponds to elevated temperature which accounts for equiaxed grains that increases in size with activation energies similar to that of in bulk diffusion.

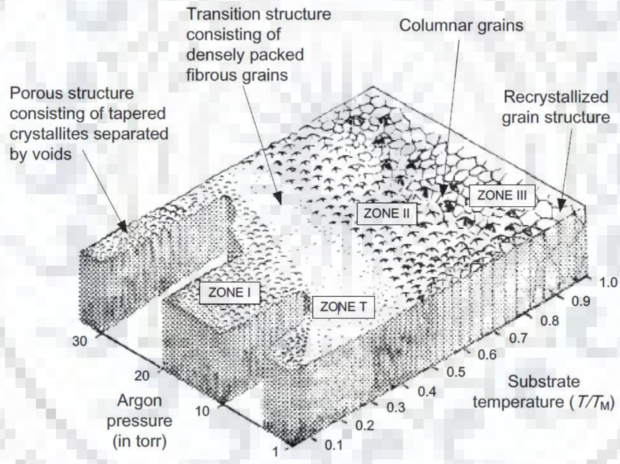

Figure 3.3: Structure zone model for metal films [55].

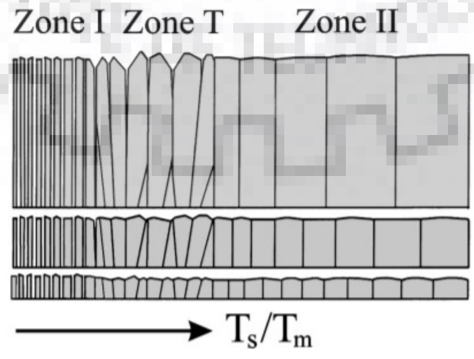

Figure 3.4: Schematic diagram of microstructure evolution [54].

3.5 Stresses in thin films

Owing to various constraints frequently forced throughout the thin film deposition process, non-equilibrium microstructures can result that cause stress levels to rise much above the corresponding yield/bulk stress which further can affect the film performance and reliability. Stresses in thin films can usually be differentiated as extrinsic or intrinsic. Stresses that occur due to external load are termed as extrinsic stress. For example, thermal stress arising from the difference in coefficient of thermal expansion of the film and the substrate material is one of the most common source of extrinsic stress. On the other hand, intrinsic stress is the stress arising from the inside of film structure while growing i.e. the growth stress. Much is yet to be understood based on intrinsic or growth stress due to the complexity of its generation and related microstructural changes during the film development [56]–[58]. Collision and infringement of the crystallite may result in tensile stress generation which has been documented both theoretically and experimentally for stress evolution characteristics [59].

Desirable or not, internal/residual stress is always present in thin films. Even without the application of external load, stresses may be present in the films as a result of differential thermal expansion between the film and substrate (Figure 6(c)), lattice parameter mismatch, inclusion of foreign atoms, interatomic spacing within the crystal, presence of microscopic voids, atomic peening, recrystallization or phase transformation [59]–[61].

The residual stresses in thin films can be either tensile or compressive as illustrated in Figure 3.5 (a) and (b). If the magnitude of stress is large, it could either result in film, substrate fracture or interface break up. As per the minimum energy theorem, the elastic solid body is said to be in equilibrium when the potential energy of the system is minimum. In other words, when the material is experiencing any residual or externally applied loads, the system would like to find the equilibrium position by rupturing in such a way that results in the decrease in potential energy [62]. So, to achieve the state of minimum energy, the strain energy produced by residual stresses can be reduced by delamination or rupture of the thin film. In worst cases, compressive residual stresses may result in film buckling and delamination from the substrate and tensile stresses may cause film cracking and peeling from the substrate [63]. In addition, the presence of residual stresses in films could also lead to generation of imperfection and defects in epitaxial layers by forming whiskers and hillocks [64]. All these responses to the presence of residual stress may alter the film properties such as electrical conductivity, magnetization and reflectivity [59].

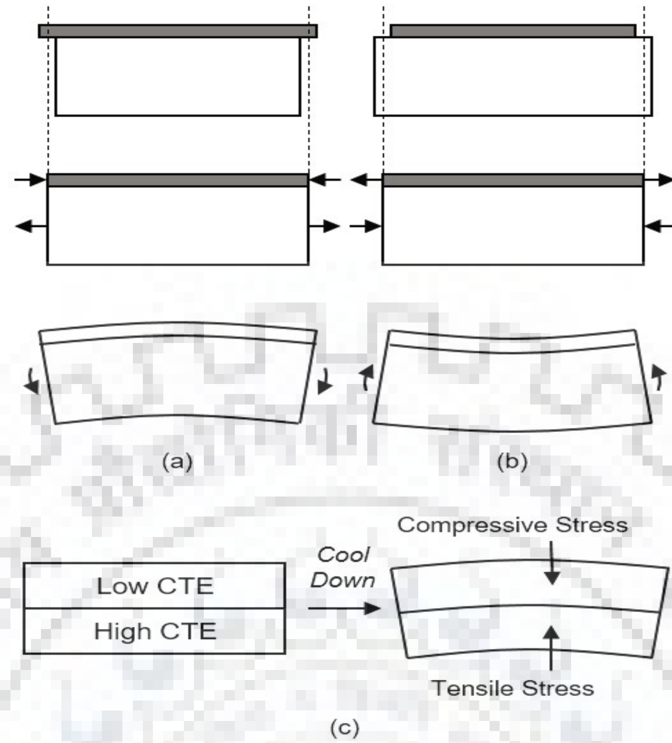

Figure 3.5: Illustrations of film/substrate bending due to (a) compressive, (b) tensile residual stresses in the film and (c) due to mismatch of the coefficients of thermal expansion (Adapted from Ref. [64])

The easiest and the most typical method to evaluate the film stress is to measure the substrate curvature before and after deposition. The change in curvature will indicate the presence of stress in the film resulting from the deposition process. A simple and famous formula that relates the film stress with the change in curvature of the substrate was given by G. G. Stoney [65]. Stoney made use of the plate theory to explain the system consisting of a thin film of thickness h_f deposited over a thicker substrate of thickness h_s and gave a well-known formula, what is identified as Stoney relation:

$$\sigma_f = \frac{E_s h_s^2}{6(1-\nu_s)h_f} r \qquad 3.3$$

where the subscripts f and s denote the film and substrate, respectively, whereas E and ν denotes the Young's modulus and Poisson's ratio respectively. σ_f is the film stress which is directly proportional to the substrate curvature, r. Stoney's relation has been formulated based on some explicit assumption. They are:

1. Both h_f and h_s are uniform and $h_f << h_s << R_s$, where R_s refers to substrate radius of curvature;

2. Film and substrate material is isotropic, homogeneous and elastic;

3. The rotations and strain in the system is negligible;

4. The misfit strain is equi-biaxial or in-plane isotropic and is constant over the plate's surface.

3.6 Size effect in thin films

The electrical conductivity of thin films exhibits a well-known size effect which is the result of electronic movements and scattering though the film surface and interfaces. Substantial effort has been put in the field of electron transport over several decades. Roughness, grain boundary scattering, impurity scattering, and surface scattering are the four-crucial electron scattering mechanisms which have been known to contribute to the classical size effect [66]–[68]. This classic 'size effect' defines the increase/decrease in the resistivity values based on the size of circuit feature. The increased resistivity effect is more pronounced when the dimension of the thin films becomes twice to thrice of the electron mean free path (EMFP). The size effect usually leads to an increase in the resistivity values when compared to that of bulk. With upgrading technologies and the need for nanoscale dimensional features, the size dependent resistivity has a critical role to play in the microelectronic industry.

The resistivity size effect in nanoscale systems occurs mostly due to the electron momentum loss during the flow of electron resulting from grain boundaries and surface scattering. To explain this electron scattering phenomenon in thin film system, two widely used theoretical models are used, the Fuchs-Sondheimer (FS) model [69][70] which relates to surface scattering and the Mayadas-Shatzkes (MS) model [71] which is based on the grain boundary scattering principle. The major assumptions of these two models are that the scattering process is isotropic and the size effect is dependent on the free electron theory.

In FS model, the resistivity of the film, ρ_{film} can be obtained using the bulk resistivity data using the following equation:

$$\rho_{film} = \rho_{bulk}\left[1 - \frac{3}{2s}(1-p)\int_1^{\infty}\left(\frac{1}{t^3} - \frac{1}{t^5}\right)\frac{1-e^{-kt}}{1-pe^{-kt}}\,dt\right]^{-1} \quad 3.4$$

$$s = \frac{d}{\lambda} \quad 3.5$$

where, p refers to the parameter indicating the number of electrons that are specularly scattered from the surface with values ranging from 0 to 1. Specular scattering (p = 1), refers to the elastic scattering

causing no change in the resistivity. Whereas, the diffuse scattering ($p = 0$) implies that randomization of the electron momentum leading to increase in the resistivity. s is the ratio between mean film thickness, d and the electron mean free path in the bulk, λ.

In contrast to FS model, the MS model is based on the electron scattering at the grain boundaries that are found typically in polycrystalline materials. These grain boundaries acts as potential barrier for the moving electrons which can either be transmitted or reflected. Assuming R as the reflection probability described by grain boundary reflection coefficient. Larger is the R, more is the electron scattering leading to increase in the electrical resistivity. Whether the scattering is specular or diffuse, all reflected electrons contribute to the increase in resistivity. Therefore, the film resistivity due to grain boundary scattering is given by:

$$\rho_{film} = \frac{\rho_{bulk}}{3}\left[\frac{1}{3} - \frac{\alpha}{2} + \alpha^2 - \alpha^3 \ln\left(1 + \frac{1}{\alpha}\right)\right]^{-1} \qquad 3.6$$

$$\alpha = \frac{\lambda}{D}\frac{R}{1 - R} \qquad 3.7$$

where, D is the average in-plane grain size. The presence of grain boundaries tends to reduce the electron mean free path value lower than that of bulk. Owing to the growth method in case of thin films, the mean grain size can become equal to the thickness if the thickness reduces up to 1 μm. As a result, thinner films will have smaller grain sizes indicating the presence of more grain boundaries that may result in the increase in the resistivity values. In almost all the cases, both grain boundary and scattering lead to the increase in the total resistivity value of the thin films.

4. Research Methodology and Experimental Procedure

4.1 Film preparation

Periodic multilayer films containing Mo and La_2O_3 in alternating pattern were deposited onto Si (100) substrate having 1 µm thickness of SiO_2 layer on the top. DC magnetron sputtering technique was used with pure Mo and La targets. Si wafers with thickness 530 µm and 250 µm were cut into square (10 × 10 mm) and rectangle (59 × 7 mm) shapes for the deposition respectively. The overall film was designed with different bilayer periods of Mo and La_2O_3 (1, 2, 4 & 8) with Mo as a top covering layer in each configuration. The overall thickness of the multilayer was kept 100 nm. All the deposited samples were vacuum annealed at 800 °C for different time duration of 24 h, 48 h, and 120 h. A total of 4 batch series were prepared with 1, 2, 4 & 8 bilayer periods, and analysed for microstructural, electrical and thermomechanical behaviour in as-deposited (AD) and heat-treated (HT) condition as shown in Figure 4.1. The thickness of individual layers was varied such that the film composition is kept constant. In the present work, a total thickness of 1 nm of La_2O_3 with 99 mm of total Mo thickness corresponds to approximately 1.1 wt.% of the oxide. To identify the respective samples, corresponding nomenclature was kept in the format of Mo-(La_2O_3-Mo)$_n$-Si, where *n* represents the number of alternating layers of Mo & La_2O_3 (bilayer period) in AD & HT conditions. In order to visualize the effectiveness of all these multilayer films, the present metallization system was compared to that of pure Mo in both AD and HT condition.

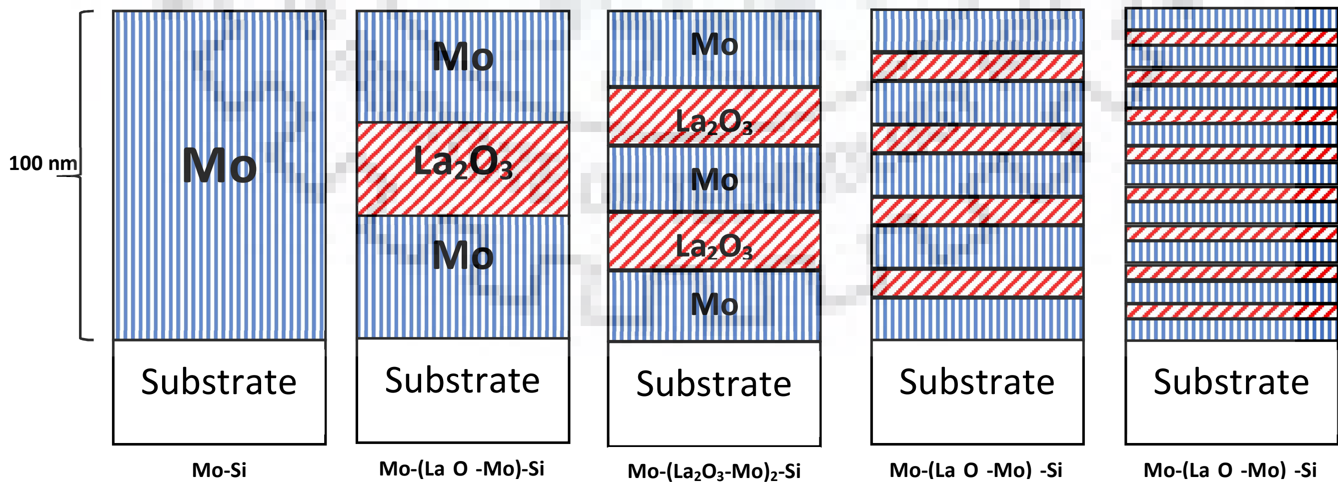

Figure 4.1: Designed multilayer film configuration.

Film fabrication was done using a DC magnetron sputtering system as shown in Figure 4.2. Before the deposition, the substrate was kept under high vacuum chamber at the base pressure of 2.6×10^{-6} - 3.0×10^{-6} mbar. Subsequently during the deposition, the chamber pressure was 1.6×10^{-3} mbar. This chamber has two planar sources for each of the material targets of pure Mo & La. Ar gas was utilized as the sputtering gas at a flow rate of 30 sccm for ionizing and creating plasma. The deposition was carried at input power of 500 W and 50 W for Mo & La respectively at room temperature conditions. The deposition rate chosen for the film fabrication was 0.478 nm/sec and 0.029 nm/sec for Mo and La respectively. The sample stage was rotated at constant speed of 10 rpm inside the sputtering chamber to obtain a homogeneous film. La is an extremely reactive material, it easily forms oxide when exposed to ambient atmosphere. It was observed that the residual oxygen in the (HV) deposition chamber was sufficient to oxidise La to La_2O_3. In order to achieve a completely oxidised layer, after deposition of the La layer, deposition was briefly interrupted so as to ensure the complete uptake of the oxygen by the deposited La. This was achieved by waiting until the chamber pressure reached to the set deposition pressure of 1.6×10^{-3} mbar. So, during the fabrication of film stacks, waiting time was introduced after the deposition of La layer in each case each time before depositing Mo layer on top.

Figure 4.2: DC magnetron sputtering system for Mo/La_2O_3 multilayer thin films.

The details of film configuration and sputtering parameters are shown in Table 4.1 & Table 4.2 respectively.

Table 3.1: Deposited thin film multilayer configuration details.

Film configuration	Mo-(La_2O_3-Mo)-Si	Mo-(La_2O_3-Mo)$_2$-Si	Mo-(La_2O_3-Mo)$_4$-Si	Mo-(La_2O_3-Mo)$_8$-Si
Mo total thickness (nm)	99	99	99	99
La total thickness (nm)	1	1	1	1
Mo individual layer thickness (nm)	49.5	33.0	19.8	11.0
La individual layer thickness (nm)	1	0.5	0.25	0.125
Total Mo layers	2	3	5	9
Total La layers	1	2	4	8
Total film thickness (nm)	100	100	100	100

Table 4.2: Sputtering parameters for deposition of thin film multilayers.

Operating Conditions (Mo/La)	
Sample dimension (mm^2)	10 x 10
Sputtering power (W)	500/15
Argon flow rate (sccm)	30
Chamber pressure (mbar)	$2.6 \times 10^{-6} - 3.0 \times 10^{-6}$
Deposition pressure (mbar)	$1.6 \times 10^{-3} - 1.8 \times 10^{-3}$
Deposition temperature (°C)	RT
Deposition time (s)	104/35; 69/17; 42/9: 23/4
Thickness (nm)	100
Waiting time after La deposition (min)	60; 45; 30; 25

4.2 Characterization of thin films

Characteristic investigation of the thin films is very crucial for understanding the underlying mechanism related to microstructural, electrical and thermo-mechanical properties. In order to achieve the technological demands of the thin film industry, measurement of their properties is very essential. In the present work, the fabricated thin film multilayers have been examined for microstructural and electrical properties. The films were characterized using SEM (Scanning Electron Microscope), XRD (X-Ray Diffraction), XRR (X-Ray Reflectivity), AFM (Atomic Force Microscopy), van der Pauw, curvature stress and TEM (Transmission Electron Microscopy). These characterization tools and the experimental details are discussed here.

4.2.1 van der Pauw measurement

In semiconductor industry, one of the widely used method to evaluate the resistivity of uniform sample such as thin films is the four point probe measurement technique (also known as van der Pauw (vdP) method) [72]. Using the vdP technique, it is possible to determine both the volume resistivity (ρ) and sheet resistance of a homogeneous and isotropic material (layers) having uniform thickness. vdP uses a 4-terminal sensing method having a point-like ohmic contact along the circumference of the layer. As per the fundamental requirements of the vdP technique, the samples must be free of voids and cracks which could lead to unwanted discontinuities in the value of resistivity.

The measurement of resistivity using vdP technique is based on the principle of determining the voltage response across the ohmic contact points when a constant electric current is applied through the sample. Considering a connection according to Figure 4.3 (a), a suitable magnitude of electric current is applied to two probes (e.g. 1 & 2) and the voltage response is measured across the other two probes (4 & 3) with a high impedance voltmeter. Based on the voltage reading, sheet resistance, R_a & R_b is calculated. In this case, the following equation given by van der Pauw holds

$$\exp\left(-\pi.\frac{R_a.h}{\rho}\right) + exp\left(-\pi.\frac{R_b.h}{\rho}\right) = 1 \qquad 4.1$$

where ρ is the specific resistivity and $R_a = U_{43}/I_{12}$ and $R_b = U_{14}/I_{23}$ are the resistance derived from the potential drop between the circumferential contact points 3 & 4 and 1& 4 respectively and h is the thickness of the sample.

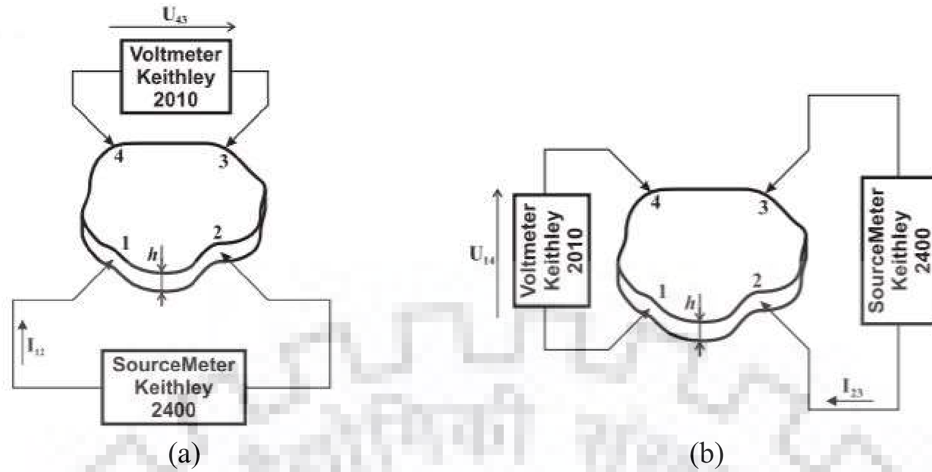

Figure 4.3: Measurement of specific resistivity of flat sample using van der Pauw technique [73].

For the measurement of resistivity of Mo/La_2O_3 thin films using a four-point probe method, square deposited samples of dimension 10 × 10 mm have been utilized. The ohmic contact points must be close to the corner/edge of the sample. The applied current during the measurement was kept at 5mA. The final value of the resistivity for a particular sample was averaged over 6 good readings using wafer prober model 1034XA6 as shown in Figure 4.4.

Figure 4.4: Wafer probe device for van der Pauw measurements.

4.2.2 Residual stress measurement

In 1909, Stoney [65] formulated the equation for determining the average biaxial stresses, σ_f in a thin film deposited over a rigid and thick substrate. The stress in the film value can be obtained from the difference in the bending (curvature) of the substrate before and after the film deposition using the following equation:

$$\sigma_f = -\frac{E_s h_s^2}{6(1-\nu_s)h_f}\left(\frac{1}{R_f} - \frac{1}{R_o}\right) \quad 4.2$$

where, R_o is the radius of the substrate material before deposition and R_f is the measured radius of curvature after deposition. Multiple films deposited over the same substrate contributes independently to the total substrate curvature which is given by:

$$\sigma_{f1}h_{f1} + \sigma_{f2}h_{f2} + \cdots \sigma_{fx}h_{fx} = -\frac{E_s h_s^2}{6(1-\nu_s)}\left(\frac{1}{R} - \frac{1}{R_o}\right) \quad 4.3$$

where, the subscript x denotes the number of films deposited over the substrate. Stoney's relation is the foundation of the curvature method, that helps in the estimation of average stress generated in the thin film. A schematic of the wafer curvature system is shown in Figure 4.5. During the stress measurement, a laser beam is scanned and reflected from the wafer's surface using a lens and a rotating mirror system. A position sensitive photodiode (PSD) continuously monitors the reflected beams and measures their deflection. For a perfectly flat wafer, all the reflected laser beams meet at a single point. There is no change in the position of the reflected beam across the wafer having a constant curvature. Figure 4.6 shows the schematic of wafer curvature system.

In the present work, a laser-optical Flexus FLX-2410 system with two laser sources of wavelength 670 nm and 750 nm has been used to compare the curvature of the sample in order to determine film stress after deposition. For the stress measurements, rectangular samples of 250 µm thick Si wafers and dimension 59 × 7 mm has been used. The laser beam moves 54 mm in length across the film surface. The surface of the wafer was kept free from strains and other contaminants, which may scatter the laser and disturb the measurement. The readings were averaged over three measurement scans both in as-depositedcondition and heat-treated state.

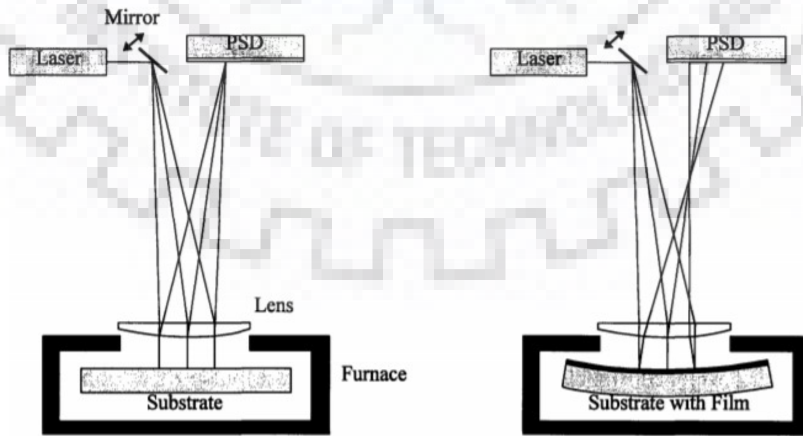

Figure 4.5: A schematic of a laser-scanning wafer curvature measurement system [74].

Figure 4.6: Curvature stress measurement device.

4.2.3 In-plane microstructure: Scanning electron microscope (SEM)

SEM is one of the most widely used characterization method for high resolution imaging and microanalysis for solid surfaces. So, study of microstructure using SEM is very much essential in order to understand the macro properties of the materials. SEM produces images of a sample by scanning the surface using a beam of high energy electrons. The high energy electrons after interacting with the sample produce characteristics X-rays, secondary electrons and back scattered electrons as a result of elastic and inelastic collision and scattering giving information about phase structure and orientation of the sample, surface morphology and texture, and chemical composition etc. SEM can capture images of the sample with dimensions ranging from several microns to few nanometres. A schematic view of the principle operation mode of a SEM is shown in Figure 4.7.

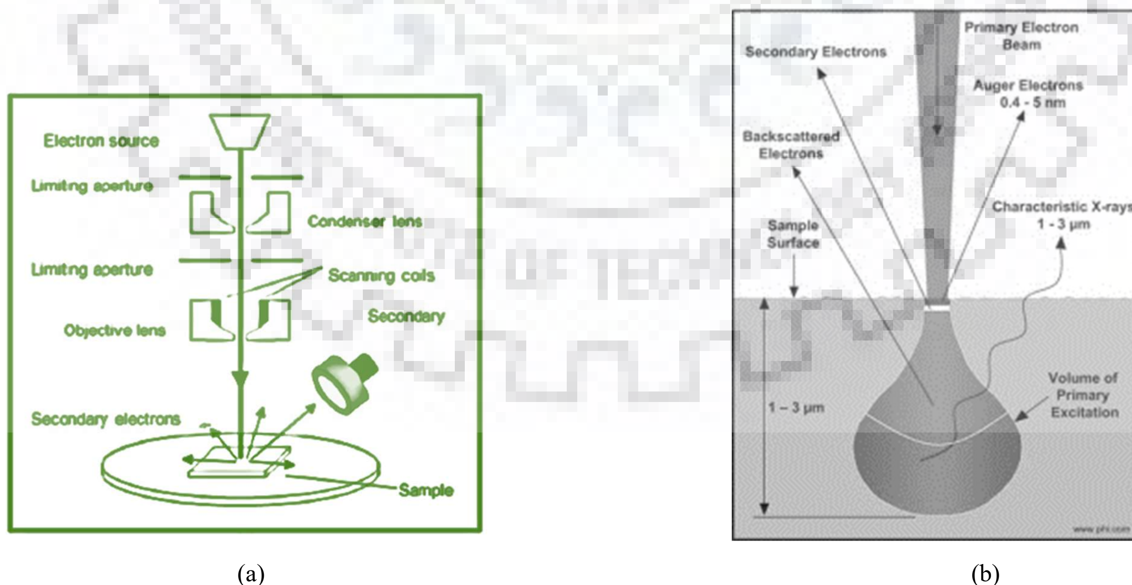

Figure 4.7: Schematic diagram of (a) scanning electron microscope (SEM), (b) Schematic showing interaction volume of the electrons/interaction depth.

Microstructural examination of Mo/La_2O_3 multilayer thin films have been carried out using Zeiss Ultra 55 Plus coupled with in-lens detector at a working distance 4-5 mm. The instrument was operated at 5kV, and the secondary electrons were collected using an in-lens detector placed rotationally symmetric inside the electron column of the microscope shown in Figure 4.8. Magnification from 500X to 150kX was taken for all the samples.

Figure 4.8: SEM Zeiss Ultra Plus used for viewing the top surface microstructure of the samples.

4.2.4 Atomic force microscopy (AFM)

One of the fast and powerful technique in material science to know the morphological features of nanometre range without the need of vacuum is the atomic force microscopy. In the current work, the surface morphology of the Mo/La_2O_3 thin films has been examined using this technique which is dependent on the Van der Waals forces between the tip and the sample surface. Data such as surface roughness can be obtained if these forces are known. AFM gives a 3D profile of the sample's surface with nanometre scale resolution by calculating the forces between the surface and the probe (<10 nm) at a very small distance (0.2-10 nm). The probe is supported on a flexible piezoelectric cantilever. The AFM tip softly touches the sample's surface and records the force between the surface and the probe.

For the investigation of the Mo/La_2O_3 thin films, tapping mode of operation was chosen. The AFM images were taken using a dimension Icon AFM (Bruker) as shown in Figure 4.9. The probe made of silicon and coating of aluminium has been used (Model: AC160TS-R3, Olympus). The maximum operating frequency of the probe having a tip radius of curvature of 10 nm has been utilized for scanning the surface. The scan size and rate were chosen as 2 x 2 µm and 1 Hz respectively. The surface topography data has been analysed using the Gwyddion software [75].

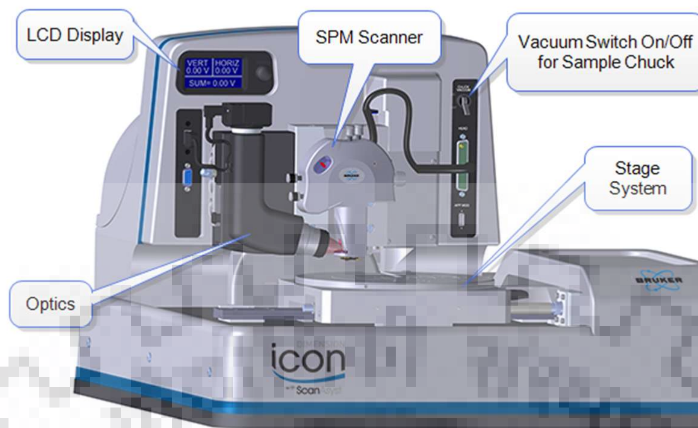

Figure 4.9: Schematic of a Bruker Dimension Icon AFM [76].

4.2.5 Out-plane microstructure: Focused ion beam (FIB)

FIB has a similar instrumental setup like SEM which includes a vacuum system chamber, sample stage, detectors, an ion column, gas input system and a liquid metal ion source. FIB technique can be utilized primarily to prepare the cross section of material or a thin film. There is a possibility to do a ion milling with the help of liquid metal ion source (LIMS) ejecting ions of size 5nm in diameter. A tungsten needle attached to LIMS is used to hold the metal source material. The most widely used material for LIMS is gallium because of low volatility, low melting point (~30 °C), and low vapor pressure [77]. The striking of Ga^+ ions onto the sample surface removes the material by sputtering process. Using the similar polishing approach as used in metallography, the samples polishing of the cross-section can be done.

To obtain the cross-sectional image of the Mo/La_2O_3 thin films, a FIB Crossbeam 1540 XB, Zeiss instrument was used. Films with substrate were sliced for observing the cross section of the multilayer stack. To have a clear view of the film cross section, three steps needs to be followed: (a) deposition of a protective layer of carbon and platinum on the top of the film; (b) milling a large trapezoidal section using current of 100nA; (c) polishing of the trapezoidal section with a current of 50pA. After polishing the sample, the sample was viewed under the SEM at a magnification of 80kX. The film thickness was obtained through the FIB cross sectional images. Figure 4.10 shows the FIB system used for characterizing the out-plane microstructure.

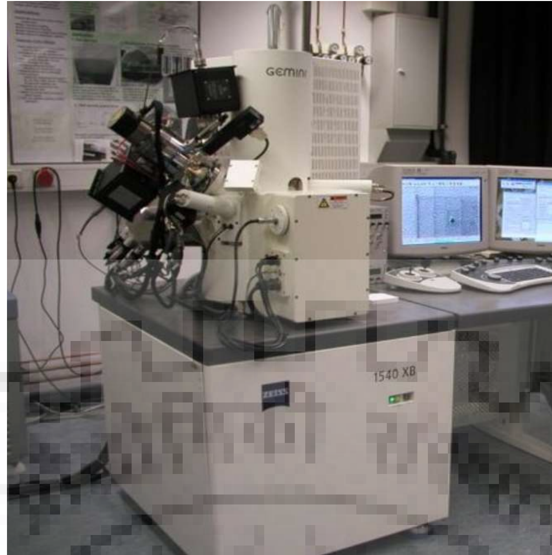

Figure 4.10: FIB Crossbeam 1540 XB, Zeiss.

4.2.6 X-Ray diffraction (XRD)

X-ray diffraction studies were done using Co K_{α} radiation employing a Panalytical X'Pert θ-θ thin-film diffractometer (see Figure 4.11) operating in Bragg-Brentano geometry. The diffractometer was operated at 40kV and 40mA for microstructural investigations. Using the famous Bragg's equation, the d-spacing of the atomic layers can be estimated from diffraction peak positions. With the help of d-spacing, phase analysis can be carried out. Furthermore, using single line broadening analysis (see for details Ref. [78] and references therein) , important microstructural parameters such as volume weighted crystallite size, D, associated microstrain (due to defects and vacancies), ε, and peak shift (existence of macro stress).

Mathematically, the measured diffraction profile, *h(x)* can be considered as a convolution of structurally broadened profile, *f(x)* and instrumental profile, *g(x)*. The instrumental broadening comes from the intrinsic instrumental deviations whereas structural broadening is a result of crystal imperfections which includes presence of microstrain due to misfits, precipitates, dislocations and the small crystallite size. Both these broadenings can be approximated using a pseudo-Voigt function, which is a convolution of a Cauchy (c) and a Gaussian (g) profile. On applying Voigt-method [79], [80] the integral breadth (β) of both the peak component i.e. Cauchy and Gaussian profile of the structurally broadened profile can be obtained from the β and Voigt-parameter (ratio of full width half maximum to β) of the measured profile. For finding the instrumental broadening of the diffractometer as a function of diffraction angle 2θ, 15 hkl reflections of a LaB_6 (NIST SRM660a) standard powder

sample was used. Integral breadth and Voigt parameters at 2θ angles of Mo and La_2O_3 were calculated by interpolation. Assuming the Gaussian component resulting from the microstrain, ε, and the Cauchy component arising from the finite crystallite size, D_v:

$$\beta_{f,c} = \left(\frac{\lambda_d}{D_v \cos\theta}\right) \quad 4.4$$

$$\beta_{f,c} = 4\varepsilon\theta \tan\theta \quad 4.5$$

where, θ is the maxima diffraction line position and λ_d is the wavelength. The obtained reflection from the films was fitted with the pseudo-Voigt function with a linear background using a profile fitting analysis in X'Pert Highscore Plus v3.0 to find the peak parameters which include, Voigt parameter, integral breadth, FWHM, universal shape, peak position.

The scan range considered for the XRD measurement of Mo/La_2O_3 thin films has been chosen as 25-76° and 87-150° with a step size of 0.01° to avoid the high intensity Si (200) peak arising from the substrate at 82.43°. Peak shifts related to error in sample height positioning was corrected using the single crystal Si diffraction peak.

Figure 4.11: Panalytical X'Pert XRD device.

4.2.7 X-Ray reflectivity (XRR)

XRR is one of the most widely used, simple and powerful non-destructive technique to examine the thin film structure. Using this method, thin film individual layer parameters such as surface/interface roughness, layer thickness from several to a few hundred nm and density can be quantitively estimated.

The analysis is based on the X-ray reflection intensity curves obtained from low angle/grazing incident X-rays. The XRR measurement can be used to investigate amorphous, single crystalline and polycrystalline materials.

The index of refraction, n_r is typically less than one for X-rays which indicates that the total external reflection happens at lower angles. There is a specific angle called the critical angle, α_c at which the total external reflection stops when the X-rays falls on a flat sample. When the incident angle goes beyond the critical angle, the X-rays penetrates into the sample. This angle can be directly related to the density of the reflecting medium. The intensity of the reflectivity curve drops exponentially as the incident angle, α_i becomes more than the α_c. The typical X-ray reflectivity curve contains many oscillations known as Kiessig fringes [81] which is the result of interference of the X-rays from the surfaces and interfaces of the individual layer.

(a) Density of the film: The mass density is associated with the value of refractive index, n_r which varies with the critical angle. The density value is directly proportional to the critical angle. Using small angle approximations, the critical angle can be expressed as:

$$\alpha_c = \sqrt{2\delta} = \sqrt{\frac{\rho_e r_e}{\pi}}\lambda_d \qquad 4.6$$

where, $\delta = \left[\frac{\rho_e r_e \lambda^2}{2\pi}\right]$, ρ_e is the electron density, λ is the wavelength of X-ray, and r_e is the electron radius.

(b) Thickness of the film: The periodic oscillations in the intensity curve gives the information about the individual layer thicknesses, t. Thickness can be calculated by finding the Fourier transform of the oscillation curve. For the maxima intensity, the path difference between the reflected waves should be integral multiple of the wavelength which is given by:

$$2t\sqrt{sin^2\alpha_i - sin^2\alpha_c} = m\lambda \qquad 4.7$$

In most cases, the incident angle, α_i is small, therefore the above equation can be rewritten as:

$$\alpha_i^2 - \alpha_c^2 = m^2\left(\frac{\lambda}{2t}\right)^2 \qquad 4.8$$

where, m is the order of reflection.

(c) Roughness of the film: XRR measurements can be used to determine the surface and interface roughness. Roughness causes the diffused reflection of the incident beam leading to decrease in the specular intensity of the curve as well as the dampening of Kiessig fringes (oscillations). Surface roughness results in the faster decay of X-ray reflectivity curve whereas interface roughness can be

obtained from the amplitude of Kiessig fringes. Rapid dampening of these oscillations is indicative of the large interface roughness.

Figure 4.12 show the possible information which can obtained from the reflectivity curve.

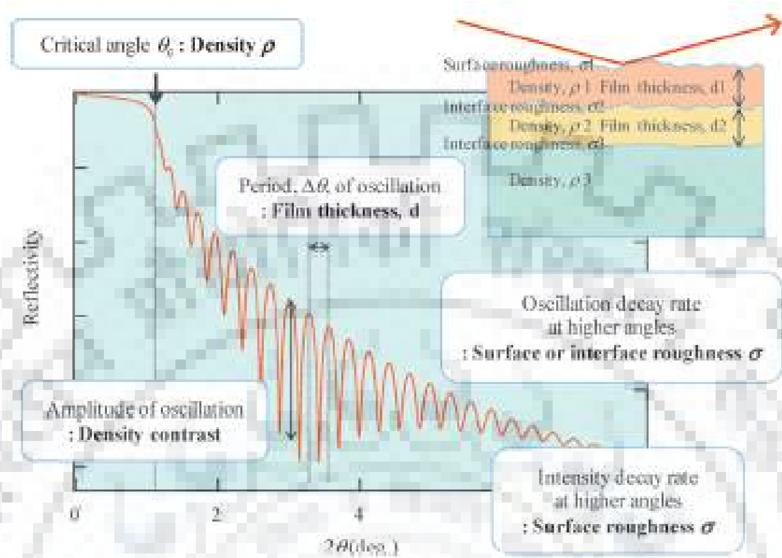

Figure 4.12: Information provided by X-ray reflectivity curve [82].

The reflectivity measurements were carried out using a Panalytical X'Pert MRD thin film with a parallel beam geometry equipped with Eulerian cradle. The XRR device comprised of a Cu X-ray tube operated at 40kV and 40mA and a parallel plate collimator in the diffracted beam. The diffraction measurements were carried out at low-angle region (1-6°). The fitting of the reflectivity profile was done using the X'Pert Reflectivity v1.1 program.

4.2.8 Transmission electron microscopy (TEM)

TEM is a powerful technique to view the sample parallel to the interface with an excellent lateral resolution. Electron gun, image producing and recording system are the essential components of a TEM. Beside the conventional transmission electron microscopy (CTEM), TEM can also appear in other forms such as scanning transmission electron microscope (STEM) and high-resolution transmission electron microscope (HRTEM). Unlike CTEM, STEM contains only a gun, an electron spectrometer & detection system and a probe forming lens. TEM generally requires a very thin sample which can ensure the transmission of electrons and interaction with atoms either elastically or inelastically. Hence, sample preparation techniques such as electropolishing is very much essential

and based on diffraction contrast different images modes like bright-field and dark-field of TEM can be achieved.

TEM investigations of the Mo/La_2O_3 multilayer films were made on Tecnai F30 (FEI) (see Figure 4.13) equipped with a high angle angular dark field detector in the STEM mode. The thin film lamella was prepared using the FIB technique which involved the deposition of protective Pt line on the surface by electron and ion beam deposition method followed by Ga^+ ions for ion milling to achieve electron transparency.

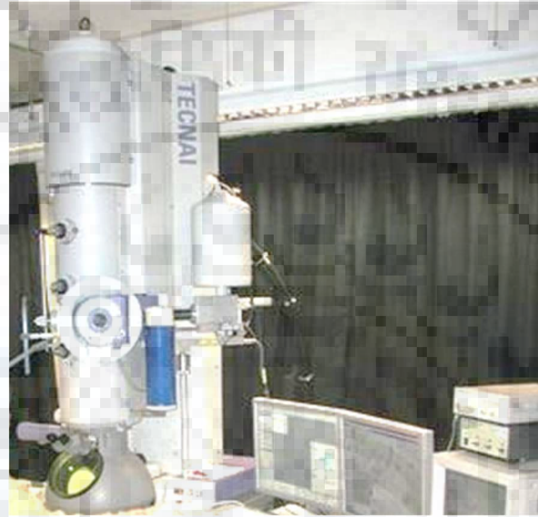

Figure 4.13: TEM Tecnai F30 FEI device.

5. Results and Discussion

5.1 Electrical Resistivity

The major challenge for the Mo/La_2O_3 thin film metallization system, in order to be considered as the potential IDT material for SAW based high temperature sensor, is to achieve the resistivity value of these polycrystalline film close to that of the bulk while maintaining the thermal stability in harsh environment conditions. Resistivity of the individual thin film layers i.e. Mo & La_2O_3 is approximately 18 μΩ.cm and 10^9 μΩ.cm where the resistivity value of Mo is more than twice of the reported values in the bulk form [83]. Using the van der Pauw method, the resistivity values of the pure Mo and Mo/La_2O_3 thin film multilayers in as-deposited and annealed state were measured and are tabulated in Table 5.1. The error bar corresponds to the difference between the maximum and minimum resistivity values obtained for a specific film in AD and HT conditions.

Table 5.1: Measured resistivity values of thin films using van der Pauw technique.

Multilayer Samples	**Electrical Resistivity (μΩ.cm)**			
	As-Deposited	**Annealed (800°C for 24 h)**	**Annealed (800°C for 48 h)**	**Annealed (800°C for 120 h)**
Mo-Si	18.5 ± 0.3	8.6	8.6	8.2
Mo-(La_2O_3-Mo)-Si	19.5 ± 0.5	17	15.9 ± 0.3	11.1 ± 1.9
Mo-(La_2O_3-Mo)$_2$-Si	21 ± 0.5	21.2 ± 1.4	19	11.6 ± 0.1
Mo-(La_2O_3-Mo)$_4$-Si	21.3 ± 0.5	23.7 ± 0.6	21 ± 0.3	13.9 ± 0.1
Mo-(La_2O_3-Mo)$_8$-Si	24.3 ± 0.9	25.9 ± 2.2	23.3 ± 1.2	15.3 ± 1.2

To better visualize the trends in the measured resistivity values, the variation of the resistivity as a function of bilayer period and individual La_2O_3 film thickness has been plotted as shown in Figure 5.1.

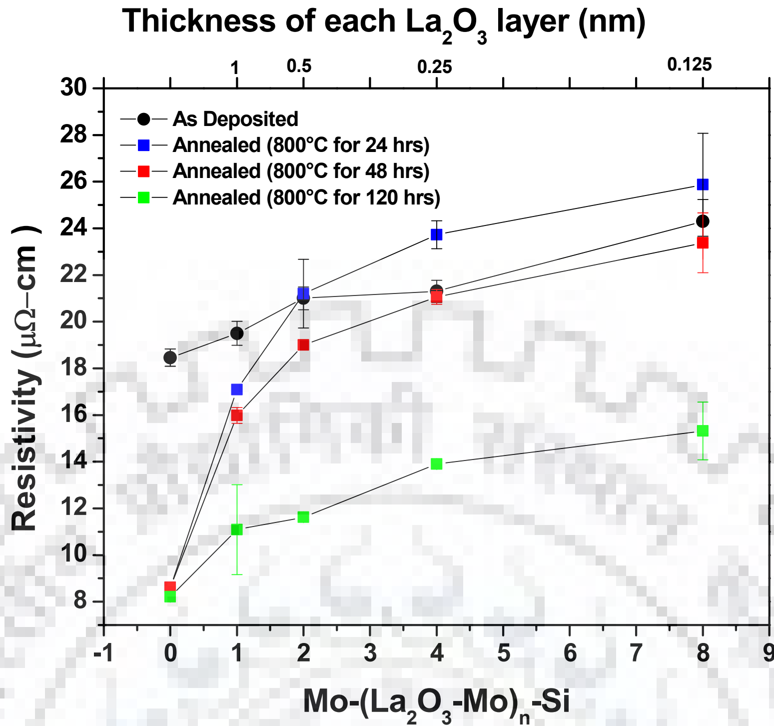

Figure 5.1: Resistivity variation as a function of bilayer period.

Pure Mo film of thickness 100 nm exhibited a resistivity of 18.4 μΩ.cm in as-deposited condition. However, after annealing, there was decrease in the resistivity values which can be attributed to grain growth (see section 5.2). The resistivity value reaches to a minimum of 8.2 μΩ.cm after 120 h of annealing as the average in -plane and out plane grain size increases continually. Conductivity of the film is found to decrease after the addition of lanthanum oxide layer. Resistivity of the film is also affected by the electron scattering at film surfaces/interfaces, grain boundaries, defects in addition to the presence of impurities [69]. In the present case, the resistivity thus increases with the increase in the number of bilayer periods. Electron mean free path (EMFP) also strongly affects the resistivity values. It is known that the EMFP of pure solid Mo at room temperature is close to 40 nm [84]. As the thickness of the individual Mo layer goes below the EMFP, there is rapid increase in the resistivity. Upon annealing for 24 h, the resistivity of Mo film reduces drastically and reduces only marginally thereafter upon subsequent annealing upto 120 h. In comparison, for the 1 bilayer period Mo/La_2O_3 film, the reduction in the resistivity is lower after 24 h of annealing. For the 2-bilayer period film, hardly any reduction in the resistivity is observed for the same annealing duration. Furthermore, in contrast annealing the 4 and 8 bilayer period films led to an unexpected increase in the resistivity. However, after 48 and 120 h of annealing, the resistivity decreases for all the films. It is interesting to note that the resistivity value of the 8-bilayer period multilayer film after 120 h of vacuum annealing

is lower than that of the pure Mo film in as-deposited state indicating the increased thermal stability and conductivity of the film.

Overall, the combination of Mo and La_2O_3 does not drastically affect the electrical property of the multilayer thin films. In addition to EMFP, factors such as surface morphology, density, grain structure and film stacking configurations also affects the electrical conductivity of thin films. So, examination of these parameters is very important in order to explain the resistivity behaviour.

5.2 In-plane microstructure: SEM

Suitable pattering and sandwiching of multiple films are the basic requirements in the fabrication of IDT materials for SAW based high temperature sensors. Film structure is also affected by the deposition properties and adhesion between each film layer. Therefore, investigation on the genesis of surface microstructure of multilayer Mo/La_2O_3 thin films is substantial to throw light on the electrical behaviour of these films in as-deposited and vacuum annealed condition.

The in-plane (top film surface) morphology has been viewed using SEM in as-deposited and annealed condition. As seen by SEM, films obtained are polycrystalline in nature and are free of any cracks or voids. The pure Mo film show a typical elongated rice grain-like morphology. The as-deposited morphology is very similar to that of Mo for every multilayer thin film configuration. The reason for the Mo like morphology even after adding La_2O_3 layer could be attributed to the template-like effect of the underlying Mo film. Figure 5.2 displays the film morphology with different bilayers and annealing conditions.

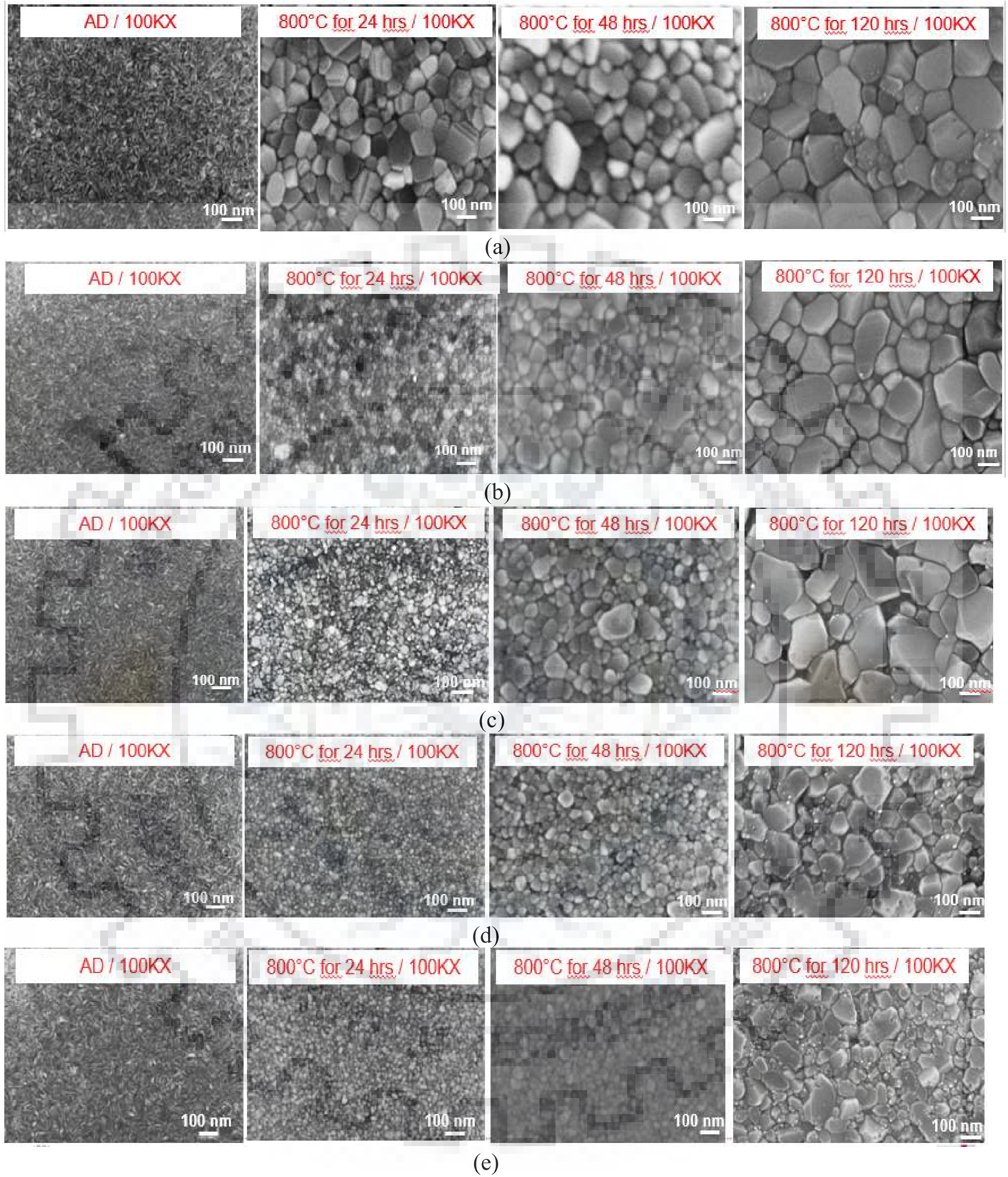

Figure 5.2: SEM micrographs of as-deposited(AD) and annealed, (a) Mo-Si, (b) Mo-(La_2O_3-Mo)-Si, (c) Mo-(La_2O_3-Mo)$_2$-Si, (d) Mo-(La_2O_3-Mo)$_4$-Si, (e) Mo-(La_2O_3-Mo)$_8$-Si, thin films.

In case of pure Mo film (Figure 5.2 (a)), there is progressively significant grain size increment upon vacuum annealing up to 120 h. With the addition of lanthanum oxide layers, the grain size increment decreases as compared to the pure Mo film which may be due to the pinning effect of lanthanum oxide particles. From Figure 5.2, it can be inferred that the grain growth upon annealing multilayer films is suppressed significantly when the number of bilayer period is increased. In order to qualify as a potential IDT material from microstructure point of view, the film needs to have smaller grain size with low roughness. To get smaller and uniform grains throughout the film, the dispersion of oxide particles needs to be uniform through the film. So, in the present investigation the film configuration consisting of 8 bilayers is more of interest. Upon annealing, it was found that Mo-(La_2O_3-Mo)$_8$-Si show a very uniform grain structure as seen in Figure 5.2 (e)). The average in-plane grain size of Mo-(La_2O_3-Mo)$_8$-Si is smallest of all the multilayer films after annealing.

Grain boundaries play a critical role in defining the electrical conductivity of the film as per the MS model. The effect becomes appreciable only when the size of the grain approaches the EMFP of the material. As the EMFP of Mo is close to 39 nm, the grain size is much larger than this. Therefore, electron scattering through grain boundaries is not the dominant mechanism for the electrical conductivity of Mo-(La_2O_3-Mo)$_8$-Si thin film. The increase in the resistivity mainly arise from the increase in the interface regions which causes electron scattering.

5.3 Surface roughness

In addition to grain boundary scattering, another factor which contributes to the resistivity size effect is surface scattering when the film thickness is close to EMFP of the material. Roughness of the material leads to diffuse scattering of electrons causing higher resistivity values. This effect is more pronounced in a thinner film as reported by Rossnagel et al. [85]. Thus, higher is the roughness, more is the electrical resistance. Ideal IDT material for the SAW based temperature sensors calls for a low surface roughness film. Hence, it is very important the Mo/La_2O_3 multilayer films show low roughness value. The average roughness value (rms) was measured for all the films scanned over the area of 2 × 2 μm obtained from the AFM images is listed in Table 5.2. The error bar corresponds to the standard deviation of the respective films.

Table 5.2: Measured RMS Surface Roughness (Rq)

Multilayer Samples	Average surface roughness-RMS (nm)			
	As-Deposited	Annealed (800°C for 24 h)	Annealed (800°C for 48 h)	Annealed (800°C for 120 h)
Mo-Si	0.6	3.1 ± 0.4	3.9 ± 0.5	4.7 ± 0.6
Mo-(La_2O_3-Mo)-Si	0.5	0.8 ± 0.2	3.9 ± 0.4	7.2 ± 0.9
Mo-(La_2O_3-Mo)$_2$-Si	0.5	0.7	2.3 ± 0.8	6.7 ± 1.1
Mo-(La_2O_3-Mo)$_4$-Si	0.5	1 ± 0.3	2.4 ± 0.4	8.1 ± 1.7
Mo-(La_2O_3-Mo)$_8$-Si	0.5	0.7	2.4 ± 0.5	5.6 ± 0.9

The roughness value was found to be less than 1 nm for the as-deposited films while it increases with the increase in the annealing duration. There is no clear dependence of roughness on the number of bilayer periods present in the multilayer Mo/La_2O_3 films with all films exhibiting sub-nanometer roughness.

Out of all the annealed films, Mo-(La_2O_3-Mo)$_8$-Si shows the lowest surface roughness after being treated for 120 h even though it has the maximum number of bilayer periods. The AFM microstructure of the films and the roughness variation as a function of bilayer period and annealing duration are shown in Figure 5.3.

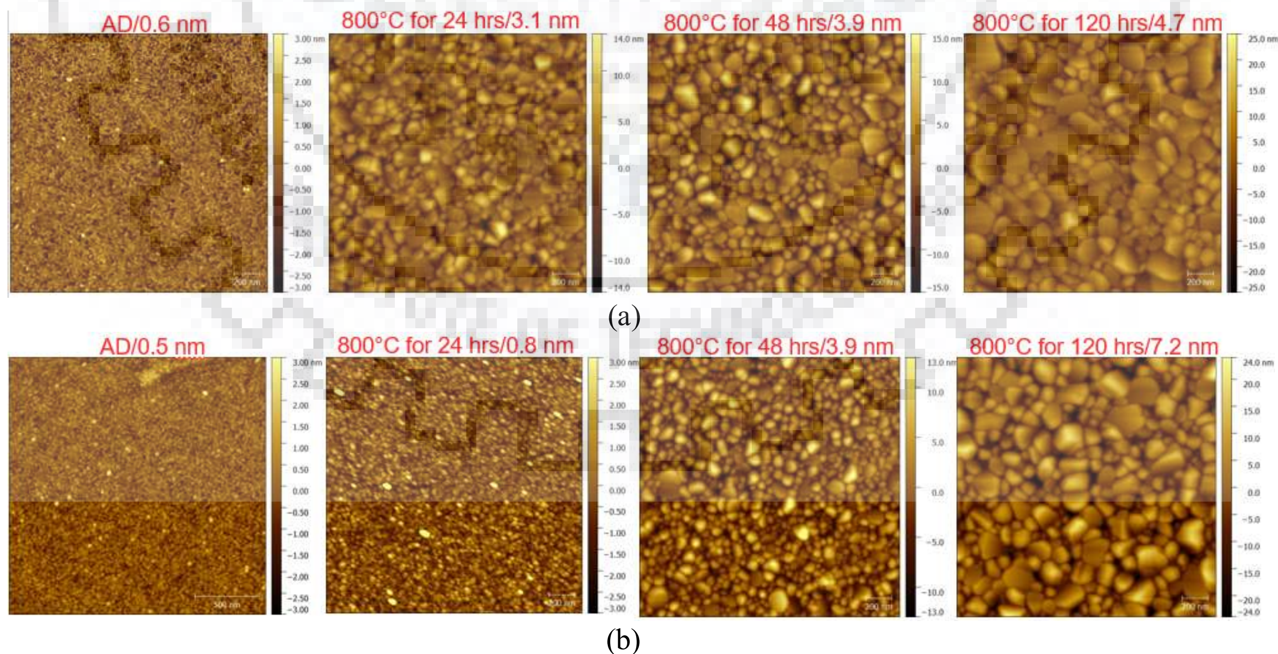

AD/0.5 nm
800°C for 24 hrs/0.7 nm
800°C for 48 hrs/2.3 nm
800°C for 120 hrs/6.7 nm

(c)

AD/0.5 nm
800°C for 24 hrs/1 nm
800°C for 48 hrs/2.4 nm
800°C for 120 hrs/8.1 nm

(d)

AD/0.5 nm
800°C for 24 hrs/0.7 nm
800°C for 48 hrs/2.4 nm
800°C for 120 hrs/5.6 nm

(e)

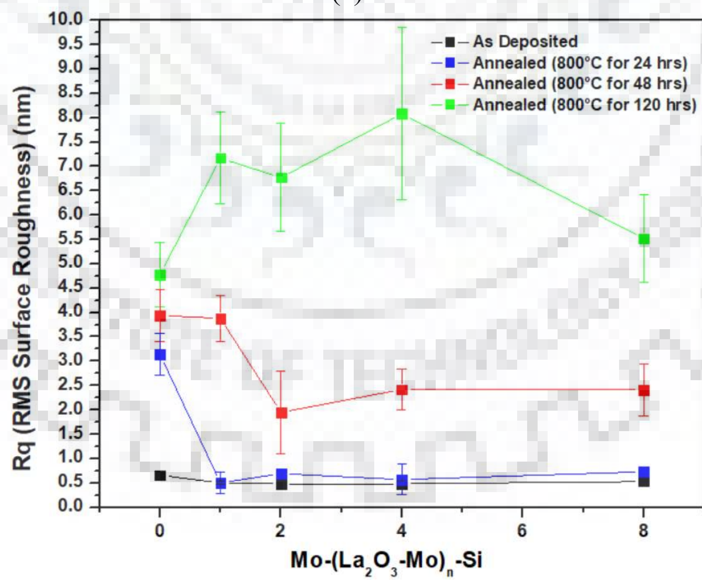

(f)

Figure 5.3: AFM topographical images of as-deposited and annealed, (a) Mo-Si, (b) Mo-(La_2O_3-Mo) Si, (c) Mo-(La_2O_3-Mo)$_2$-Si, (d) Mo-(La_2O_3-Mo)$_4$-Si, (e) Mo-(La_2O_3-Mo)$_8$-Si, multilayer thin films and (f) RMS roughness variation as a function of bilayer period and annealing duration.

From Figure 5.3, it is evident that AFM images are very much consistent with the SEM micrographs. There are some grains which are darker than other which indicates that they are deeper than others. After the annealing of the films, it can be seen from the roughness scale that the height difference between the deepest and the highest grain increases from 3 nm to approximately 30 nm indicating a drastic roughness of the films. It should be noted here that this height difference is the lowest for the Mo-(La_2O_3-Mo)$_8$-Si film. Besides this, it can be seen that the grain size is also smallest in case of Mo-(La_2O_3-Mo)$_8$-Si after 120 h of annealing.

From the above AFM images, it can be observed that, upon annealing for 24 h there is a 5-fold increase in the RMS roughness value in case pure Mo film from the as-deposited state whereas there is only a marginal increase observed for multilayer thin films. Though the high surface roughness of the multilayer film and presence of highly resistive second phase particles are expected to reduce the conductivity of the films due to diffuse scattering, the annealing of the films curtails the effect as seen in Figure 5.1.

5.4 Out-of-plane microstructure: FIB

Figure 5.4 shows the cross-sectional micrograph of the pure Mo and Mo/La_2O_3 multilayer thin films. The interface between the Mo and La_2O_3 layers can be clearly seen for the 1 bilayer film configuration (Figure 20(b)), however it is not identifiable in other configurations. Since the individual layer thickness of La_2O_3 decreases with the increase in the multilayer stacks to maintain same composition, the interface cannot be seen distinctly. The thickness of the film from cross-section images are in good agreement with the intended values.

From the FIB images, it can be observed that the top layer roughness increases after annealing which was also seen from AFM images. Out of all the film configurations annealed for 120 h, Mo-(La_2O_3-Mo)$_8$-Si has minimal modulations on the top surface which is indicative of a more stable film.

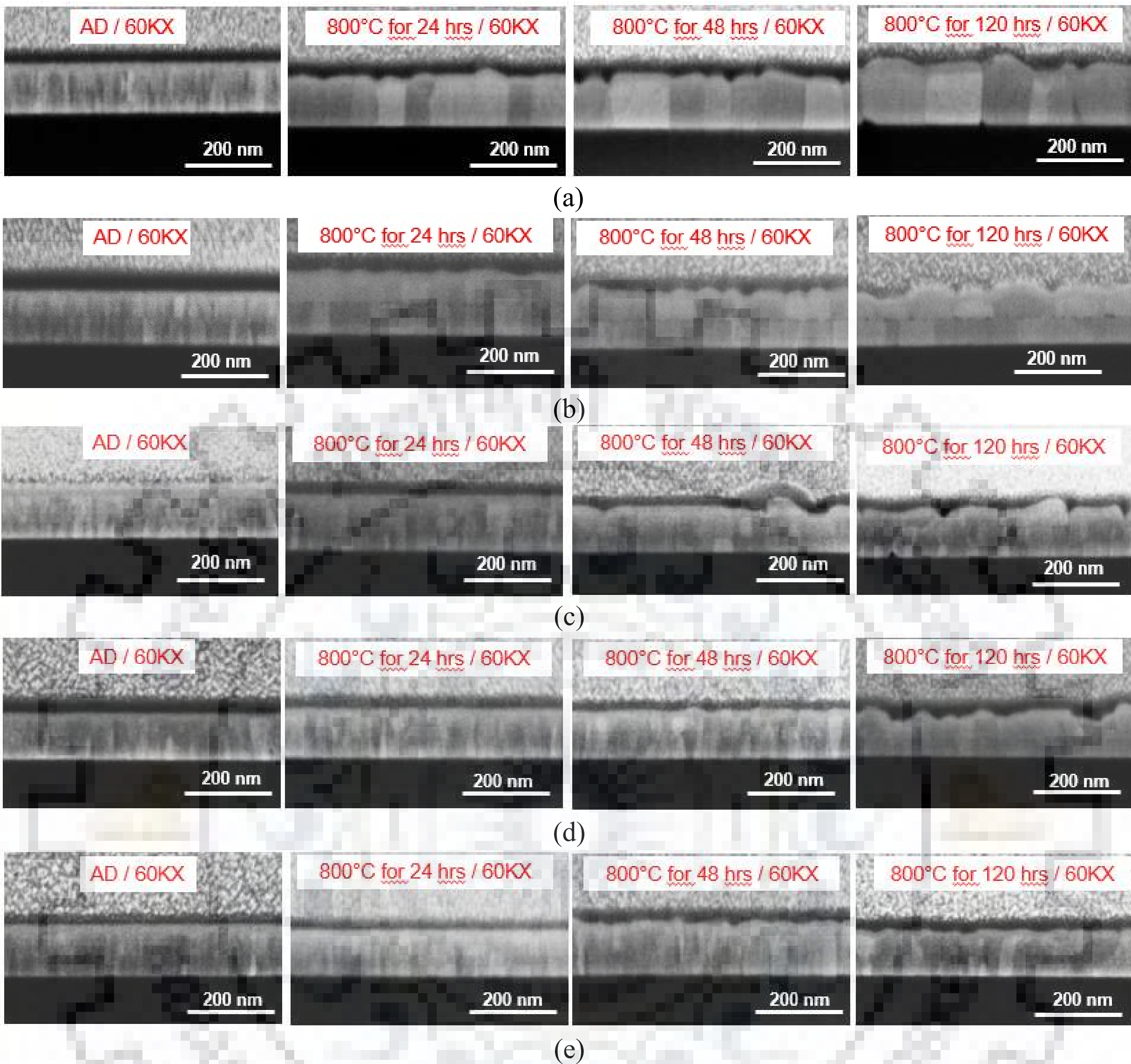

Figure 5.4: FIB cross-section view of as-deposited and annealed, (a) Mo-Si, (b) Mo-(La_2O_3-Mo)-Si, (c) Mo-(La_2O_3-Mo)$_2$-Si, (d) Mo-(La_2O_3-Mo)$_4$-Si, (e) Mo-(La_2O_3-Mo)$_8$-Si, thin films.

The above cross-section images show the presence of small and tapered grains in the as-deposited films. A closer look shows that in case of Mo, the grains are more or less continuous across the film thickness while for the multilayer films, smaller tapered grains are visible that are interrupted along the film thickness direction. As the Mo films are heated, large columnar grains are formed that span the entire film thickness. Upon annealing for 120 h, a more equiaxed grain structure develops. In contrast, for the Mo-(La_2O_3-Mo)-Si film, a clear interruption of grain growth is observed midway of the film thickness. This can be attributed to the presence of a continuous layer of a La_2O_3 that interrupt the growth in the out-of-plane direction. However, for the other multilayer films in both as-deposited and annealed condition, along with discontinuous grains, columnar grains of Mo extending through

the film at certain locations can be seen. This could be due to an open/discontinuous La_2O_3 layer due to low layer thickness. Thus, the out-of-plane grain growth is interrupted only at locations with La_2O_3.

The in-plane grain size also reduces with increasing number of bilayer periods which could be attributed to the presence of La_2O_3 at the top and bottom surface of the Mo grains, and with probability also at the adjacent grain boundaries, pinning the grains in two directions. Another reason for decreased in-plane grain size could be a result of a mixture of 2 types of grains that are interspersed: uninterrupted grains (columnar, spanning the film thickness) and grains that are pinned by La_2O_3 (interrupted across layers). The probability of this mixture of grains being more uniformly dispersed increases with increasing number of bilayer periods. This could also explain the more uniform in-plane grain size in the Mo-(La_2O_3-Mo)$_8$-Si film.

5.5 Film structure: XRR

Figure 5.5 shows the angle dependent reflectivity spectra of pure Mo and multilayer Mo/La_2O_3 thin films in as-deposited and annealed condition.

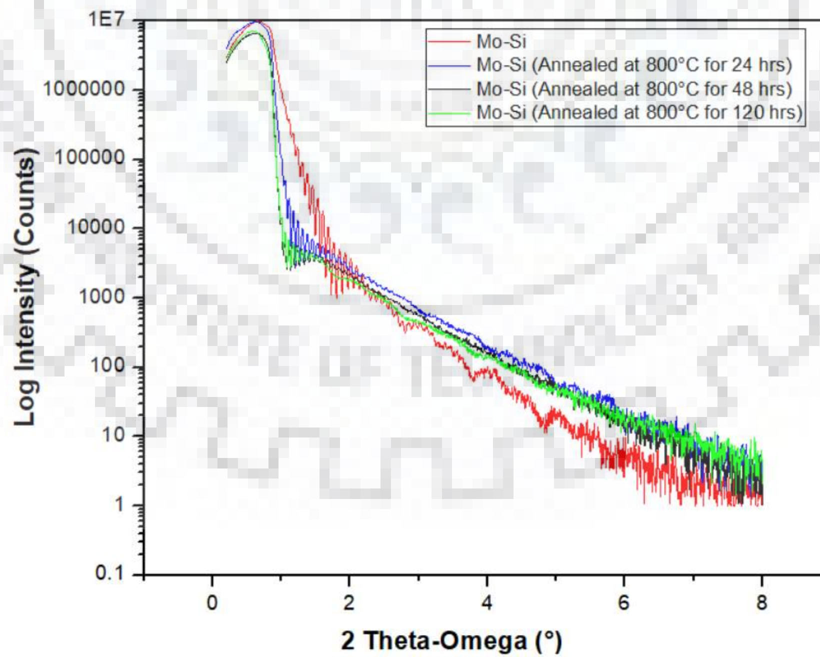

(a)

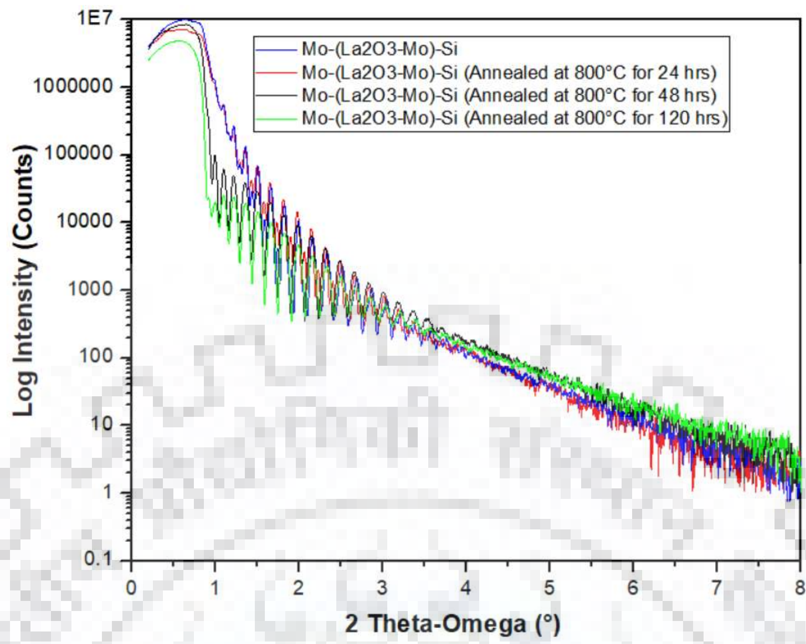

(b)

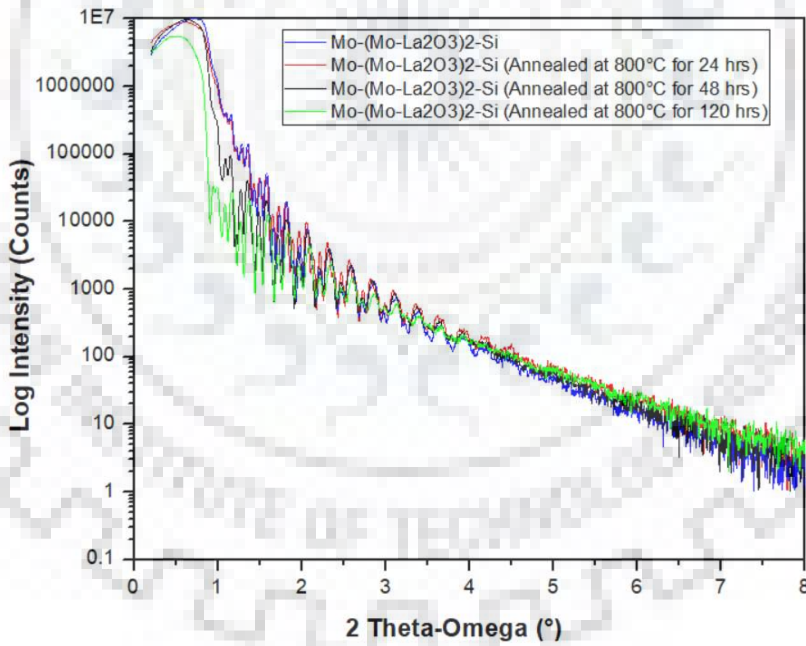

(c)

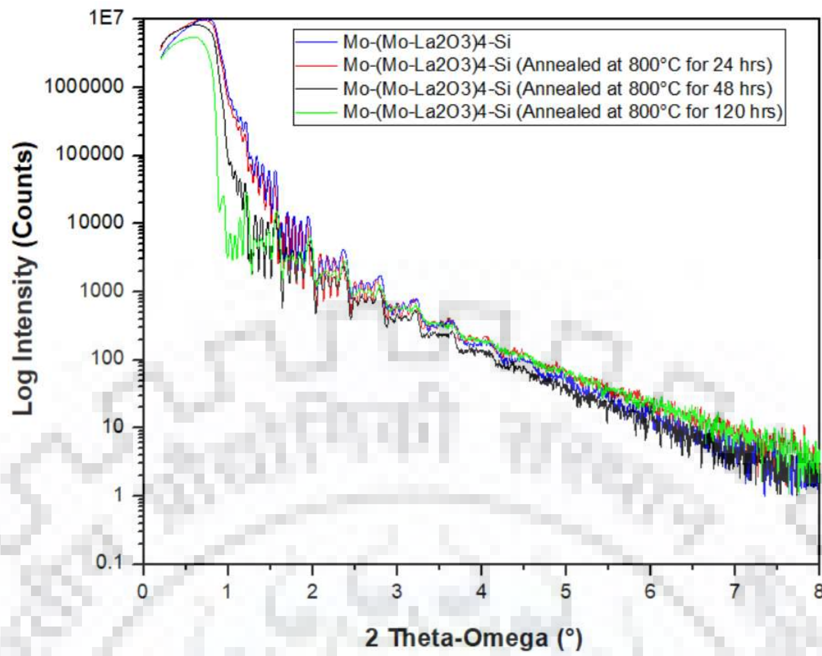

(d)

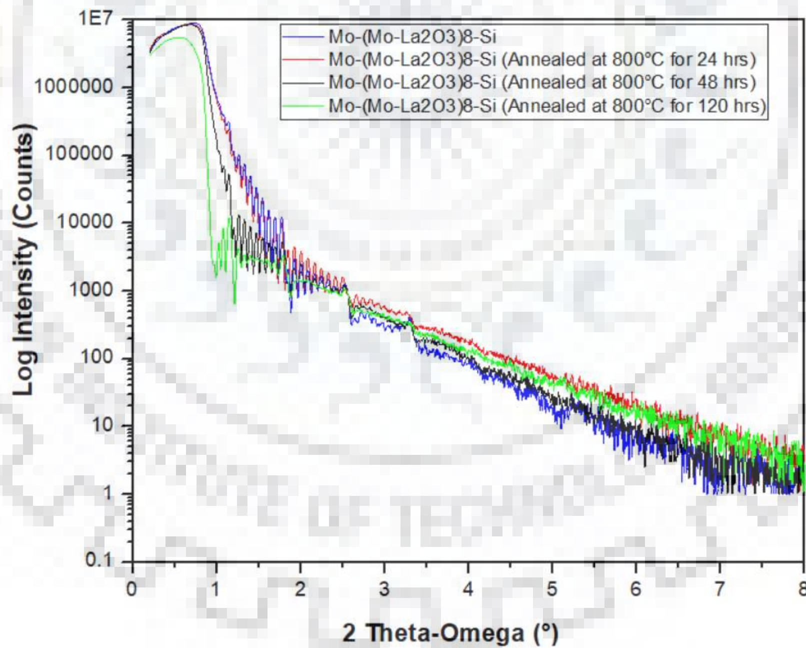

(e)

Figure 5.5: XRR curves for as-deposited and annealed, (a) Mo-Si, (b) Mo-(La_2O_3-Mo)-Si, (c) Mo-(La_2O_3-Mo)$_2$-Si, (d) Mo-(La_2O_3-Mo)$_4$-Si, (e) Mo-(La_2O_3-Mo)$_8$-Si, thin films.

It can be noted from the XRR curves that good quality films with low roughness have been deposited in this work as evidenced from the presence of Kiessig fringes up to high angles with low intensity modulation. Further on, it can be confirmed that all the layers in the multilayer films are indeed distinct and separated with a good periodic structure in the as-deposited state as evidenced by the presence of Bragg peaks. This is also true for the film Mo-(La_2O_3-Mo)$_8$-Si wherein Bragg peak upto 3rd order is seen suggesting high structural order. It is interesting to note that in all the films, distinct Bragg peaks are visible even after annealing for 120 h which further confirms that the Mo/La_2O_3 layers do not intermix and remain distinct. It is seen that both, the oscillation and intensity began to decay faster with the increase in annealing duration as well as the increase in the bilayer period which is caused by the film roughness as confirmed by SEM, AFM and FIB images. There is also a minimal change in the oscillation amplitude of the fringes with the change in the bilayer period signifying the density value of Mo layer close to that of the bulk.

In the present investigation, Mo-(La_2O_3-Mo)$_8$-Si thin film is more interesting among other film configurations because of its stable microstructure even after 120 h of annealing. So, the XRR curve fitting and simulations of Mo-(La_2O_3-Mo)$_8$-Si were performed to extract the values of structural and interface parameters.

The 17-layer model comprising of Mo & La_2O_3 layers in addition to interlayers of carbon just above the substrate and the contamination layer of MoC at the top of the film was used for the simulation. The model used for fitting the reflectivity spectra in as-deposited and annealed condition is shown in Figure 5.6. The presence of C layer above the substrate has been assumed to come from the substrate cleaning using ethanol and acetone. Since Mo has more affinity to form a carbide rather than the oxide, so the top layer of the film has been assumed to be MoC. For fitting, the 17-layer configuration has been modelled using superlattice structure of Mo and La_2O_3 layers repeating 8 times to reduce the fitting complexity and time. Instead of a pure La_2O_3 interlayer, a mixed Mo-La_2O_3 layer is considered for the fitting of the specular XRR data since the possibility of the existence of 0.125 nm of La_2O_3 layer is unrealistic.

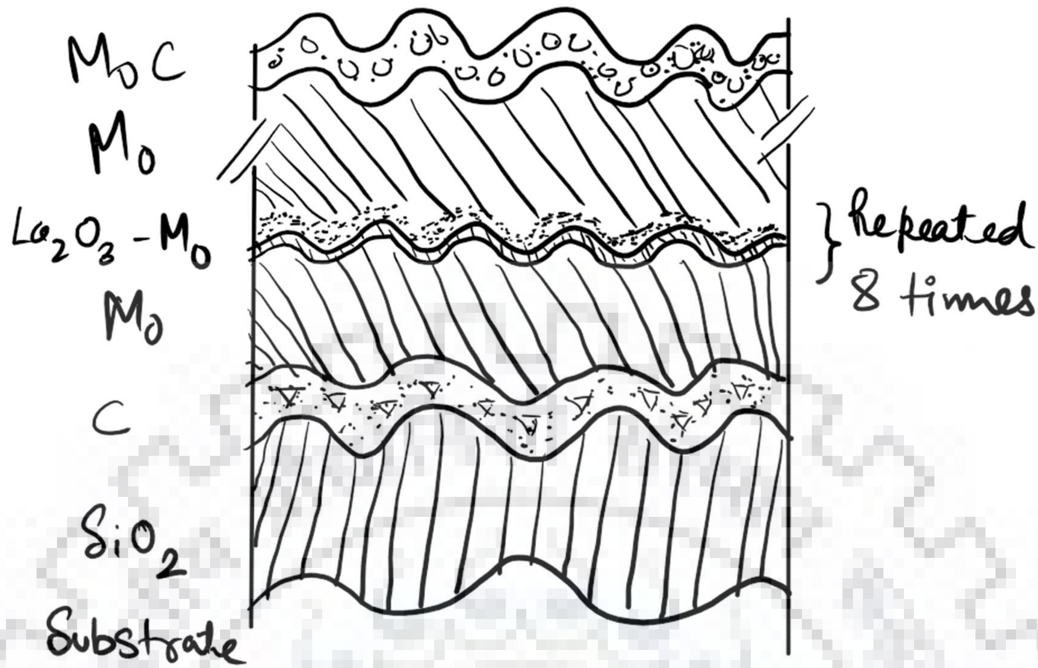

Figure 5.6: Schematic model of the interlayer configuration for Mo-(La_2O_3-Mo)$_8$-Si.

Figure 5.7 shows the best fit simulated data and the comparison of experimental data with the fitted one. The blue curve represents the experimental data and the red curves represent the fitted data.

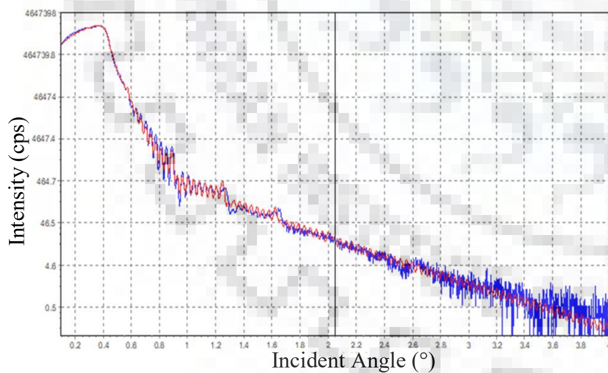

Layer	Layer Description	Density (g/cm^3)	Thickness (nm)	Roughness (nm)
4	Mo0.500 C0.500	2.5	1.7	0.3
3	Mo	10	9	1.7
2	Superlattice, Number of repeats= 8			
2.1	Mo0.300 La2O30.700	7.6	0.1	0.8
2.0	Mo	10	11	0.8
1	C	2.2	1.5	1.4
Substrate	SiO2	2.2	1000	0.2
Substrate	Si	2.2	600000	0.1

(a)

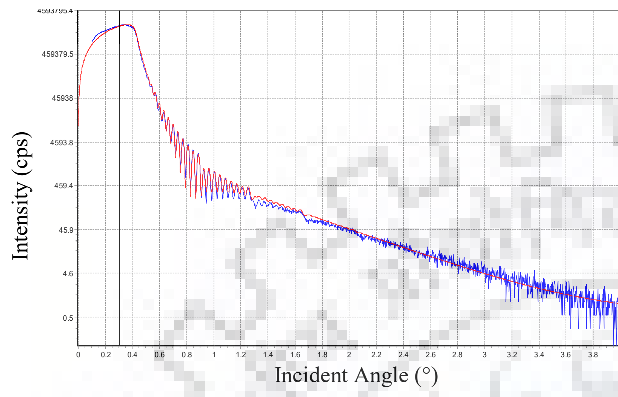

Layer	Layer Description	Density (g/cm^3)	Thickness (nm)	Roughness (nm)
4	Mo0.500 C0.500	8.3	0.6	1.8
3	Mo	10	11	1.2
2	Superlattice, Number of repeats= 8			
2.1	Mo0.300 La2O30.700	9.9	0.1	1.2
2.0	Mo	9.9	10.8	1
1	C	4.3	0.5	0.1
Substrate	SiO2	2.2	1000	0.2
Substrate	Si	2.2	600000	0.1

(b)

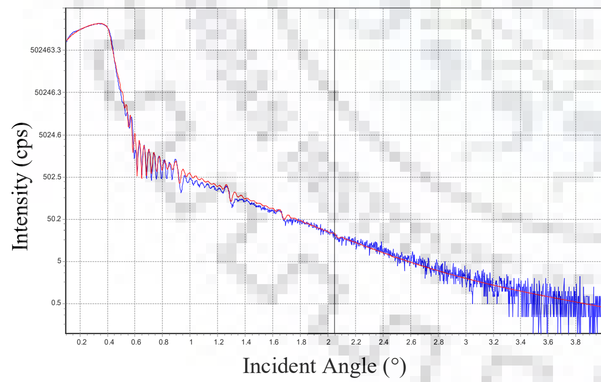

Layer	Layer Description	Density (g/cm^3)	Thickness (nm)	Roughness (nm)
4	Mo0.500 C0.500	7.9	0.5	2.5
3	Mo	9.6	9.6	3.3
2	Superlattice, Number of repeats= 8			
2.1	Mo0.300 La2O30.700	9.4	0.1	1.1
2.0	Mo	9.4	10.7	0.9
1	C	4.7	0.4	0.4
Substrate	SiO2	2.2	1000	0.2
Substrate	Si	2.2	600000	0.1

(c)

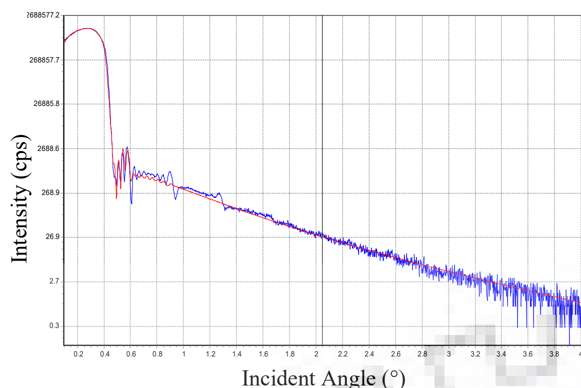

Layer	Layer Description	Density (g/cm^3)	Thickness (nm)	Roughness (nm)
4	Mo0.500 C0.500	8.6	5	5.1
3	Mo	9.8	9	7.9
2	Superlattice, Number of repeats= 8			
2.1	Mo0.300 La2O30.700	10.2	0.1	2.3
2.0	Mo	9.1	11	10
1	C	6.7	0.1	0.4
Substrate	SiO2	2.2	1000	0.2
Substrate	Si	2.2	600000	0.1

(d)

Figure 5.7: XRR fitted curve and simulated data for Mo-(La_2O_3-Mo)$_8$-Si multilayer thin film in, (a) as deposited, (b) annealed at 800 °C for 24 h, (c) annealed at 800 °C for 48 h, (d) annealed at 800 °C for 120 h, condition.

Based on the quantitative fitting results, it can be seen that the contamination layer thickness (top layer) of the film increases with the increase in the annealing duration owing to the possibility of the absorption of moisture or other gases when exposed to air. The density of the interlayers such as Mo and Mo-La_2O_3 mixed layer is close to that of the bulk value of pure Mo showing the minimum effect of lanthanum oxide on the density variation. The oxide on molybdenum layer, assuming that they are the compound of Mo and La_2O_3, are in-depth only sub-nanometer thick, thinner than an atomic monolayer.

Roughness of the top layer is quite consistent with the RMS average surface roughness of the film both in as-deposited and annealed condition. The slight difference in the observed roughness value is understandable as AFM only gives a local surface roughness while XRR is more statistical. With annealing, both surface and interface roughness increase and a 10-fold increase in the roughness of interlayer of Mo on the substrate side is observed. Since the specular intensity of the reflectivity curve is only sensitive to variation along the normal surface direction, it is difficult to differentiate between the interface roughness and the interfacial composition grading or diffuseness [86]. Therefore, it is not easy to determine the exact film or interfacial structure. Here, it has been assumed that sub-nanometer layer of lanthanum oxide is formed on the crevices and gaps of the Mo layer in the ratio of 70:30.

The density of the Mo layers are lower than that of the bulk value of 10.24 g/cm^3, indicating that these layers are not completely dense and could contain void. The thickness of top layer Mo is found to be about 5% less that the designed, however, the substrate side Mo layers have a good agreement with the intended thickness. The fitting of 120 h annealed sample is not reliable owing to large changes in the roughness, density and thickness values and requires a different film structure model to quantify the parameters and data from diffuse scattering.

5.6 XRD phase and structure analysis

Pure Mo and Mo/La_2O_3 films are polycrystalline and show the diffraction peaks associated with BCC Mo structure. The diffractograms of the out-of-plan XRD measurements of the films are shown in Figure 5.8. Owing to the very small content of La_2O_3 in the film (1 nm totals approx. 1 wt.%) it cannot be detected in XRD measurement of the thin film. All the films show a prominent peak of Mo (110) compared to other weak peaks. In addition to (110) peak, (220) and low intensity (211) peak of cubic Mo is also observed. From the XRD peaks, it can be seen that with annealing of the films, the peak intensity increases.

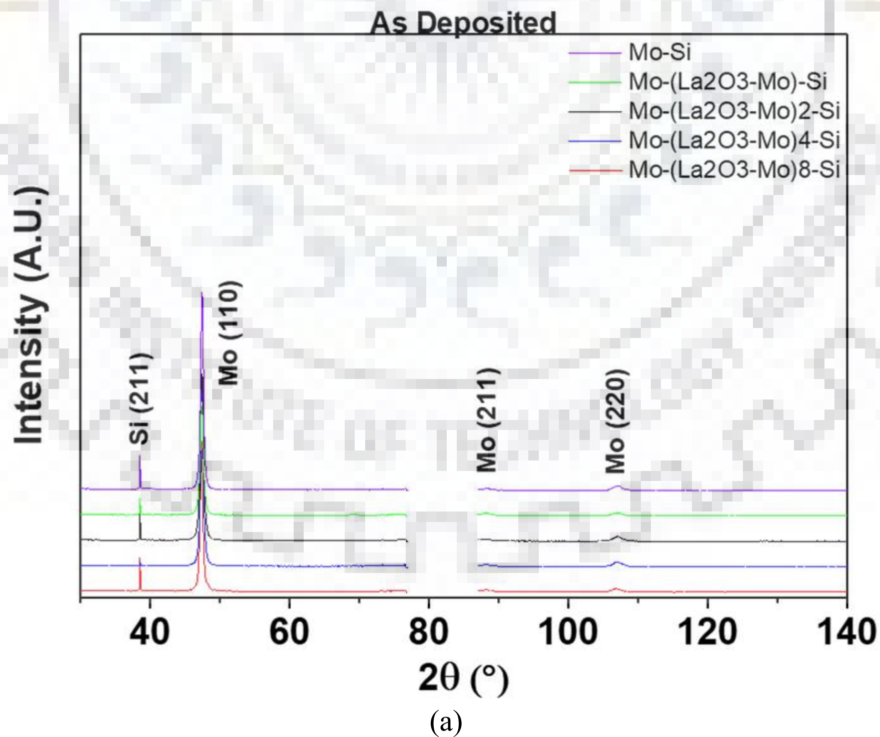

(a)

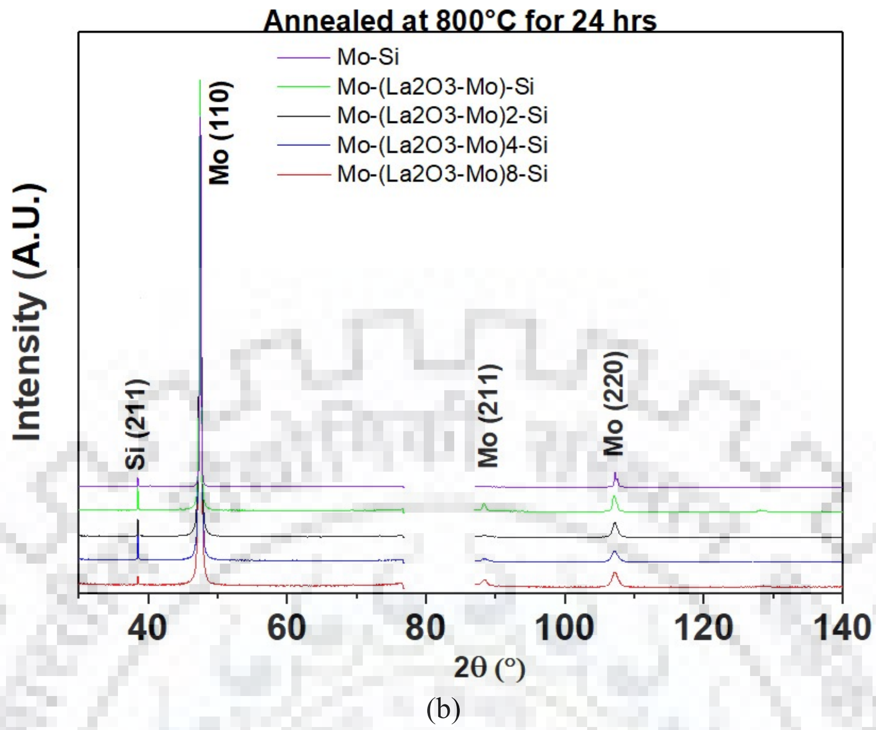

(b)

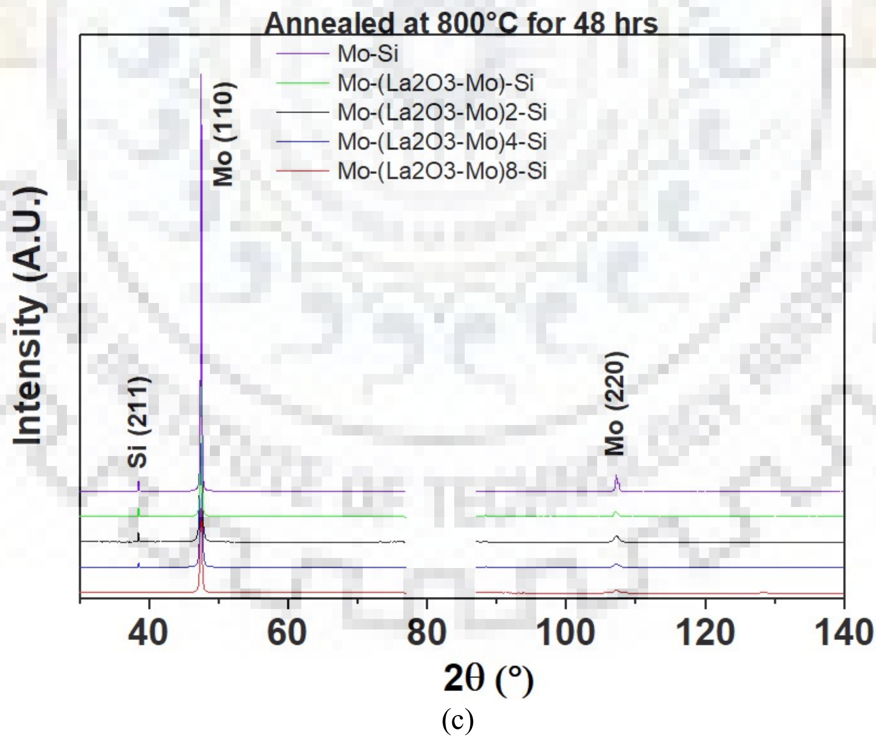

(c)

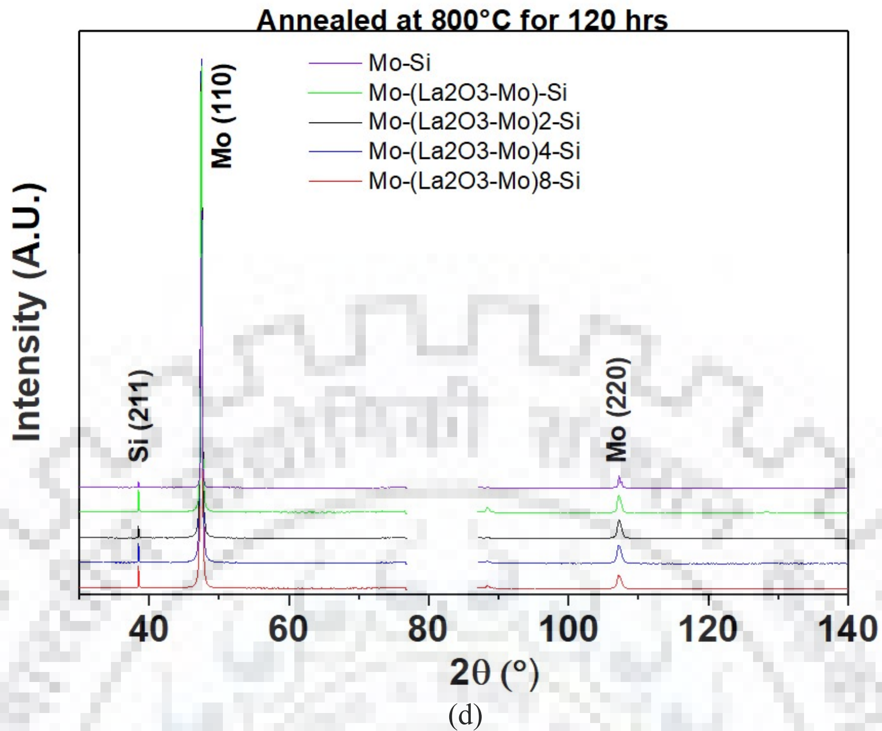

(d)

Figure 5.8: XRD pattern of multilayer thin film, (a) as deposited, (b) annealed at 800 °C for 24 h, (c) annealed at 800°C for 48 h, (d) annealed at 800 °C for 120 h, condition.

To have a clearer picture of the film microstructure though the diffraction lines with change in annealing duration, enlarged section of Mo peak in the range of 46-49° is shown in Figure 5.9. The 2θ angles for cubic Mo (110) and (220) are 47.5° and 107.8° respectively. Peak shifting is observed in the films upon annealing. The shift to higher theta value is due to existence of tensile stress in the films. Film annealed for 120 h show a smaller shift of XRD peak towards left. This is perfectly consistent with the residual stress measurement presented later in section 5.7.

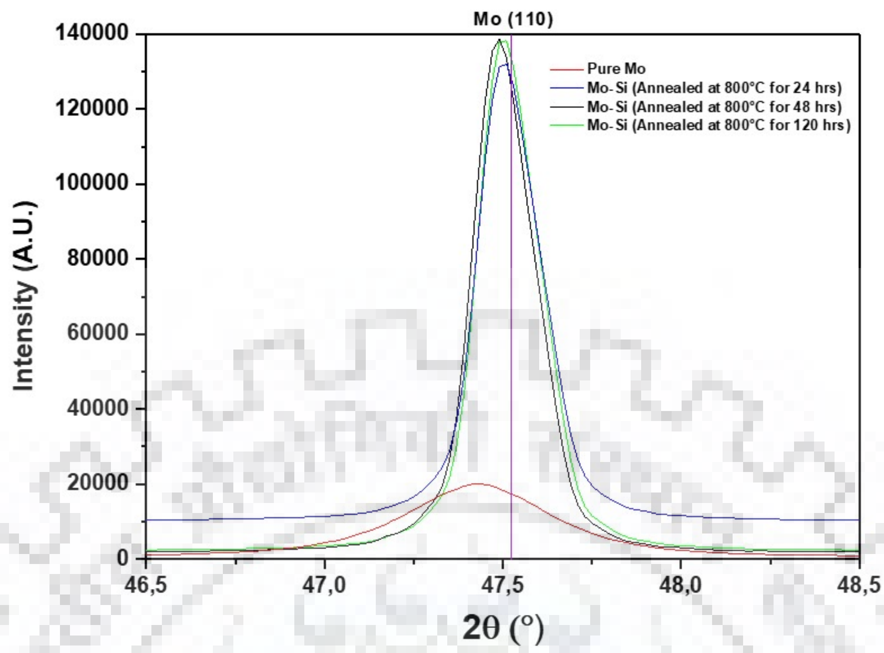

(a)

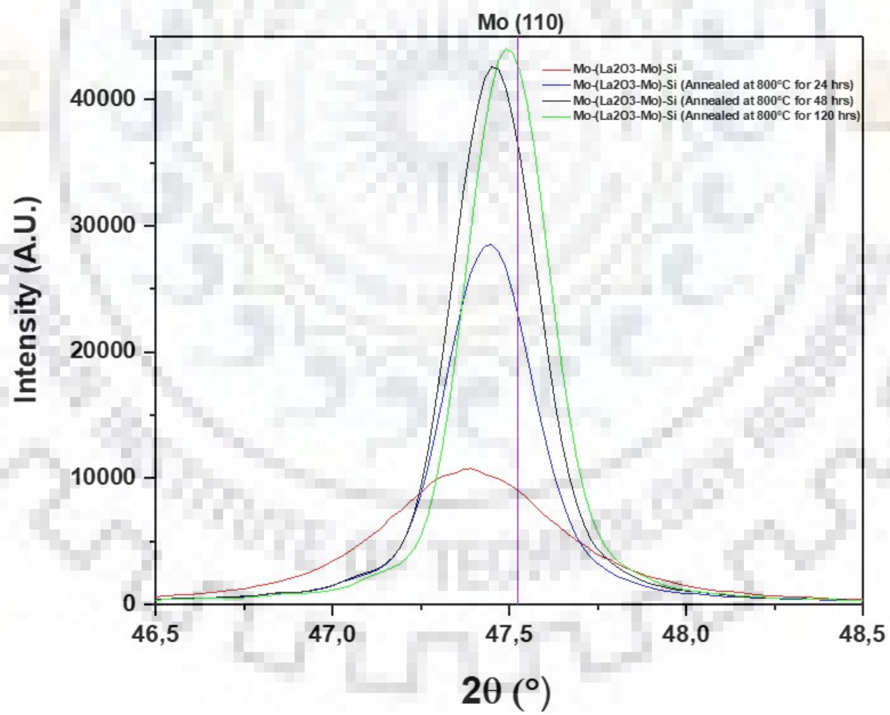

(b)

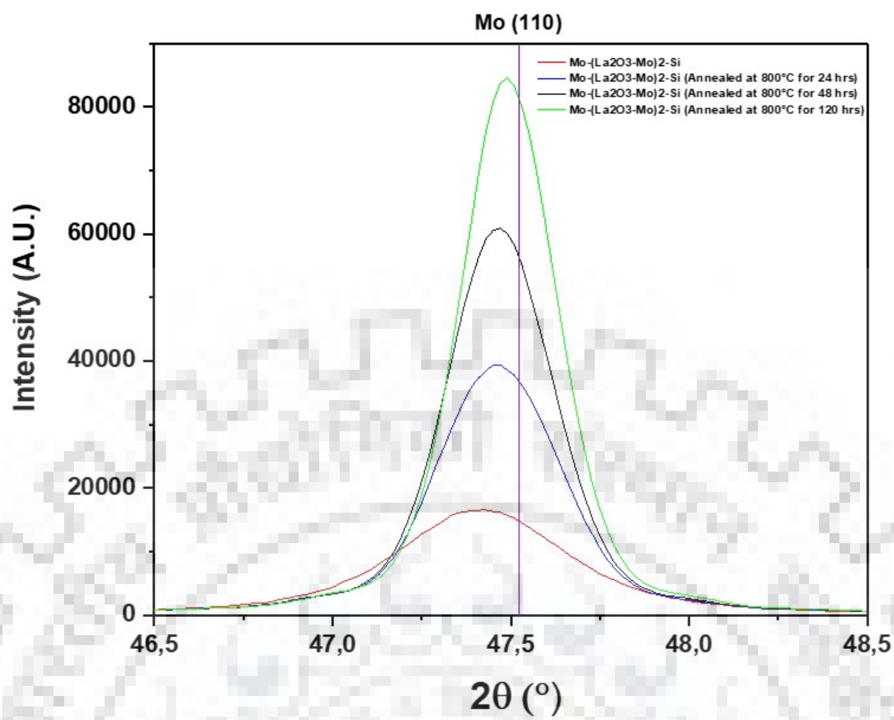

(c)

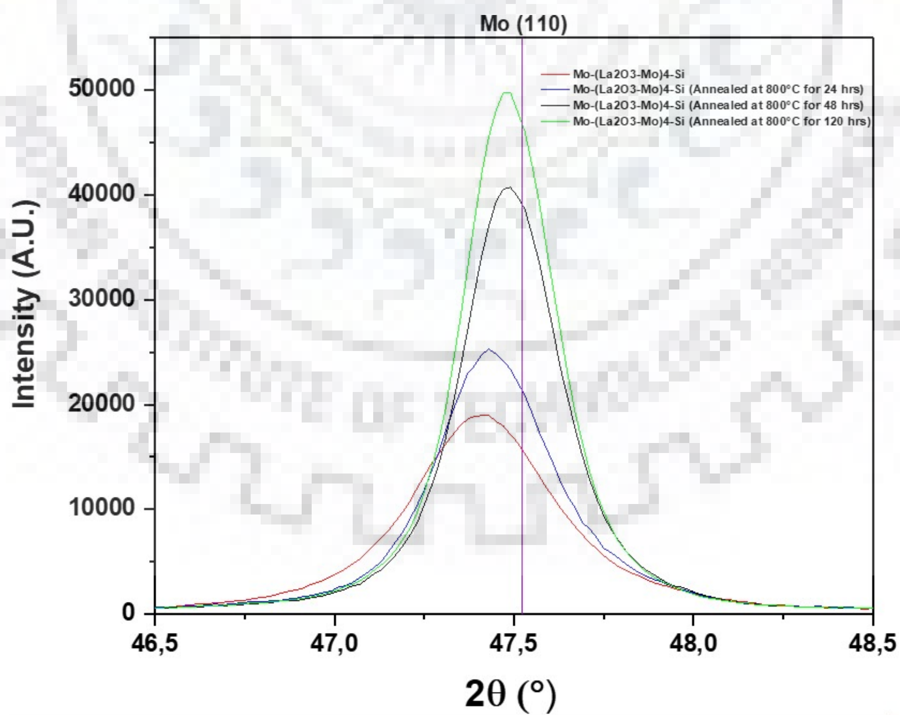

(d)

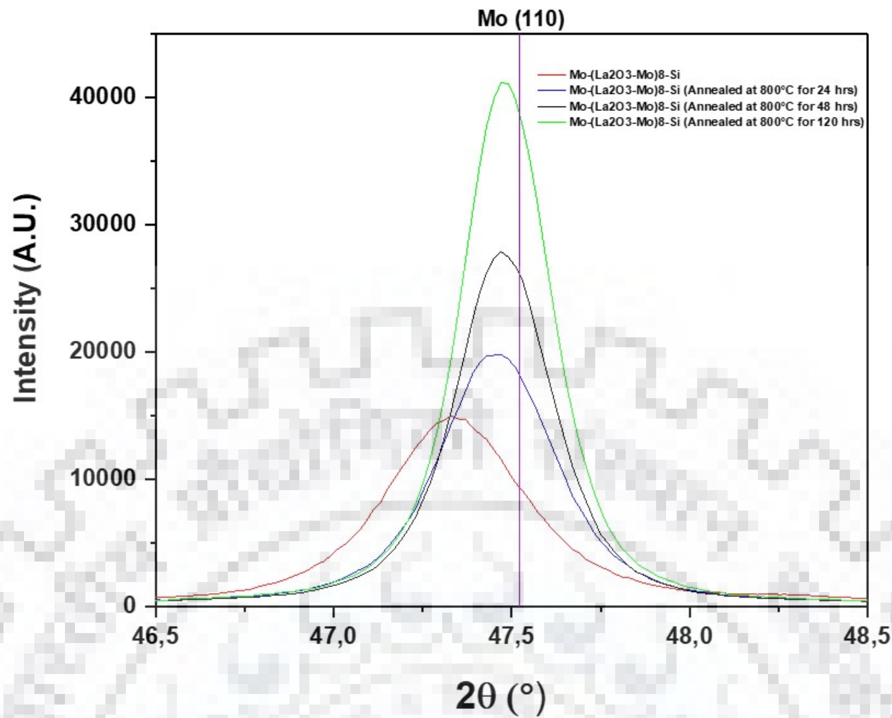

(e)

Figure 5.9: Enlarged XRD peak of Mo (110) in pure Mo and multilayer thin film in, (a) as deposited, (b) annealed at 800 °C for 24 h, (c) annealed at 800 °C for 48 h, (d) annealed at 800 °C for 120 h, condition.

The diffraction-line broadening was analysed using single line analysis discussed in section 4.2.6. The variation of volume-weighted grain size (out-of-plane grains) as a function of bilayer period and annealing duration has been plotted in Figure 5.10. It should be noted that the grain size is obtained only from the Mo (110) peak and hence the absolute values should be treated with care and used not only to understand trends in the grain size evolution.

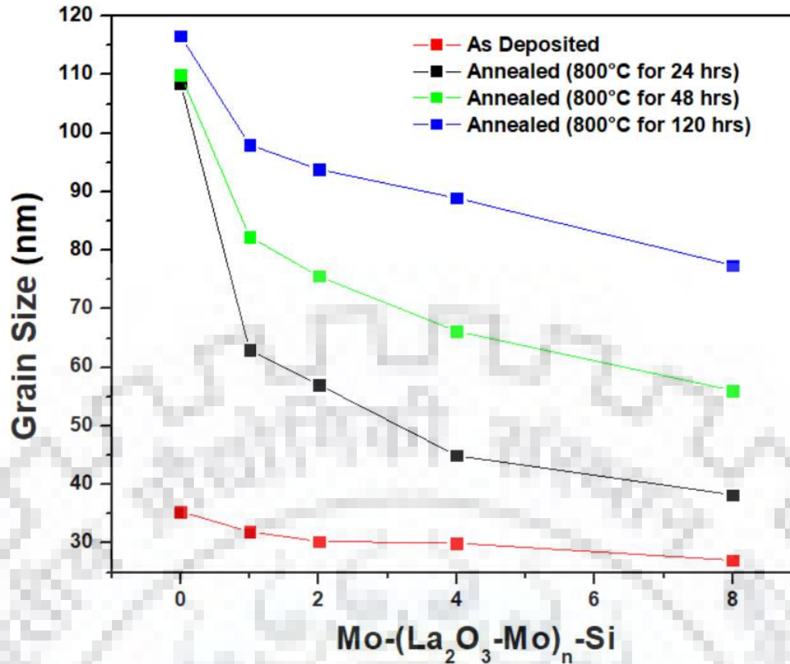

Figure 5.10: Volume weighted grain size as a function of bilayer period and annealing duration.

In as-deposited condition, the grain size of Mo in all the films is close to 30 nm. However just after 24 h annealing, the volume weighted grain size of Mo increases to 100 nm which is consistent with the FIB results showing Mo columnar grain extending through the film thickness. The out-of-plane grain size increases with annealing duration as is also evident from SEM/FIB images. Upon 24 h of annealing it can be seen that the extent of grain growth decreases with increasing number of bilayer periods. After 48 h of annealing, the extent of growth is more or less similar for all the multilayer films. Finally, after 120 h of annealing while grain size of only the Mo-(La_2O_3-Mo)-Si film reaches the film thickness value, the other films have consecutively lower grain sizes. Thus, it can be expected that with the increase in the bilayer period, there is an exponential decrease in the volume-weighted grain size due to the pinning effect of lanthanum oxide particles between the adjacent Mo columnar grains. The pinning effect is more effective in the film with 8 bilayer period leading to smaller grain size when compared to other multilayer films.

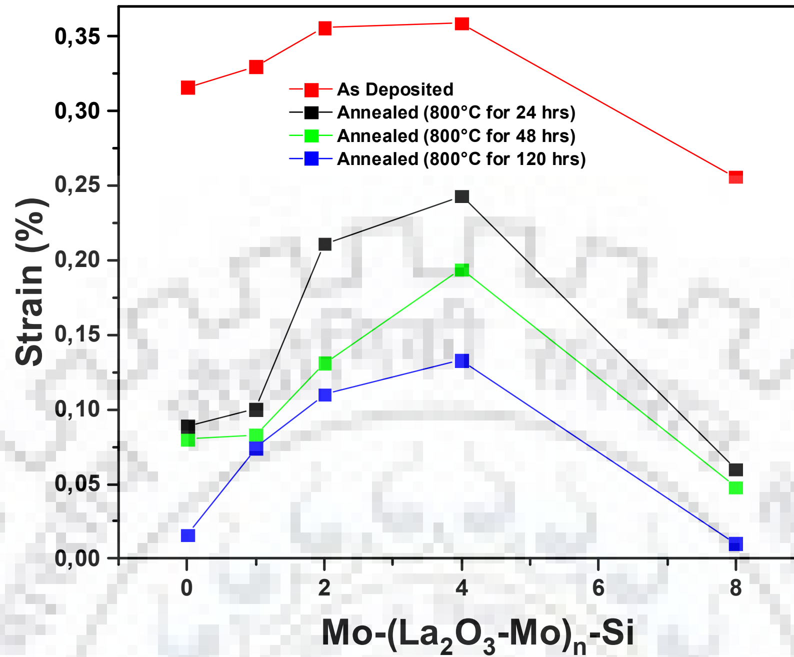

Figure 5.11: Microstrain as a function of bilayer period and annealing duration.

Owing to the presence of defects, dislocations, faults and twins, microstrain is also present in the thin film. In the present work, the microstrain has been determined using SLA and the obtained values has been plotted as a function of bilayer period and annealing duration as shown Figure 5.11. Annealing of films result in lowering of the strain value caused by the structural relaxation and annihilation of defects and dislocations. However, the microstrain initially increases with the increase in bilayer period upto 4 and then decreases to a value even lower than that of the pure Mo film with 8 bilayer period. This indicates that the film with 4 bilayer period is very unstable which is also seen from the FIB images. However, the film with 8 bilayer period is the most stable structure probably due to uniform distribution of oxide particles in the film matrix. The decrease in the microstrain value can also be linked to the reduced net effect of the lattice strain due to formation of high number of dislocation and defects which results in the strain cancellation in the growth direction. Moreover, the presence of microstrain in the multilayer films is a result of lattice mismatch between the film and substrate or/and between the different layers [87]. The combined effect of small crystallite size and high number of interfaces (interfacial scattering) results in higher resistivity values of these films with increasing the number of bilayer periods.

5.7 Interfacial structure analysis

Considering the above results, Mo-(La_2O_3-Mo)$_8$-Si has been found to be the most stable and uniform multilayer film configuration. Therefore, to have a direct observation and a better understanding of the oxide interaction within the film, 120 h annealed sample have been analysed as a preliminary investigation. Figure 5.12 shows the bright field C-TEM image of the film confirming the presence of large columnar grains of Mo extending through the layers. The interlayers of La_2O_3 are also clearly visible (marked with numbers) in the image. From the image it can be seen that the interlayer of La_2O_3 is not closed and distinct agglomerates of La_2O_3 cab be discerned.

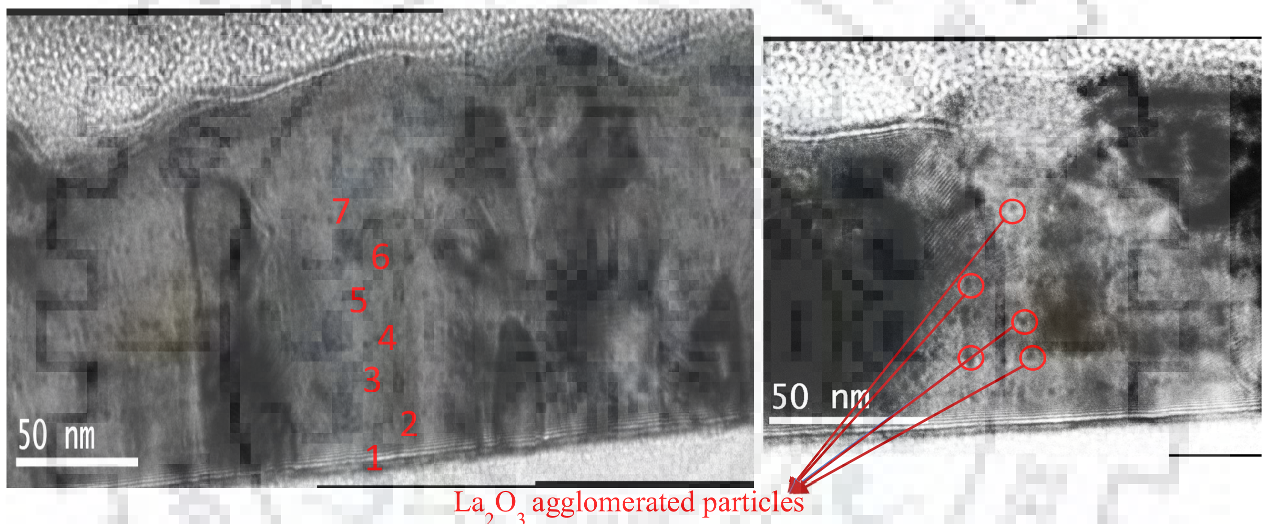

Figure 5.12: Cross-sectional bright-field C-TEM of sample Mo-(La_2O_3-Mo)$_8$-Si.

It is interesting to see that the lanthanum oxide particles do not diffuse into the Mo layers even after 120 h of annealing at 800 °C and are present as agglomerated particles. EDX (Figure 5.13) confirms the presence of lanthanum in the interlayers and absence within the Mo layer which indicates that diffusion of lanthanum needs a much higher temperature than 800 °C.

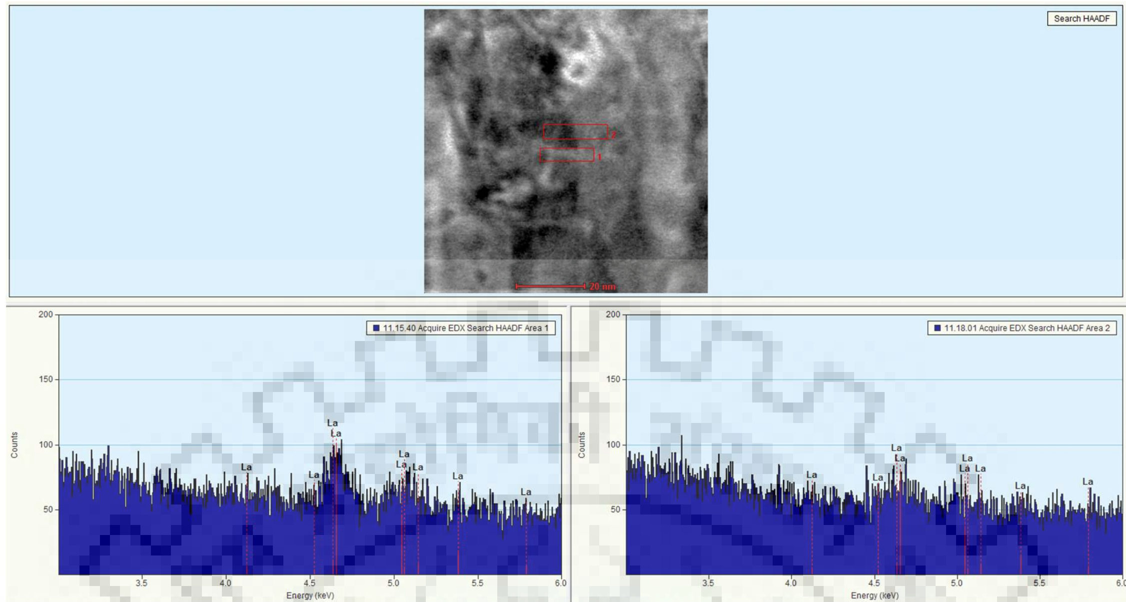

Figure 5.13: EDX spectra of interlayer area 1 & 2 present in sample Mo-(La_2O_3-Mo)$_8$-Si.

5.8 Curvature based residual stress measurement

As explained in section 3.5, there are two kinds of residual stresses which elucidate different film structures. Usually, it is observed that porous film give rise to tensile stress while a dense film exhibits compressive stress. Table 5.3 represents the residual stresses in as-deposited and 24 h annealed condition for pure Mo and multilayer thin films determined using curvature method. The stress values are then plotted as a function of bilayer periods as shown in Figure 5.14.

Table 5.3: Residual stresses in thin films obtained using curvature method.

Samples	**Residual stress (MPa)**	
	As-Deposited	**Annealed (800 °C for 24 h)**
Mo-Si	173	267
Mo-(La_2O_3-Mo)-Si	286	669
Mo-(La_2O_3-Mo)$_2$-Si	160	462
Mo-(La_2O_3-Mo)$_4$-Si	124	230
Mo-(La_2O_3-Mo)$_8$-Si	368	451

Since Mo and La_2O_3 has different crystal structure, the interface formed between them is incoherent causing formation of lattice strains within the interlayers. The lattice mismatch strain between Mo and La_2O_3 can be calculated using the following equation [88]:

$$\varepsilon_s = \frac{2(a_{La2O3} - a_{Mo})}{a_{La2O3} + a_{Mo}} = 7.64\% \qquad 5.1$$

Therefore, interface stress could greatly affect the stress behaviour of the films [89]. Misfit strain between the incoherent layers can result in alternating strain field.

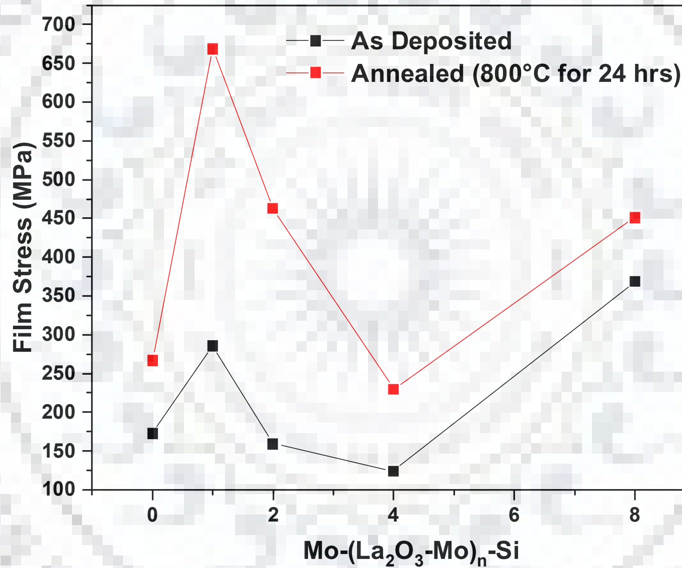

Figure 5.14: Residual stress variation in the multilayer films in as-deposited and annealed condition.

Tensile stress is generally described through grain boundary relaxation. With the relaxation, the intergranular forces across interfaces lead to grain boundary deformation. Intragrain tensile force arising from the constraints imposed by the substrate balances this deformation [90].

From figure 29, it is observed that the tensile stress increases in the films when annealed which is contrary to results observed in bulk materials. Intrinsic stress in the films depend largely on the grain size and governed by the presence of interfaces. It is known that grain boundary are regions in the material which has majority of spaces to accommodate impurities or defects and reduces the strain in

the material as a result of atomic diffusion. When the film is annealed, the grain boundary region is decreased causing the interfacial stress to rise significantly. Due to this reason, the stress in the annealed film increases when compared to as-deposited films.

However, there is no particular trend observed in the intrinsic stress value with the changes in the bilayer period. It can be seen that film with 4 bilayer period shows the lowest tensile stress compared to pure Mo. Generally, it is expected that the residual stress increases with the increase in the interfaces, Nevertheless, the Mo/La_2O_3 films exhibit certain abnormality indicating that there may be other factors that govern the stress values.

An interesting thing to be noted is that the increase in the stress value is minimum for the film with 8 bilayers after 24 h of annealing. In general, the resistivity of the material increases with the increases in the internal stress due to induced defects and dislocations. vdP measurements also confirms that the resistivity is more for the higher stressed films is as-deposited condition. This factor could also contribute to the higher resistivity besides the small grain size and high number of interfaces.

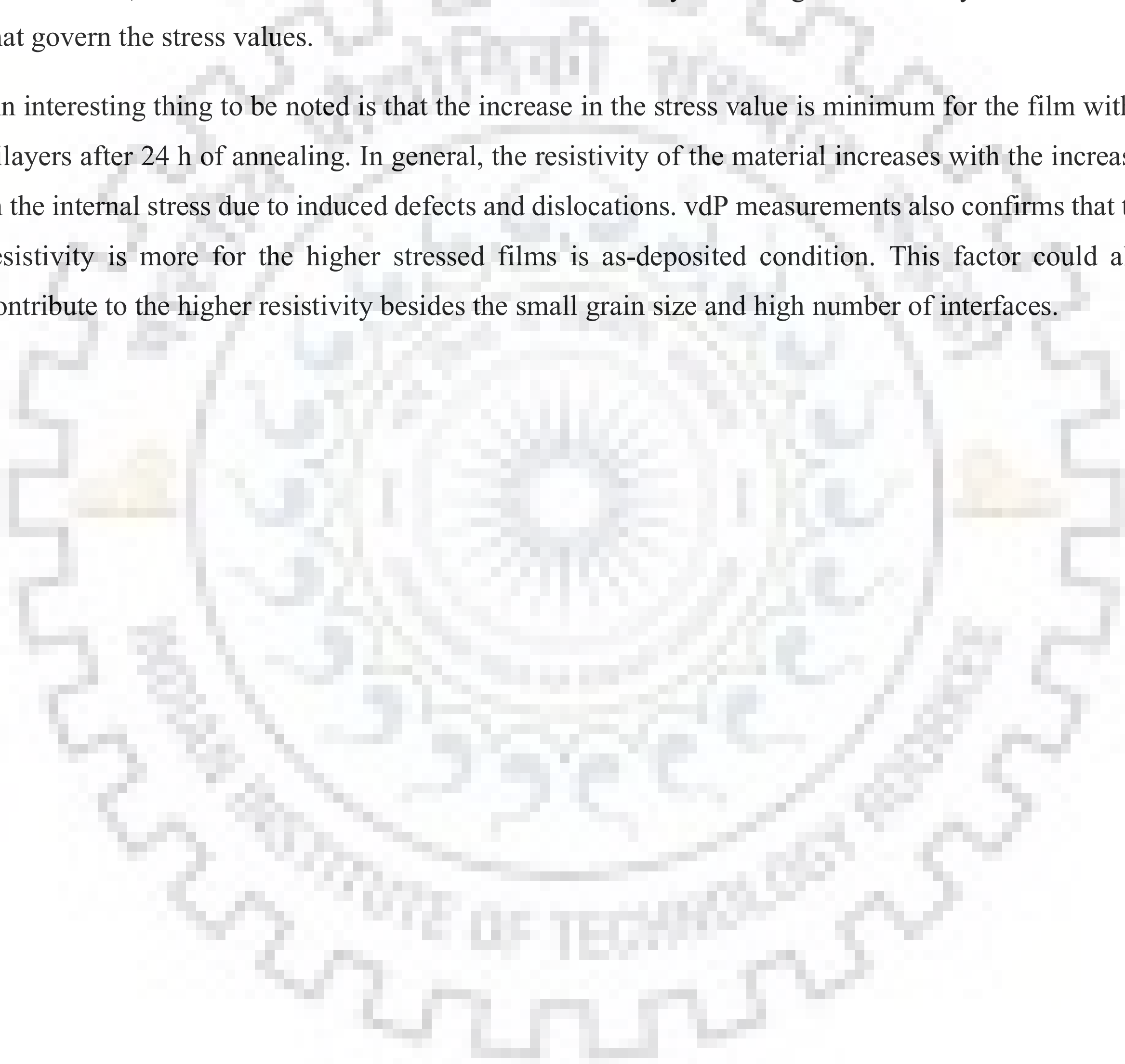

6. Conclusion

This study discusses the microstructural and electrical characteristics of Mo/La_2O_3 nano multilayers in as-deposited and heat-treated conditions with different annealing durations. About 1.1 wt.% of lanthanum oxide was distributed through the film with varying individual film thickness of each material component in such a way that the overall composition remains the same. Based on the results following conclusions were drawn:

1. Pure Mo and multilayer Mo/La_2O_3 films exhibited size related phenomena causing 100 % or more increase in the electrical resistance owing to electron scattering though surface/interface, grain boundary, defects and roughness adding basically to the net resistance. The electrical resistivity of the films was found to increase with the increase in the number of bilayer periods due to increasing contribution from interface scattering. Annealing the films led to reduction in the resistivity owing to increased grain size leading to lowering of grain boundary scattering. Mo film vacuum annealed for 120 h showed lowest resistivity of 8.2 μΩ.cm (close to the bulk value). The lower conductivity of the multilayer films compared to pure Mo film can be attributed to the addition of a highly resistive oxide layer and the increased surface and interface scattering along with reduced grain size. For multilayer films with 4 and 8 bilayer periods, increase in resistivity value from as-deposited condition was observed after 24 h of annealing. The reason for this is presently unclear and would require further investigations. The resistivity of all the films reduce upon further annealing steps indicating their thermal stability for extended durations.

2. All the films were found to be polycrystalline and exhibited similar morphology of tiny elongated rice grain-like features in the as-deposited state. The obtained films were crack free. These grains are columnar in shape when viewed cross-sectionally and are found to be discontinuous and tapered in shape. However, after annealing, the grain grows continuously and span through the 100 nm thickness of the pure Mo film. Addition of La_2O_3 layer in the films in alternating patterns causes some Mo grains to grow while some get interrupted by the oxide particles in the layer indicating that oxide layer formed is incomplete. This effect is more pronounced and clearly seen after the films have been annealed at 800 °C for different time durations. The in-plane grain size reduces with the increase in the number of bilayer period both in as-deposited and annealed condition owing to the grain growth suppression caused by the addition of second phase oxide particles. Upon annealing for 120 h, the grain size distribution looks more uniform with increasing number of bilayer periods.

3. Increase in the surface roughness value was detected as evident from the SEM and FIB images. There is no exact trend to the RMS roughness with the change in the bilayers. Nevertheless, it is interesting to note that the RMS roughness value is almost similar in case of the as-deposited pure Mo and multilayer films. The percent change in the roughness upon annealing upto 120 h is lowest for the 8 bilayer period film indicating its higher thermal stability compared to others film configurations. More is the bilayer period, the second phase distribution through the complete film becomes uniform resulting in lower surface roughness value.

4. The films structure was analysed using the X-ray reflectivity measurements in order to know the density, thickness and roughness of the individual layers before and after annealing as well as to notice changes in the film layer configuration. The thickness of the as-deposited individual layers in pure Mo and Mo/La_2O_3 multilayer films was found close to the intended values. With annealing, the decay of the oscillation fringes and spectral intensity was observed indicating the increase in interface and surface roughness of the films. The appearance of the Bragg peaks provides evidence that these multilayer samples have a good periodic structure along the growth direction. The fringes can be clearly seen in the film reflectivity profile even after 5 days of annealing indicating that the layers have been separated out further rather than intermixing. XRR fittings and simulations were performed to evaluate the individual layers parameters such as density, thickness and roughness based on the assumption that the layers formed are grown as a superlattice structure. Fittings performed on Mo-(La_2O_3-Mo)$_8$-Si showed that the density of all the Mo layer before and after annealing were lower than that of bulk value of 10.24 g/cm^3 implying that layers formed are not dense. The top layer roughness of this multilayer configuration conforms with the values of RMS surface roughness value obtained by AFM. The fitting for layer thickness is however not reliable for this configuration after annealing.

5. Phase analysis of these films show diffraction peaks associated with BCC Mo structure corresponding to cubic (110) and (220) planes. There is no peak observed for the oxide layer in the XRD diffractograms due to its low content. The increase in the peak intensity of the films is also observed after annealing owing to grain growth. Peak shifting also occurs when films are subjected to vacuum annealing which is attributed to the presence of tensile stress in the films as confirmed by the residual stress measurements. Using single line analysis, the volume weighted crystallite size and microstrain of the multilayer films were determined. The observations based on the crystallite size variation were in agreement with the results of SEM, FIB and AFM. As evident, the microstrain in the films decreases with the annealing duration because of structural relaxation. Mo-(La_2O_3-Mo)$_8$-Si film showed the lowest microstain value both in as-deposited and heat-treated condition owing to structural uniformity and thermal stability achieved by homogeneous dispersion of oxide particles.

6. TEM investigation on 120 h vacuum annealed Mo-(La_2O_3-Mo)$_8$-Si film showed the clear presence of lanthanum oxide interlayers distinctly separated without any intermixing or diffusion. Also, agglomerated La_2O_3 particles distantly spaced along the interlayers are observed causing the electron interface scattering to be less pronounced resulting in low resistivity values.

7. Future Scope

Based on the electrical and microstructural investigation, Mo/La_2O_3 nano multilayers can be regarded as a potential metallization system for SAW based high temperature sensors. These multilayer thin films are stable upto 800 °C without considerable thermal and microstructural damage and at the same time maintaining a good electrical conductivity. However, electrical properties also depend on the amount of second phase present in the film. Following steps can be opted in future for the deeper understanding of the behaviour of the present material system:

1. In the present case, approximately 1.1 wt.% of lanthanum oxide was used for fabricating the film corresponding to a total of 1 nm layer thick La_2O_3 and 99 nm of Mo making a total thickness of 100 nm. Since the oxide phase with the present composition does not form a complete layer, the distribution is quite random through the film. So, a higher content of the lanthanum oxide can be an alternative option in future with higher number of bilayer periods i.e. 16 to have a more uniform oxide dispersion effect in the films and increased thermal stability.

2. Also, these films can be annealed at temperature higher than 800 °C for longer durations as pure Mo and multilayer films does not degrade even after 120h of vacuum heating. Moreover, there is no diffusion observed in the films at 800 °C. Therefore, a higher annealing temperature can give us the information related to thermal damage conditions and diffusion of the oxides through the interfaces.

3. For the high temperature stable IDT material, the roughness of the film should be as low as possible. More is the number of bilayer period in the films, finer will be its microstructure corresponding to even distribution of the La_2O_3 particles resulting in lower roughness. Another important factor that needs to taken into consideration is the high temperature strength of the IDT material at temperatures 800 °C or higher. Therefore, the uniform distribution of the second phase particles is very crucial in order to ensure the high temperature stability.

Having said that, these Mo/La_2O_3 multilayers can open a new window for high temperature SAW devices with improved thermo-mechanical properties without comprising on the electrical behaviour.

References

[1] J. H. T. Grandke, *Sensors: A Comprehensive Survey*, vol. 1. Weinheim, Germany: VCH Publisher, 1989.

[2] X. J. Huang and Y. K. Choi, “Chemical sensors based on nanostructured materials,” *Sensors Actuators, B Chem.*, vol. 122, no. 2, pp. 659–671, 2007.

[3] R. M. White and F. W. Voltmer, “Direct piezoelectric coupling to surface elastic waves,” *Appl. Phys. Lett.*, vol. 7, no. 12, pp. 314–316, 1965.

[4] D. P. Morgan, “History of SAW devices,” in *Proceedings of the 1998 IEEE International Frequency Control Symposium (Cat. No.98CH36165)*, pp. 439–460.

[5] C. Campbell, *Surface acoustic wave devices for mobile and wireless communications*. Academic Press, 1998.

[6] R. Weigel, D. P. Morgan, J. M. Owens, A. Ballato, K. M. Lakin, K. Hashimoto, and C. C. W. Ruppel, “Microwave acoustic materials, devices, and applications,” *IEEE Trans. Microw. Theory Tech.*, vol. 50, no. 3, pp. 738–749, Mar. 2002.

[7] D. S. Ballantine, *Acoustic wave sensors : theory, design, and physico-chemical applications*. Academic Press, 1997.

[8] F. Schmidt and G. Scholl, “Wireless SAW identification and sensor systems,” *Int. J. High Speed Electron. Syst.*, pp. 1143–1191, Jan. 2000.

[9] J. Ma, J. Yang, B. Du, L. Wang, H. M. Jiang, and J. He, “Design of SAW Specific Gas Sensor with High Sensitivity,” *Appl. Mech. Mater.*, vol. 303–306, pp. 137–142, Feb. 2013.

[10] A. Binder, G. Bruckner, N. Schobernig, and D. Schmitt, “Wireless Surface Acoustic Wave Pressure and Temperature Sensor With Unique Identification Based on LiNbO3,” *IEEE Sens. J.*, vol. 13, no. 5, pp. 1801–1805, May 2013.

[11] Lord Rayleigh, “On Waves Propagated along the Plane Surface of an Elastic Solid,” *Proc. London Math. Soc.*, vol. s1-17, no. 1, pp. 4–11, Nov. 1885.

[12] R. Singh, S. K. R. S. Sankaranarayanan, and V. R. Bhethanabotla, “Enhanced surface acoustic wave biosensor performance via delay path modifications in mutually interacting multidirectional transducer configuration: A computational study,” *Appl. Phys. Lett.*, vol. 95, no. 3, 2009.

[13] S. R. Heron, R. Wilson, S. A. Shaffer, D. R. Goodlett, and J. M. Cooper, "Surface acoustic wave nebulization of peptides as a microfluidic interface for mass spectrometry," *Anal. Chem.*, vol. 82, no. 10, pp. 3985–3989, 2010.

[14] J. Hornsteiner, E. Born, G. Fischerauer, and E. Riha, "Surface acoustic wave sensors for high-temperature applications," in *Proceedings of the 1998 IEEE International Frequency Control Symposium (Cat. No.98CH36165)*, pp. 615–620.

[15] R. Behanan, S. C. Moulzolf, M. Call, G. Bernhardt, D. Frankel, R. J. Lad, and M. P. Da Cunha, "Thin films and techniques for SAW sensor operation above 1000°C," *IEEE Int. Ultrason. Symp. IUS*, pp. 1013–1016, 2013.

[16] A. R. John Vetelino, *Introduction to Sensors*, 1st Editio. CRC Press, 2010.

[17] C. K. Campbell, I. Eee, and A. S. A. W. Development, "Applications of Surface Acoustic and Shallow Bulk Acoustic Wave Devices," vol. 77, no. 10, 1989.

[18] J. Haines, O. Cambon, D. A. Keen, M. G. Tucker, and M. T. Dove, "Structural disorder and loss of piezoelectric properties in α-quartz at high temperature," *Appl. Phys. Lett.*, vol. 81, no. 16, pp. 2968–2970, 2002.

[19] H. Fritze, "High-temperature piezoelectric crystals and devices," *J. Electroceramics*, vol. 26, no. 1–4, pp. 122–161, Jun. 2011.

[20] K. Shimamura, H. Takeda, T. Kohno, and T. Fukuda, "Growth and characterization of lanthanum gallium silicate La3Ga5SiO14 single crystals for piezoelectric applications," *J. Cryst. Growth*, vol. 163, no. 4, pp. 388–392, Jun. 1996.

[21] F. Kubat, W. Ruile, C. Eberl, T. Hesjedal, and L. M. Reindl, "Qualitative and quantitative analysis of acoustomigration effects in SAW-devices," *Microelectron. Eng.*, vol. 82, no. 3–4 SPEC. ISS., pp. 655–659, 2005.

[22] J. A. Thiele and M. P. Da Cunha, "Platinum and palladium high-temperature transducers on langasite," *IEEE Trans. Ultrason. Ferroelectr. Freq. Control*, vol. 52, no. 4, pp. 545–549, 2005.

[23] M. P. da Cunha, T. Moonlight, R. Lad, D. Frankel, and G. Bernhard, "High temperature sensing technology for applications up to 1000°C," in *2008 IEEE Sensors*, 2008, pp. 752–755.

[24] M. N. Hamidon, V. Skarda, N. M. White, F. Krispel, P. Krempl, M. Binhack, and W. Buff, "Fabrication of high temperature surface acoustic wave devices for sensor applications,"

Sensors Actuators, A Phys., vol. 123–124, pp. 403–407, 2005.

[25] D. Richter, S. Sakharov, E. Forsén, E. Mayer, L. Reindl, and H. Fritze, "Thin film electrodes for high temperature surface acoustic wave devices," *Procedia Eng.*, vol. 25, pp. 168–171, 2011.

[26] G. Bernhardt, C. Silvestre, N. Le Cursi, S. C. Moulzolf, D. J. Frankel, and R. J. Lad, "Performance of Zr and Ti adhesion layers for bonding of platinum metallization to sapphire substrates," *Sensors Actuators, B Chem.*, vol. 77, no. 1–2, pp. 368–374, 2001.

[27] U. Robert G. Johnson, James O. Holmen, Ronald B. Foster, "Adhesion layer for platinum based sensors," 23-Dec-1988.

[28] Y. Q. Fu, J. K. Luo, N. T. Nguyen, A. J. Walton, A. J. Flewitt, X. T. Zu, Y. Li, G. McHale, A. Matthews, E. Iborra, H. Du, and W. I. Milne, "Advances in piezoelectric thin films for acoustic biosensors, acoustofluidics and lab-on-chip applications," *Prog. Mater. Sci.*, vol. 89, pp. 31–91, 2017.

[29] G. K. Rane, S. Menzel, T. Gemming, and J. Eckert, "Microstructure, electrical resistivity and stresses in sputter deposited W and Mo films and the influence of the interface on bilayer properties," *Thin Solid Films*, vol. 571, pp. 1–8, Nov. 2014.

[30] M. Seifert, G. K. Rane, S. B. Menzel, and T. Gemming, "TEM studies on the changes of the composition in LGS and CTGS substrates covered with a RuAl metallization and on the phase formation within the RuAl film after heat treatment at 600 and 800 °C," *J. Alloys Compd.*, vol. 664, pp. 510–517, Apr. 2016.

[31] M. Spindler, S. B. Menzel, J. Eckert, and C. Eggs, "Influence of Al on resistance and power durability of Cu-based SAW metallizations," *IOP Conf. Ser. Mater. Sci. Eng.*, vol. 8, no. 1, p. 012013, Feb. 2010.

[32] K. Wetzig and C. M. (Claus M. Schneider, *Metal based thin films for electronics*. Weinheim: Wiley-VCH, 2006.

[33] M. Jubault, L. Ribeaucourt, E. Chassaing, G. Renou, D. Lincot, and F. Donsanti, "Optimization of molybdenum thin films for electrodeposited CIGS solar cells," *Sol. Energy Mater. Sol. Cells*, vol. 95, pp. S26–S31, May 2011.

[34] S. K. Samanta, W. J. Yoo, G. Samudra, E. S. Tok, L. K. Bera, and N. Balasubramanian, "Tungsten nanocrystals embedded in high-k materials for memory application," *Appl. Phys. Lett.*, vol. 87, no. 11, p. 113110, Sep. 2005.

[35] S. Petroni, C. La Tegola, G. Caretto, A. Campa, A. Passaseo, and R. Cingolani, “Aluminum Nitride piezo-MEMS on polyimide flexible substrates,” *Microelectron. Eng.*, vol. 88, no. 8, pp. 2372–2375, Aug. 2011.

[36] R. Zhang, Z. Huo, X. Jiao, . JieYang, B. Du, H. Zhong, and Y. Shi, “Deposition of Molybdenum Thin Films on Flexible Polymer Substrates by Radio Frequency Magnetron Sputtering,” *J. Nanosci. Nanotechnol.*, vol. 16, no. 8, pp. 8154–8159, Aug. 2016.

[37] S.-J. S. Sung-Guk An, Dong-Un Jin, Hyung-Sik Kim, Tae-Woong Kim, Young-Gu Kim, “Flexible display and method for manufacturing the same,” EP2290726 A1, 2010.

[38] J. J. A. Shields, “Applications of Mo Metal and Its Alloys,” *Int. Molybdenum Assoc. London*, 1995.

[39] S. R. Agnew and T. Leonhardt, “The low-temperature mechanical behavior of molybdenum-rhenium,” *JOM*, vol. 55, no. 10, pp. 25–29, Oct. 2003.

[40] H.C. Starck Fabricated Products, “High Temperature Alloys for Furnace Applications,” *AZoM*, 2017. [Online]. Available: https://www.azom.com/article.aspx?ArticleID=13926. [Accessed: 07-Apr-2018].

[41] M. K. Yoo, Y. Hiraoka, and J. Choi, “Recrystallization of molybdenum wire doped with lanthanum oxide,” *Int. J. Refract. Met. Hard Mater.*, vol. 13, no. 4, pp. 221–227, 1995.

[42] G. J. Zhang, Y. J. Sun, R. M. Niu, J. Sun, J. F. Wie, B. H. Zhao, and L. X. Yang, “Microstructure and strengthening mechanism of oxide lanthanum dispersion strengthened molybdenum alloy,” *Adv. Eng. Mater.*, vol. 6, no. 12, pp. 943–948, 2004.

[43] M. K. Yoo, Y. Hiraoka, and J. Choi, “Recrystallization of molybdenum wire doped with lanthanum oxide,” *Int. J. Refract. Met. Hard Mater.*, vol. 13, no. 4, pp. 221–227, Jan. 1995.

[44] A. . Mueller, R. Bianco, and R. . Buckman, “Evaluation of oxide dispersion strengthened (ODS) molybdenum and molybdenum–rhenium alloys,” *Int. J. Refract. Met. Hard Mater.*, vol. 18, no. 4–5, pp. 205–211, Jan. 2000.

[45] M. Endo, K. Kimura, T. Udagawa, … S. T.-H. T. H., and U. 1990, “The effects of doping molybdenum wire with rare-earth elements,” *High Temp. High Press.*, vol. 22(2), pp. 129–137, 1990.

[46] J. X. Zhang, L. Liu, M. L. Zhou, Y. C. Hu, and T. Y. Zuo, “Fracture toughness of sintered Mo-

La2O3 alloy and the toughening mechanism," *Int. J. Refract. Metals Hard Mater.*, vol. 17, no. 6, pp. 405–409, 1999.

[47] S. Q. Deng and Z. C. Liu, "," in *proc. 6th refractory metals*, 1990, p. 103.

[48] R. Bianco and R. W. Buckman, "Mechanical properties of oxide dispersion strengthened(ODS) molybdenum," *Molybdenum molybdenum Alloy.*, pp. 125–142, 1998.

[49] H.C. Starck, "High Performance Solutions with MoLa Alloys," 2017. [Online]. Available: https://www.hcstarck.com/hcs-admin/file/ae23e4b248d030140149754c51d64a36.de.0/mola_alloys_hc_starck.pdf;jsessionid=1501F6D45B15FA372B9A5F269F37D170.s1. [Accessed: 07-Apr-2018].

[50] P. M. Martin, *Handbook of Deposition Technologies for Films and Coatings : Science, Applications and Technology.* Elsevier Science, 2009.

[51] Matt Hughes, "What Is Sputtering? Magnetron Sputtering?," *Semicore Equipment*, 2014. [Online]. Available: http://www.semicore.com/what-is-sputtering. [Accessed: 08-Apr-2018].

[52] M. Seifert, G. K. Rane, S. B. Menzel, and T. Gemming, "The influence of barrier layers (SiO2, Al2O3, W) on the phase formation and stability of RuAl thin films on LGS and CTGS substrates for surface acoustic wave technology," *J. Alloys Compd.*, vol. 688, pp. 228–240, 2016.

[53] K. Ellmer, "Resistivity of polycrystalline zinc oxide films: current status and physical limit[J]," *J. Phys. D Appl. Phys.*, vol. 34, pp. 3097–3108, 2001.

[54] I. Petrov, P. B. Barna, L. Hultman, and J. E. Greene, "Microstructural evolution during film growth," *J. Vac. Sci. Technol. A Vacuum, Surfaces, Film.*, vol. 21, no. 5, pp. S117–S128, Sep. 2003.

[55] J. A. Thornton, "The microstructure of sputter-deposited coatings," *J. Vac. Sci. Technol. A Vacuum, Surfaces, Film.*, vol. 4, no. 6, pp. 3059–3065, Nov. 1986.

[56] R. W. Hoffman, "Physics of thin films," *Phys. Thin Film.*, vol. 3, pp. 211–273, 1966.

[57] R. Abermann, R. Koch, and R. Kramer, "Electron microscope structure and internal stress in thin silver and gold films deposited onto MgF2 and SiO substrates," *Thin Solid Films*, vol. 58, no. 2, pp. 365–370, Apr. 1979.

[58] M. F. Doerner and W. D. Nix, "Stresses and deformation processes in thin films on substrates," *Crit. Rev. Solid State Mater. Sci.*, vol. 14, no. 3, pp. 225–268, Jan. 1988.

[59] R. W. Hoffman, “Stresses in thin films: The relevance of grain boundaries and impurities,” *Thin Solid Films*, vol. 34, no. 2, pp. 185–190, May 1976.

[60] W. Buckel, “Internal Stresses,” *J. Vac. Sci. Technol.*, vol. 6, no. 4, pp. 606–609, Jul. 1969.

[61] W. D. Nix and B. M. Clemens, “Crystallite coalescence: A mechanism for intrinsic tensile stresses in thin films,” *J. Mater. Res.*, vol. 14, no. 08, pp. 3467–3473, Aug. 1999.

[62] A. A. Griffith, “The Phenomena of Rupture and Flow in Solids,” *Philos. Trans. R. Soc. A Math. Phys. Eng. Sci.*, vol. 221, no. 582–593, pp. 163–198, Jan. 1921.

[63] A. A. Volinsky, D. C. Meyer, T. Leisegang, and P. Paufler, “Fracture patterns in thin films and multilayers,” *MRS Proc.*, vol. 795, p. U3.8, Jan. 2003.

[64] M. Ohring, *Materials science of thin films : deposition and structure*. Academic Press, 2002.

[65] G. G. Stoney, “The Tension of Metallic Films Deposited by Electrolysis,” *Proc. R. Soc. A Math. Phys. Eng. Sci.*, vol. 82, no. 553, pp. 172–175, May 1909.

[66] S. M. Rossnagel and T. S. Kuan, “Alteration of Cu conductivity in the size effect regime,” *J. Vac. Sci. Technol. B Microelectron. Nanom. Struct.*, vol. 22, no. 1, p. 240, Jan. 2004.

[67] J.-W. Lim and M. Isshiki, “Electrical resistivity of Cu films deposited by ion beam deposition: Effects of grain size, impurities, and morphological defect,” *J. Appl. Phys.*, vol. 99, no. 9, p. 094909, May 2006.

[68] C.-U. Kim, J. Park, N. Michael, P. Gillespie, and R. Augur, “Study of electron-scattering mechanism in nanoscale Cu interconnects,” *J. Electron. Mater.*, vol. 32, no. 10, pp. 982–987, Oct. 2003.

[69] K. Fuchs and N. F. Mott, “The conductivity of thin metallic films according to the electron theory of metals,” *Math. Proc. Cambridge Philos. Soc.*, vol. 34, no. 01, p. 100, Jan. 1938.

[70] E. H. Sondheimer, “The mean free path of electrons in metals,” *Adv. Phys.*, vol. 50, no. 6, pp. 499–537, Sep. 2001.

[71] A. F. Mayadas and M. Shatzkes, “Electrical-Resistivity Model for Polycrystalline Films: the Case of Arbitrary Reflection at External Surfaces,” *Phys. Rev. B*, vol. 1, no. 4, pp. 1382–1389, Feb. 1970.

[72] L. J. van der Pauw, “A Method of Measuring the Resistivity and Hall Coefficient on Lamellae of Arbitary Shape,” *Philips Tech. Rev.*, vol. 20, pp. 220–224, 1959.

[73] J. Náhlík, I. Kašpárková, and P. Fitl, “Study of quantitative influence of sample defects on measurements of resistivity of thin films using van der Pauw method,” *Measurement*, vol. 44, no. 10, pp. 1968–1979, Dec. 2011.

[74] E. C. Chu, “Temperature-dependent yield properties of passivated aluminum thin films on silicon wafers,” Diss. Massachusetts Institute of Technology, 1996.

[75] P. Klapetek, D. Necas, and C. Anderson, “Gwyddion user guide,” *Czech Metrol. Inst.*, vol. 2007, p. 2009, 2004.

[76] “Dimension Icon SPM Overview,” *Bruker Corporation*, 2016. [Online]. Available: http://www.nanophys.kth.se/nanophys/facilities/nfl/afm/icon/bruker-help/Content/System Overview/SPM Overview.htm. [Accessed: 13-Apr-2018].

[77] C. A. Volkert and A. M. Minor, “Focused Ion Beam Microscopy and Micromachining,” *MRS Bull.*, vol. 32, no. 05, pp. 389–399, May 2007.

[78] E. J. Mittemeijer and U. Welzel, “The ‘state of the art’ of the diffraction analysis of crystallite size and lattice strain,” *Zeitschrift für Krist.*, vol. 223, no. 9, pp. 552–560, Jan. 2008.

[79] de K. Th. H., J. I. Langford, E. J. Mittemeijer, A. B. P. Vogels, and IUCr, “Use of the Voigt function in a single-line method for the analysis of X-ray diffraction line broadening,” *J. Appl. Crystallogr.*, vol. 15, no. 3, pp. 308–314, Jun. 1982.

[80] R. Delhez, T. de Keijser, E. Mittemeijer, and J. Langford, “Size and Strain Parameters from Peak Profiles: Sense and Nonsense,” *Aust. J. Phys.*, vol. 41, no. 2, p. 213, 1988.

[81] H. Kiessig, “Interferenz von Röntgenstrahlen an dünnen Schichten,” *Ann. Phys.*, vol. 402, no. 7, pp. 769–788, 1931.

[82] Yasaka Miho, “X-ray thin film measurement techniques,” *Rigaku J.*, vol. 26, no. 5, pp. 1–9, 2010.

[83] J. Nagano, “Electrical resistivity of sputtered molybdenum films,” *Thin Solid Films*, vol. 67, no. 1, pp. 1–8, Apr. 1980.

[84] L. Fabrega, I. Fernandez-Martinez, M. Parra-Borderias, O. Gil, A. Camon, R. Gonzalez-Arrabal, J. Sese, J. Santiso, J.-L. Costa-Kramer, and F. Briones, “Effects of Stress and Morphology on the Resistivity and Critical Temperature of Room-Temperature-Sputtered Mo Thin Films,” *IEEE Trans. Appl. Supercond.*, vol. 19, no. 6, pp. 3779–3785, Dec. 2009.

[85] S. M. Rossnagel and T. S. Kuan, “Alteration of Cu conductivity in the size effect regime,” *J. Vac. Sci. Technol. B Microelectron. Nanom. Struct.*, vol. 22, no. 1, p. 240, Jan. 2004.

[86] I. Kojima and B. Li, “Structural Characterization of Thin Films by X-ray Reflectivity,” *Rigaku J.*, vol. 16, no. 2, 1999.

[87] P. . Petrov, Z. . Ivanov, and S. . Gevorgyan, “X-ray study of SrTiO3 thin films in multilayer structures,” *Mater. Sci. Eng. A*, vol. 288, no. 2, pp. 231–234, Sep. 2000.

[88] C. K. Pan, D. C. Zheng, T. G. Finstad, W. K. Chu, V. S. Speriosu, M. A. Nicolet, and J. H. Barrett, “Structural study of GaSb/AlSb strained-layer superlattice,” *Phys. Rev. B*, vol. 31, no. 3, pp. 1270–1277, Feb. 1985.

[89] R. C. Cammarata, “Surface and interface stress effects in thin films,” *Prog. Surf. Sci.*, vol. 46, no. 1, pp. 1–38, May 1994.

[90] H. Windischmann, “Intrinsic stress in sputtered thin films,” *J. Vac. Sci. Technol. A Vacuum, Surfaces, Film.*, vol. 9, no. 4, pp. 2431–2436, Jul. 1991.